STIMULATED RAMAN DISPERSION SPECTROSCOPY WITH HOLLOW-CORE FIBER：FROM FUNDAMENTAL PRINCIPLES TO APPLICATIONS

HAIHONG BAO

PhD

The Hong Kong Polytechnic University

2020

The Hong Kong Polytechnic University

Department of Electrical Engineering

Stimulated Raman dispersion spectroscopy with hollow-core fiber：From fundamental principles to applications

Haihong Bao

A thesis submitted in partial fulfillment of the requirements for

the degree of Doctor of Philosophy

January 2020

CERTIFICATE OF ORIGINALITY

I hereby declare that this thesis is my own work and that, to the best of my knowledge and belief, it reproduces no material previously published or written, nor material that has been accepted for the award of any other degree or diploma, except where due acknowledgement has been made in the text.

…….. (Signed)

……Haihong BAO…… (Name of student)

Abstract

Identification and measurement of chemical substances with high sensitivity and good selectivity is of great importance for many practical applications, including pollutant analysis, industrial safety monitoring and health examination. Optical fiber-based laser absorption spectroscopy and its derivatives have been regarded as powerful techniques for sensitive detection. Measurements of absorptive gases (e.g., methane, acetylene and ammonia) have been extensively demonstrated using laser absorption spectroscopy and limit-of-detection from parts-per-million (ppm) to ppb parts-per-billion (ppb) levels has been achieved. However, these methods are not applicable to gases that have no absorption in the low-loss transmission window of optical fibers, which is in the near-infrared.

Raman spectroscopy is a versatile technology which can detect Raman-active gases that do not necessarily have absorption in the near-IR. The recent employment of the hollow-core fiber for Raman spectroscopy has greatly enhances both the spontaneous and stimulated Raman signals compared with the free-space system. Sensitive gas detection (e.g., hydrogen, nitrogen and methane) has been achieved with detection limit down to a few hundreds of ppm using lock-in amplifier with 1s time constant at ambient condition. Such system uses pump source in visible band and need sophisticated process to couple light beams in to hollow-core fibers.

Recently, our group has demonstrated all-fiber hydrogen gas sensors based on stimulated Raman gain spectroscopy with 15-m-long hollow-core photonic crystal fiber. The detection system operates in the telecom-wavelength-band (i.e., from 1530 to 1625 nm), where cost-effective fiber-optic components are available. The all-fiber systems avoid complex optical alignment, have the capability for remote detection, and are flexible for practical applications. Detection limit of ~140 ppm with 1 second lock-in time constant

is realized. However, further performance improvement is limited by the intensity fluctuation of the received signal at the photodetector, a problem common to the intensity-detection-based techniques

In this thesis, we develop a new branch of Raman spectroscopy to sensitively detect hydrogen based on stimulated Raman dispersion spectroscopy with hollow-core photonic crystal fibers. Stimulated Raman dispersion spectroscopy monitors the refractive index change during the Raman scattering process by sensitive optical fiber interferometers in the vicinity of a stimulated Raman transition. It essentially has better immunity to the intensity noise and large dynamic range.

The physical process of the stimulated Raman scattering induced dispersion involves two incident laser beams (i.e., a pump beam and a probe beam). The phase change of the probe beam can be modulated when the frequency difference between the pump and probe matches a Raman transition. For the first measurement of the Raman-induced dispersion change, a fiber Mach Zehnder interferometer with 7m-long hollow-core fiber is used to detect the accumulated phase change of the probe beam. The interferometer is stably operated at its quadrature point. By wavelength modulating the pump beam, measurement of the dispersion change with high signal-to-noise ratio is achieved. Applying the optimal modulation depth, this technique has been demonstrated for hydrogen detection with a normalized noise-equivalent concentration of 17.4 ppm/(m·W) at 3.5 bar and a dynamic range over 4 orders of magnitude. To our best knowledge, this is the first demonstration of the measurement of stimulated Raman scattering induced dispersion and its application for sensitive gas detection.

To develop a compact hydrogen sensor with compact size and fast response time, a Fabry Perot interferometer based on hollow-core fiber is implemented. Different from the Mach Zehnder interferometer, the typical length of the hollow core fiber is several

centimeters, which makes it much faster for gas molecules to diffuse into the hollo core. The Fabry Perot interferometer-based hydrogen sensors show excellent long-term stability since the time delay of the two reflected probe beams are extremely short (i.e., <0.2nm). Moreover, the single mode fibers connected to the hollow-core fiber are not parts of the interferometer, which ensures the environment perturbations imposed on the single mode fiber would not interfere the interferometer performance. With a 3.5 cm-long how-core Fabry Perot interferometer, hydrogen detection with detection limit of 0.42% using 1s integration time constant is demonstrated. Lower detection limit of 264 ppm may be realized by conducting the Allan deviation analysis and applying the optimal integration time constant of ~1300s.

The linewidth of hydrogen Raman transitions are quite narrow (i.e., typically a few hundred MHz). Though the Raman-induced refractive index change is small, the rapid variation of the refractive index change near Raman resonances can make considerable group refractive index change of the gas medium, which can be used to actively control the group velocity of optical pulses by adjusting the pump power level and gas pressure. Optical pulse delay as much as 1.42 ns with Raman gain of 10 dB in an 80-m-long hollow-core fiber filled with 2.5-bar hydrogen is achieved.

Publications arising from the thesis

Journal articles

1. **H. Bao,** W. Jin, Y. Miao, and H. L. Ho, “Laser induced dispersion with stimulated Raman scattering in gas-filled optical fiber,” J. Light. Technol. 37(9), 2120-2125 (2019).

2. **H. Bao,** W. Jin, and H. L. Ho, “Tuning of group delay with stimulated Raman scattering-induced dispersion in gas-filled optical fiber,” Chinese Opt. Lett., 18(6) 060601-4 (2020).

3. Y. Qi, Y. Zhao, **H. Bao**, W. Jin, and H. L. Ho, “Nanofiber enhanced stimulated Raman spectroscopy for ultra-fast, ultra-sensitive hydrogen detection with ultra-wide dynamic range,” Optica **6**(5), 570-576 (2019).

Conference proceedings

1. **H. Bao**, W. Jin, and Y. Miao, "Optical fiber hydrogen sensor with stimulated Raman dispersion spectroscopy," in 26th International Conference on Optical Fiber Sensors, pp. 1–4 (2019).

2. Y. Qi, Y. Zhao, **H. Bao**, W. Jin, H. L. Ho, and H. Luo, "Nano-taper enhanced stimulated Raman gain spectroscopy for high sensitivity hydrogen detection," in 26th International Conference on Optical Fiber Sensors, pp. 1–4 (2019).

Acknowledgements

First of all, I would like to express my sincere gratitude to Professor Wei Jin for giving me the opportunity to work with him and many other outstanding colleagues in his group. His intellectual rigor and integrity would always inspire me in my future career. Under his mentorship and, with his generous support and patient guidance, I have grown immensely as a researcher and I will always keep the curiosity exploring the new science and technology.

Special thanks go to Dr. Hoi Lut Ho, Dr. Chao Wang, Dr. Yuechuan Lin, Dr. Yanzhen Tan, Dr. Congzhe Zhang, Dr. Haipeng Luo and Dr. Yinping Miao for your inspiring discussions and kind help, especially at the early stage of my Ph.D. project.

I would also acknowledge Mr. Yan Zhao, Mr. Yun Qi, Mr. Pengcheng Zhao, Miss Han Gao, Miss Yingzhen Hong and Mr. Feifan Chen, for your support in my study and life.

Finally, I would like to express my gratitude to my beloved family for their unconditional love and support.

Table of contents

List of Figures

List of Tables

Chapter 1: Introduction

1.1 Research background

Sensitive gas detection with good selectivity is essential for numerous applications, including safety monitoring for industrial production, air-pollutant detection, and diseases diagnosis through breath analysis [1–7]. For disease diagnosis, analysis of the exhale gas components can be used for non-invasive disease diagnosis since certain volatile organic compounds within human breath have been identified as the products of the diseases-related physiological and pathophysiological process, e.g., liver failure and lung cancer [8–10]. Detection and identification of these gas compounds with high sensitivity and good selectivity are critical for a comprehensive understanding of the biomedical process.

Various techniques have been developed for sensitive gas detection. Functional materials including sensitive coatings on optical fibers and electrochemical materials have been utilized for trace of gas components. When the gas molecules are attached to the sensing material, characteristics of the functional materials, e.g., the refractive index (RI), electric resistance and geometric size, will be modified and would induce change in the measured reflectance, absorbance, or optical path length. Though sensitive gas detection has been demonstrated, the sensing materials are highly sensitive to the contamination and this technology has limitations in selectivity, dynamic range and repeatability [11,12].

Another widely used technology is the mass spectrometry (MS), which has been proved to be a highly sensitive gas detection method. Detection limit of parts per million (ppm) or parts per billion (ppb) level has been realized. However, its selectivity of different gas

types can be compromised due to the substantial overlap of the ratios of *m/z* from different types of gas molecules. Moreover, equipment required for MS is usually complicated and expensive, which needs to be operated by well-trained operators.

1.2 Laser absorption spectroscopy

Laser absorption spectroscopy (LAS) and its derivatives, including the direct absorption spectroscopy (DAS), photothermal spectroscopy (PTS), photoacoustic spectroscopy (PAS) and molecular dispersion spectroscopy (MDS), rely on the molecular "fingerprint" of the gas absorption lines. LAS shows overwhelming advantages of high sensitivity and selectivity for identification and detection of the gas components. With all-fiber based technologies, the capacity of LAS has been significantly expanded for applications in the harsh environment, remote and distributed sensing and wavelength multiplexing fiber networks.

1.2.1 Direct absorption spectroscopy

DAS measures the molecular absorption induced optical loss along the transmission path, which is described by the Beer-Lambert law. All-fiber based DAS was first demonstrated using optical fiber collimator pair (GRIN lenses) in an open gas absorption cell [13]. The one-way optical path is usually several centimeters long and the detection limit is limited to ppm-level. Recently, the hollow-core fiber-based gas cells greatly expand the absorption path length. Hollow-core photonic crystal fibers (HC-PCF) have most of their optical power confined within the air core (>95%) [14] and are ideal platform for strong light-matter interaction over long distance [15,16]. Compact all-fiber gas sensors can be realized by coiling the HC-PCF to small diameters without significant bending loss [17]. It has been demonstrated that various gases (acetylene, ammonia and methane) can be detected down to ppm level using DAS with ~1 to ~13m-long HC-PCF

[18–20]. The response time of the DAS with meters-long HC-PCF can be shortened to ~3s by drilling multiple micro gas-filling channels using femtosecond laser [21,22].

1.2.2 Photothermal spectroscopy

The concepts of PTS in an HC-PCF can be explained using Fig. 1.1. When the wavelength of the pump laser is tuned to the molecular absorption line, the gas molecules absorb the energy from the modulated pump beam and induce localized heating, which changes the temperature through thermal relaxation. The modulated temperature distribution then induces density and pressure changes of the gases within the hollow core area, which modulates the RI of the gas medium. Among different approaches of measuring the RI change, photothermal interferometry (PTI) measures the RI change via the detection of the accumulated phase change along the absorption path. The magnitude of the PT phase change is proportional to gas concentration, the molecular absorption strength, the absorption path length and the pump power level Recently, an all-fiber PTI gas sensor based on 10-m-long HC-HCF has been demonstrated, ultra-sensitive acetylene detection with a detection limit down to 2 ppb and an unprecedented dynamic range of nearly six orders of magnitude have been achieved [23]. The all-fiber based PTI is entirely compatible with existing optical fiber network.

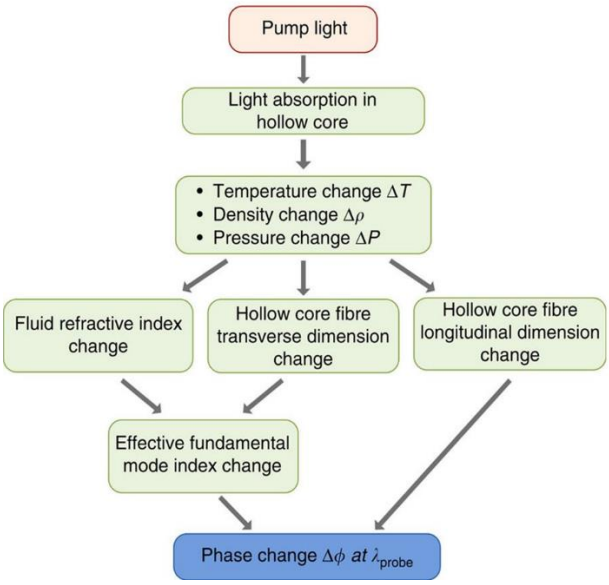

Fig. 1.1 The basic physical process involved in the PT-induced RI and phase modulation in HC-PCF [23].

1.2.3 Photoacoustic spectroscopy

The periodic absorption-induced heating would cause local gas pressure change. PAS detects the optical absorption by monitoring the generated acoustic pressure wave, which is a sensitive technique for gas detection with good selectivity [24–26]. Early PAS systems used mid-infrared pump laser sources and bulky photoacoustic cells [27]. A CO_2 laser was used as the pump source to excite the gas molecules for PA detection of carbon dioxide. However, the newly developed PAS systems use near-infrared semiconductor lasers as the pump source and compact photoacoustic cells with fiber pigtails [28,29]. A typical PAS gas detection system is depicted in Fig. 1.2. With pump power of ~750mW, detection of trace ammonia down to ppb level has been realized [29]. Acoustic resonators are used to enhance the magnitude of the detected photoacoustic signal. When the modulation frequency of the pump light matches the resonant frequency of the

well-designed acoustic resonator, the measured acoustic signal can be significantly amplified [30,31]. These acoustic signals are detected using electric capacitive microphones or piezoelectric transducers such as a quartz fork [32]. Recently, progress has been made in developing fiber-tip optical microphones [33–36] and applying them for PAS gas sensors. Using optical fiber to deliver the pump beam to sample gas and to detect the acoustic signal makes it possible to realize all-optical fiber PAS gas sensors with remote detection capability [37].

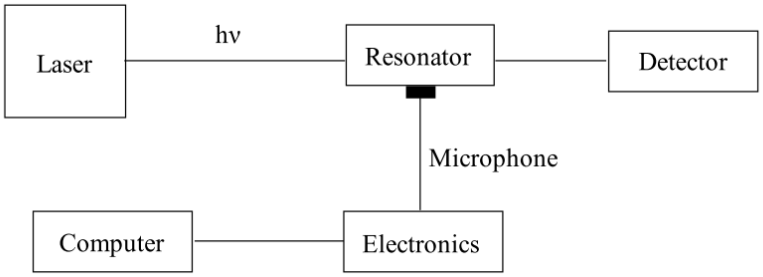

Fig. 1.2 A typical PAS system for gas detection [26]

1.2.4 Molecular dispersion spectroscopy

MDS is a newly developed derivative technology of LAS, which detects the optical absorption induced RI change (i.e., dispersion) near the molecular absorption resonant wavelength. The magnitude of the dispersion change is directly proportional to the gas concentration and can be detected by measurement of the accumulated optical phase change using optical interferometers. This technology is essentially different from DAS and provides advantages of better immunity to the system intensity noise, calibration-free operation and larger dynamic range since the phase change is linearly proportional to the gas concentration over the range from 0-100%. Different measurement configurations such as Mach-Zehnder interferometer, chirped laser dispersion spectroscopy (CLaDS) and heterodyne phase-sensitive dispersion

spectroscopy (HPSDS) have been demonstrated for gas detection from ppm to ppb level with open-path gas cells. HPSDS has been applied for gas detection based on MDS both in NIR and MIR bands [38,39]. CLaDS is an alternative method for MDS is to measure the beating frequency induced by the dispersion [40–42], which has been applied for the field test of atmospheric methane concentration emitted from wetlands [43]. A typical CLaDS is shown in Fig. 1.3.

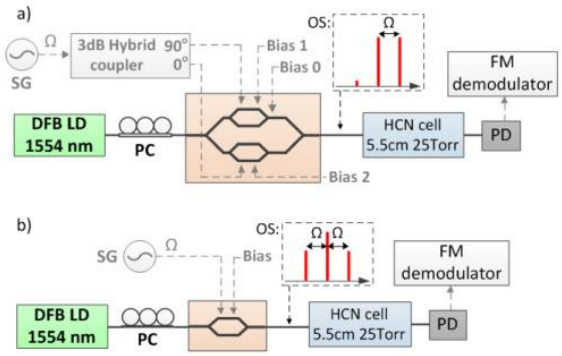

Fig. 1.3 The principles of two typical CLaDS systems (a) CLaDS system with dual-wavelength beam generation. 3dB hybrid coupler is used to drive the modulator with two orthogonal signals; (b) CLaDS system with triple-wavelength beam generation. LD: laser diode; SG: signal generator; PC: polarization controller; PD: photodetector and OS: optical spectrum [42].

1.3 Raman spectroscopy

Raman spectroscopy (RS) is a powerful technology which relies on the molecular structures for chemical compounds analysis and has excellent selectivity. RS can be used to detect chemical components with no or very weak absorptions as long as they are Raman-active. Different RS-based techniques have been developed, e.g., spontaneous and stimulated Raman spectroscopy, photoacoustic Raman spectroscopy (PARS), photothermal Raman spectroscopy (PTRS) and stimulated Raman gain (SRG) spectroscopy.

1.3.1 Photoacoustic Raman spectroscopy

Photoacoustic Raman spectroscopy (PARS) combines the stimulated Raman scattering (SRS) spectroscopy with PAS, which is a sensitive technique for trace gas molecules [44–48]. The SRS process requires simultaneous illumination of the gas sample by two laser beams (pump and Stokes) and the frequency difference of the laser beams should match the Raman transition frequency. The pump laser excites the gas molecules to a higher energy level via SRS process. Then the excited gas molecules go back to the initial energy level and generate heating through thermal relaxation. At the same time, energy is transferred from the pump beam to the Stokes beam. If the pump beam is modulated, the periodic temperature modulation will generate the acoustic wave. The magnitude of the acoustic wave is proportional to the gas concentration and the product of the power levels of the pump and Stokes lasers. Since Raman scattering is an inefficient process of heat generation, typically high power pump sources are needed for sensitive gas detection. Trace gas detection of molecular hydrogen down to 4.6 ppm has been realized with pulsed lasers (35 mJ pulse energy at 532 nm for pump, 45 mJ at 681-684 nm for Stokes, 6 ns pulse duration, 10 Hz repetition rate, and 256 s measurement time) [48]. A typical experimental setup for PARS is shown in Fig. 1.4. Similar to PAS, PARS systems use sensitive microphones, which have limited detection areas (i.e., mm to cm in diameter) and the detection sensitivity cannot be improved by increasing the path length of the gas cell.

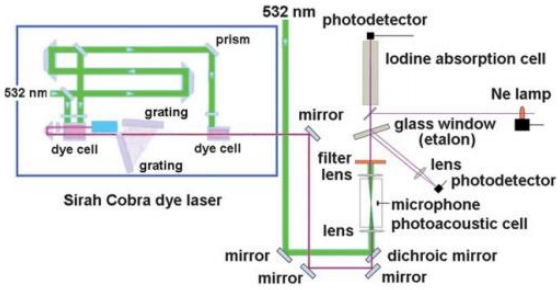

Fig. 1.4 A typical experimental setup of PARS for sensitive gas detection [48].

1.3.2 Photothermal Raman spectroscopy

The generated heating during stimulated Raman scattering can also induce the RI change of the gas medium. Photothermal Raman spectroscopy (PTRS) detects the RI due to generated heating during the SRS process. Different techniques have been developed for PTRS detection. Thermal-lens PTRS was used for hydrogen detection and achieved detection limit of 9 ppm with 50 mJ pump at 532.1 nm, 21 mJ Stokes at 683.2 nm, 6-ns pulse duration and 10-Hz repetition rate [49]. Thermal laser-induced gratings (LIGs) PTRS probes the LIG signal generated via two-photon stimulated Raman excitation of pure rotational Raman transitions of gas molecules, using a single broadband pump source. Dye laser with pulse duration of a few ns is used as the pump to efficiently excite the LIGs, which can cover a wide spectral range of ~400 cm^{-1}. Several gases (e.g., N_2, CO_2, C_3H_8) at room temperature with gas pressures of 0.1-5 bar have been experimentally investigated [50].

1.3.3 Stimulated Raman gain spectroscopy

The stimulated Raman gain (SRG) spectroscopy is one powerful type of coherent

Raman spectroscopy. The detected Raman gain signal is linearly proportional to the gas concentration, which is convenient for measurement compared to the quadratic dependence on the gas concentration provided by the coherent anti-Stokes Raman spectroscopy (CARS). Direct SRG measurement has been demonstrated with a continuous wave (CW) pump source. The detection results show that background signals have been substantially suppressed. Detection limit comparable to or exceeding that realized by using CARS is realized [51]. It has been demonstrated that the use of HC-PCFs can enhance the sensitivity of gas detection systems by two to three orders of magnitude over the free-space systems for both spontaneous and stimulated RS [52–54]. With 1 to 4.5 meter long HC-PCFs, these systems have achieved detection limit of 10^2-10^3 ppm for different gases (e.g., H_2, N_2, O_2 and CO_2) at ambient conditions. Under higher pressure (e.g., 20 bar) conditions, gas detection limit down to several ppm has been achieved using a meter-long HC-PCF (HC-580-02 from NKT Photonics) with pump laser power of 2W at 532 nm and Roper Scientific spectrometer (Model Acton 2556) equipped with liquid-nitrogen-cooled CCD [55]. However, these methods require high power laser and complex detectors, which are not suitable for practical applications.

Recently, our research group has demonstrated all-fiber hydrogen detection based on SRG with HC-PCF [56].The experimental setup is depicted in Fig. 1.5. Two lasers with wavelengths around 1532 and 1620 nm are used as the pump and the probe (Stokes) sources, respectively. Detection limit of ~140 ppm has been achieved for hydrogen detection with ~40 mW pump laser delivered to a 15-metre-long HC-PCF when the time constant of the lock-in amplifier is 1s. The performance of such system is mainly limited by the laser intensity fluctuation and residual mode interference of the HC-PCF since even the state-of-the-art HC-PCFs are not perfect single mode fibers and they support a few high-order modes.

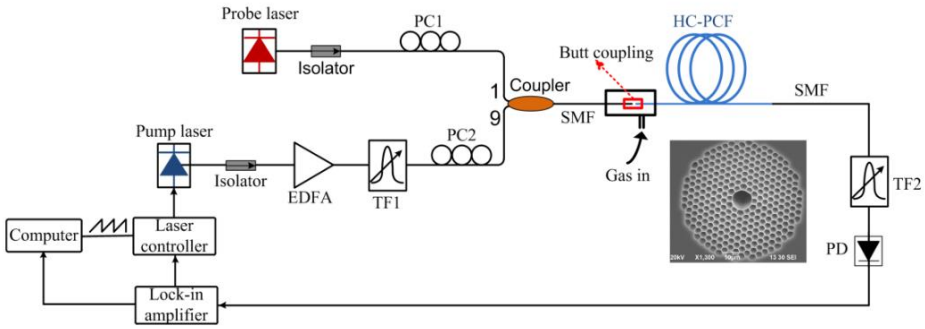

Fig. 1.5 The experimental setup for all-fiber hydrogen detection based on SRG. PC: polarization controller; EDFA: erbium-doped fiber amplifier; TF: tunable filter and PD: photodetector.

1.4 Research motivations

Though RS is generally a powerful technique for gas detection, it is remained challenging to further improve detection sensitivity due to the need of very high pump power and ultra-long light-gas interaction length. Recently, there is a report on stimulated Raman dispersion spectroscopy (SRDS), which detects the anomalous dispersion induced phase shift in the vicinity of SRG lines and has been applied for high resolution biological imaging. Compared to the gain or intensity based detection, the phase-shift-based detection scheme is regarded as a more robust method to reduce intensity noise [57].

SRS can also modify RI change in gases. However, to my knowledge, the study of SRDS in gases was not conducted before, not with open path optical systems, nor with optical fiber systems. In fact, due to the very small Raman scattering cross section and the limited light-gas interaction length, it is very difficult to demonstrate SRDS in gases with open-path optical systems and high-power pump laser is needed. Recently, HC-PCF has been proposed to enhance the SRS process [52–54]. HC-PCF can confine the optical mode in the hollow core area, which has nearly perfect overlap with gas molecules. The optical mode radius in HC-PCF small (e.g., hollow core radius of NKT HC-1550-06

fiber is ~5 μm), which dramatically increases the light intensity and enhances SRS process given the same laser power. It is easy to furtherly enhance SRS process with the employment of tens-meters-long HC-PCF. Such HC-PCF is compatible with the existed optical fiber networks and expands the capability of SRDS for remote sensing and applications under harsh environment.

Here, I propose to study SRDS in gases with HC-PCF and use it for high sensitivity gas detection and optical pulse delay tuning. Similar to the MDS, the output signal of SRDS depends linearly on the gas concentration over a large dynamic range and SRDS has high immunity to the intensity fluctuations. The difference between MDS and SRDS is that the phase change of SRDS is induced by pump associated SRS process which can be easily modulated by modulating pump laser (e.g. intensity, wavelength and frequency modulation). The dispersion induced phase change of the probe beam can be extracted through stable fiber interferometer with high sensitivity. The development of such HC-PCF-based SRDS may benefit highly sensitive gas detection and can furtherly improve the detection limit of the existing Raman spectroscopy.

The SRS induced RI variation near narrow Raman resonances in gases can significantly reduce the group velocity of signal pulses around Stokes wavelength and result in detectable pulse delay. Hence, we extend the application of the Raman-induced dispersion in gases for dynamically controlling the delay of optical pulses since it is important in optical communication, signal processing. Such Raman-induced dispersion can be dynamically manipulated by changing the wavelength and power level of the pump laser as well as the gas pressure, composition and concentration, which provides a highly flexible means of controlling light dispersion.

1.5 Thesis outline

This thesis is organized as follows:

Chapter 1 introduces the background of gas detection. Some widely used laser spectroscopy technologies, including laser absorption spectroscopy and Raman spectroscopy, are reviewed. And then the motivation of this work is presented followed by the thesis outline.

Chapter 2 reviews the theory describing the physical process of the stimulated Raman scattering. The physical origin and phenomena of the Raman gain and Raman-induced dispersion are well investigated. The physical concepts and processes discussed in this chapter is the basis for the techniques introduced in the following chapters.

Chapter 3 presents the theory of the stimulated Raman dispersion spectroscopy. The interferometric measurement of Raman-induced dispersion using wavelength modulation is proposed. The relationship between the harmonic signals and the wavelength-modulated Raman dispersion is revealed. The dependence of the harmonic signal amplitudes on the modulation depth is investigated too. The optimal modulation depths are calculated to acquire the largest harmonic signal amplitudes. This chapter provides theoretical guidance for optimization of the operation of the stimulated Raman dispersion spectroscopy systems.

Chapter 4 presents the experimental results of the measured stimulated Raman dispersion in hydrogen-filled HC-PCF and applications of that for sensitive hydrogen detection. The mathematical model derived in Chapter 3 is experimentally verified by measurement of the harmonic signals with different modulation depths. Noise performance of the detection system is also evaluated.

Chapter 5 demonstrates a newly developed hydrogen sensor with stimulated Raman dispersion using Fabry Perot interferometer (FPI) for practical gas detection. Fabrication process and operation principles of the proposed FPI as the sensing head for

hydrogen detection are presented. Advantages of performances of the FPI is discussed. Long-term stability of the FPI hydrogen detection system is evaluated.

Chapter 6 extends the application of the stimulated Raman dispersion to dynamically control the group velocity of optical pulses in hydrogen-filled optical fibers. SRS-induced RI change is experimentally measured and the group RI change near the Raman resonance is evaluated. Dynamically tuning of the optical pulse delay is demonstrated by changing the pump pulse power as well as the gas pressure. The experiment results are compared with the theoretic predictions.

Chapter 7 summarizes the thesis and discusses future works.

References

1. U. Willer, M. Saraji, A. Khorsandi, P. Geiser, and W. Schade, "Near- and mid-infrared laser monitoring of industrial processes, environment and security applications," Opt. Lasers Eng. **44**(7), 699–710 (2006).
2. P. A. Martin, "Near-infrared diode laser spectroscopy in chemical process and environmental air monitoring," Chem. Soc. Rev. **31**(4), 201–210 (2002).
3. T. Rück, R. Bierl, and F. M. Matysik, "NO2 trace gas monitoring in air using off-beam quartz enhanced photoacoustic spectroscopy (QEPAS) and interference studies towards CO2, H2O and acoustic noise," Sensors Actuators, B Chem. **255**(2), 2462–2471 (2018).
4. P. Laj, J. Klausen, M. Bilde, C. Plaß-Duelmer, G. Pappalardo, C. Clerbaux, U. Baltensperger, J. Hjorth, D. Simpson, S. Reimann, P. F. Coheur, A. Richter, M. De Mazière, Y. Rudich, G. McFiggans, K. Torseth, A. Wiedensohler, S. Morin, M. Schulz, J. D. Allan, J. L. Attié, I. Barnes, W. Birmili, J. P. Cammas, J. Dommen, H. P. Dorn, D. Fowler, S. Fuzzi, M. Glasius, C. Granier, M. Hermann, I. S. A. Isaksen, S. Kinne, I. Koren, F. Madonna, M. Maione, A. Massling, O. Moehler, L. Mona, P. S. Monks, D. Müller, T. Müller, J. Orphal, V. H. Peuch, F. Stratmann, D. Tanré, G. Tyndall, A. Abo Riziq, M. Van Roozendael, P. Villani, B. Wehner, H. Wex, and A. A. Zardini, "Measuring atmospheric composition change," Atmos. Environ. **43**(33), 5351–5414 (2009).
5. E. Boedeker, G. Friedel, and T. Walles, "Sniffer dogs as part of a bimodal bionic research approach to develop a lung cancer screening," Interact. Cardiovasc. Thorac. Surg. **14**(5), 511–515 (2012).
6. M. McCulloch, T. Jezierski, M. Broffman, A. Hubbard, K. Turner, and T. Janecki, "Diagnostic accuracy of canine scent detection in early- and late-stage

lung and breast cancers," Integr. Cancer Ther. **5**(1), 30–39 (2006).

7. T. Bögözi, J. Popp, and T. Frosch, "Fiber-enhanced Raman multi-gas spectroscopy: What is the potential of its application to breath analysis?," Bioanalysis **7**(3), 281–283 (2015).
8. C. Wang and P. Sahay, "Breath analysis using laser spectroscopic techniques: Breath biomarkers, spectral fingerprints, and detection limits," Sensors **9**(10), 8230–8262 (2009).
9. W. Miekisch, J. K. Schubert, and G. F. E. Noeldge-Schomburg, "Diagnostic potential of breath analysis - Focus on volatile organic compounds," Clin. Chim. Acta **347**(1–2), 25–39 (2004).
10. J. Wojtas, Z. Bielecki, T. Stacewicz, J. Mikołajczyk, and M. Nowakowski, "Ultrasensitive laser spectroscopy for breath analysis," Opto-Electronics Rev. **20**(1), 26–39 (2012).
11. J. Dai, L. Zhu, G. Wang, F. Xiang, Y. Qin, M. Wang, and M. Yang, "Optical Fiber Grating Hydrogen Sensors: A Review," Sensors **17**(3), 577 (2017).
12. G. Korotcenkov, S. Do Han, and J. R. Stetter, "ChemInform Abstract: Review of Electrochemical Hydrogen Sensors," ChemInform **40**(22), no-no (2009).
13. B. Culshaw, G. Stewart, F. Dong, C. Tandy, and D. Moodie, "Fibre optic techniques for remote spectroscopic methane detection—from concept to system realisation," Sensors Actuators B **51**, 25–37 (1998).
14. P. Russell, "Photonic Crystal Fibres," **285**(September 2002), 2300 (2003).
15. T. Ritari, H. Ledvigsen, J. C. Petersen, T. Soreasen, A. Bjarklev, and T. P. Hansen, "Gas sensing using air-guiding photonic bandgap fibers," OSA Trends Opt. Photonics Ser. **96 A**(17), 1579–1580 (2004).
16. Y. L. Hoo, W. Jin, H. L. Ho, J. Ju, and D. N. Wang, "Gas diffusion measurement using hollow-core photonic bandgap fiber," Sensors Actuators, B Chem. **105**(2),

183–186 (2005).

17. T. P. Hansen, J. Broeng, C. Jakobsen, G. Vienne, H. R. Simonsen, M. D. Nielsen, P. M. W. Skovgaard, J. R. Folkenberg, and A. Bjarklev, "Air-Guiding Photonic Bandgap Fibers: Spectral Properties, Macrobending Loss, and Practical Handling," J. Light. Technol. **22**(1), 11–15 (2004).

18. F. Yang, W. Jin, Y. Cao, H. L. Ho, and Y. Wang, "Towards high sensitivity gas detection with hollow-core photonic bandgap fibers," Opt. Express **22**(20), 24894 (2014).

19. X. Li, J. Pawlat, J. Liang, and T. Ueda, "Measurement of low gas concentrations using photonic bandgap fiber cell," IEEE Sens. J. **10**(6), 1156–1161 (2010).

20. A. M. Cubillas, M. Silva-Lopez, J. M. Lazaro, O. M. Conde, M. N. Petrovich, and J. M. Lopez-Higuera, "Methane detection at 1670-nm band using a hollow-core photonic bandgap fiber and a multiline algorithm," Opt. Express **15**(26), 17570 (2007).

21. F. Yang, W. Jin, Y. Lin, C. Wang, H. Lut, and Y. Tan, "Hollow-core microstructured optical fiber gas sensors," J. Light. Technol. **35**(16), 3413–3424 (2017).

22. Y. L. Hoo, S. Liu, H. L. Ho, and W. Jin, "Fast response microstructured optical fiber methane sensor with multiple side-openings," IEEE Photonics Technol. Lett. **22**(5), 296–298 (2010).

23. W. Jin, Y. Cao, F. Yang, and H. L. Ho, "Ultra-sensitive all-fibre photothermal spectroscopy with large dynamic range," Nat. Commun. **6**, (2015).

24. A. Miklós, P. Hess, and Z. Bozóki, "Application of acoustic resonators in photoacoustic trace gas analysis and metrology," Rev. Sci. Instrum. **72**(4), 1937–1955 (2001).

25. T. Schmid, "Photoacoustic spectroscopy for process analysis," Anal. Bioanal.

Chem. **384**(5), 1071–1086 (2006).

26. A. Elia, P. M. Lugarà, C. di Franco, and V. Spagnolo, "Photoacoustic techniques for trace gas sensing based on semiconductor laser sources," Sensors **9**(12), 9616–9628 (2009).
27. C. Haisch, "Photoacoustic spectroscopy for analytical measurements," Meas. Sci. Technol. **23**(1), (2012).
28. M. E. Webber, M. Pushkarsky, and C. K. N. Patel, "Fiber-amplifier-enhanced photoacoustic spectroscopy with near-infrared tunable diode lasers," Appl. Opt. **42**(12), 2119 (2003).
29. J. P. Besson, S. Schilt, E. Rochat, and L. Thévenaz, "Ammonia trace measurements at ppb level based on near-IR photoacoustic spectroscopy," Appl. Phys. B Lasers Opt. **85**(2–3), 323–328 (2006).
30. C. F. Dewey, R. D. Kamm, and C. E. Hackett, "Acoustic amplifier for detection of atmospheric pollutants," Appl. Phys. Lett. **23**(11), 633–635 (1973).
31. R. D. Kamm, "Detection of weakly absorbing gases using a resonant optoacoustic method," J. Appl. Phys. **47**(8), 3550–3558 (1976).
32. A. A. Kosterev, F. K. Tittel, D. V. Serebryakov, A. L. Malinovsky, and I. V. Morozov, "Applications of quartz tuning forks in spectroscopic gas sensing," Rev. Sci. Instrum. **76**(4), 1–9 (2005).
33. Q. Wang, J. Wang, L. Li, and Q. Yu, "An all-optical photoacoustic spectrometer for trace gas detection," Sensors Actuators, B Chem. **153**(1), 214–218 (2011).
34. W. Wang, N. Wu, Y. Tian, C. Niezrecki, and X. Wang, "Miniature all-silica optical fiber pressure sensor with an ultrathin uniform diaphragm," Opt. Express **18**(9), 9006 (2010).
35. J. Ma, H. Xuan, H. L. Ho, W. Jin, Y. Yang, and S. Fan, "Fiber-optic fabry-pérot acoustic sensor with multilayer graphene diaphragm," IEEE Photonics Technol.

Lett. **25**(10), 932–935 (2013).

36. O. Kilic, M. Digonnet, G. Kino, and O. Solgaard, "External fibre Fabry-Perot acoustic sensor based on a photonic-crystal mirror," Meas. Sci. Technol. **18**(10), 3049–3054 (2007).

37. W. Jin, H. L. Ho, Y. C. Cao, J. Ju, and L. F. Qi, "Gas detection with micro- and nano-engineered optical fibers," Opt. Fiber Technol. **19**(6 PART B), 741–759 (2013).

38. P. Martín-Mateos and P. Acedo, "Heterodyne phase-sensitive detection for calibration-free molecular dispersion spectroscopy," Opt. Express **22**(12), 15143 (2014).

39. P. Martín-Mateos, J. Hayden, P. Acedo, and B. Lendl, "Heterodyne Phase-Sensitive Dispersion Spectroscopy in the Mid-Infrared with a Quantum Cascade Laser," Anal. Chem. **89**(11), 5916–5922 (2017).

40. G. Plant, Y. Chen, and G. Wysocki, "Optical heterodyne-enhanced chirped laser dispersion spectroscopy," 2016 Conf. Lasers Electro-Optics, CLEO 2016 **42**(14), 2770–2773 (2016).

41. G. Plant, A. Hangauer, and G. Wysocki, "Fundamental Noise Characteristics of Chirped Laser Dispersion Spectroscopy," IEEE J. Sel. Top. Quantum Electron. **23**(2), 147–156 (2017).

42. M. Nikodem, G. Plant, Z. Wang, P. Prucnal, and G. Wysocki, "Chirped lasers dispersion spectroscopy implemented with single- and dual-sideband electro-optical modulators," Opt. Express **21**(12), 14649 (2013).

43. G. Plant, M. Nikodem, P. Mulhall, R. K. Varner, D. Sonnenfroh, and G. Wysocki, "Field test of a remote multi-path CLaDS methane sensor," Sensors (Switzerland) **15**(9), 21315–21326 (2015).

44. J. J. Barrett and D. F. Heller, "Theoretical analysis of photoacoustic Raman

spectroscopy," J. Opt. Soc. Am. **71**(11), 1299 (1981).

45. G. A. West and J. J. Barrett, "Pure rotational stimulated Raman photoacoustic spectroscopy," Opt. Lett. **4**(12), 395 (1979).

46. D. R. Siebert, G. A. West, and J. J. Barrett, "Gaseous trace analysis using pulsed photoacoustic Raman spectroscopy," Appl. Opt. **19**(1), 53 (1980).

47. Y. Oki, N. Kawada, Y. Abe, and M. Maeda, "Nonlinear Raman spectroscopy without tunable laser for sensitive gas detection in the atmosphere," Opt. Commun. **161**(1–3), 57–62 (1999).

48. C. L. Spencer, V. Watson, and M. Hippler, "Trace gas detection of molecular hydrogen H2by photoacoustic stimulated Raman spectroscopy (PARS)," Analyst **137**(6), 1384–1388 (2012).

49. Y. Oki, S. Nakazono, Y. Nonaka, and M. Maeda, "Sensitive H_2 detection by use of thermal-lens Raman spectroscopy without a tunable laser," Opt. Lett. **25**(14), 1040 (2000).

50. D. N. Kozlov, M. C. Weikl, J. Kiefer, T. Seeger, and A. Leipertz, "Two-photon stimulated Raman excitation of thermal laser-induced gratings in molecular gases using broadband radiation of a single laser.," Opt. Express **16**(22), 18379–18389 (2008).

51. A. Owyoung, *Coherent Raman Gain Spectroscopy Using CW Laser Sources* (1978), (3).

52. M. P. Buric, J. Falk, K. Chen, and S. Woodruff, "Enhanced spontaneous Raman scattering using a photonic crystal fiber," Opt. InfoBase Conf. Pap. **47**(23), 4255–4261 (2008).

53. J. L. Doménech and M. Cueto, "Sensitivity enhancement in high resolution stimulated Raman spectroscopy of gases with hollow-core photonic crystal fibers," Opt. Lett. **38**(20), 4074 (2013).

54. P. G. Westergaard, M. Lassen, and J. C. Petersen, "Differential high-resolution stimulated CW Raman spectroscopy of hydrogen in a hollow-core fiber," Opt. Express **23**(12), 16320 (2015).

55. S. Hanf, T. Bögözi, R. Keiner, T. Frosch, and J. Popp, "Fast and highly sensitive fiber-enhanced Raman spectroscopic monitoring of molecular H2 and CH4 for point-of-care diagnosis of malabsorption disorders in exhaled human breath," Anal. Chem. **87**(2), 982–988 (2015).

56. F. Yang and W. Jin, "All-fiber hydrogen sensor based on stimulated Raman gain spectroscopy with a 1550-nm hollow-core fiber," in *Optical Fiber Sensors Conference (OFS), 2017 25th* (2017), **0**(0), p. 103233C.

57. F. E. Robles, M. C. Fischer, and W. S. Warren, "Dispersion-based stimulated Raman scattering spectroscopy, holography, and optical coherence tomography," Opt. Express **24**(1), 485 (2016).

Chapter 2: Theoretical background of Raman scattering

In this chapter, I would review the theory of stimulated Raman scattering and introduce the origin of the Raman gain and dispersion. This is mainly based on the references [1,2].

2.1 Theory of Raman scattering

In this section, the process of the Raman scattering would be treated using quantum mechanics theory. A Hamiltonian function H is introduced here to describe the whole physical system including the Raman-active molecules H_v, the laser field H_{em} and the interactions between the laser field and the molecules H_{int}.

The full expression of Hamiltonian H_v may be expressed as:

$$H_v = \sum_i \frac{1}{2m}\left(\dot{r}_i^2 + \omega_0^2 r_i^2\right) \tag{2.1}$$

where integer i runs over all the molecules, m is the reduced mass, r is the relevant local coordinate and ω_0 is the transition frequency of the molecules. H_v generally comprises two parts: the kinetic energy and the potential energy of the uncoupled molecules.

The laser field H_{em} which contains the electric and magnetic energy may be expressed as:

$$H_{em} = \frac{1}{8\pi}\int\left(\varepsilon \boldsymbol{E}^2 + \frac{1}{\mu}\boldsymbol{B}^2\right)dV \tag{2.2}$$

where $\boldsymbol{E}$ is the electric field strength, $\boldsymbol{B}$ is the magnetic inductance, ε is the relative permittivity and μ is the relative permeability. The integration is operated over the whole interaction volume.

The interaction Hamiltonian H_{int} describing the light-molecule interaction is directly responsible for the Raman scattering process, which can be treated with electric dipole

approximation and applying the Placzek model, the polarizability α of the molecular system can be expanded as [3]:

$$\alpha=\alpha_0+\frac{\partial\alpha}{\partial r}r+... \tag{2.3}$$

where α_0 is the polarizability of the molecular system without forced oscillation and is related to the Rayleigh scattering. The linear term of *r* which is important for the interaction Hamiltonian H_{int} is responsible for the coupling nucleus and electrons and may be expressed as:

$$H_{\text{int}}=-\frac{1}{2}\sum_i\left(\frac{\partial\alpha}{\partial r}\right)r(\boldsymbol{R}_i)\boldsymbol{E}(\boldsymbol{R}_i)\boldsymbol{E}(\boldsymbol{R}_i) \tag{2.4}$$

where $\boldsymbol{R}_i$ is the coordinate position of the *i*th molecule. The sum is carried out over the entire interaction volume. If we only consider the pump laser field and the first Stokes field ($\boldsymbol{E}$=$\boldsymbol{E}_{\text{p}}$+$\boldsymbol{E}_{\text{s}}$), the H_{int} responsible for the Stokes light generation is:

$$H_{\text{int}}=-\sum_i\left(\frac{\partial\alpha}{\partial r}\right)r(\boldsymbol{R}_i)\boldsymbol{E}_p(\boldsymbol{R}_i)\boldsymbol{E}_s(\boldsymbol{R}_i) \tag{2.5}$$

After second quantization of the laser fields, the Hamiltonians H_v, H_{em} and H_{int} may be rewritten as the follows:

$$H_v=\sum_{k_v}\hbar\omega_0\left(b_{k_v}^{+}b_{k_v}+\hat{I}/2\right) \tag{2.6}$$

$$a_{k_\lambda}^{+}\ H_{em}=\sum_{k_\lambda}\hbar\omega_{k_\lambda}\left(a_{k_\lambda}^{+}a_{k_\lambda}+\hat{I}/2\right) \tag{2.7}$$

$$H_{\text{int}}=\left(\frac{\partial\alpha}{\partial r}\right)\frac{\sqrt{N_0}\pi\hbar^{3/2}}{n_s n_p V\sqrt{m}}\sum_{k_s,k_p}\left(\frac{2\omega_s\omega_p}{\omega_0}\right)^{1/2}\left(b_{k_v}^{+}a_{k_s}^{+}a_{k_p}+b_{k_v}a_{k_s}a_{k_p}^{+}\right)\delta(\boldsymbol{k}_p-\boldsymbol{k}_s-\boldsymbol{k}_v)\boldsymbol{e}_p\boldsymbol{e}_s \tag{2.8}$$

where $b_{k_v}^{+}$, $a_{k_\lambda}^{+}$, b_{k_v} and a_{k_λ} are the creation and annihilation operators; $\hat{I}$ is the identity

operator; N_0 is the molecules number within the interaction volume V; n_s and n_p are the RI of the medium at the wavelength of the Stokes and pump lasers, respectively; ω_s and ω_p are the angular frequency of the Stokes and pump lasers, respectively; $\boldsymbol{e}_s$ and $\boldsymbol{e}_p$ are the unit vectors representing the light polarization of the Stokes and pump laser and, $\boldsymbol{k}_s$, $\boldsymbol{k}_p$ and $\boldsymbol{k}_v$ are the wave vectors of the Stokes and pump lasers, and the molecular transitions. Similar to the treatment of direct electric dipole, the interaction Hamiltonian H_{int} provides a resonant coupling between the incident laser fields and the molecular transitions. Equations 2.6-2.7 show that the whole system including laser fields and molecules can be described by models of harmonic oscillators.

Following the Fermi's golden rule, the steady state transition rate of Raman transition may be expressed as:

$$W = 2\pi / \hbar \left| \langle i | H_{\text{int}} | g \rangle \right|^2 \rho_{\hbar\omega_i} \tag{2.9}$$

where $\rho_{\hbar\omega_i}$ is the density of the final state $|i\rangle$, $|g\rangle$ is the initial state based on the two-level model which is depicted in Fig. 2.1.

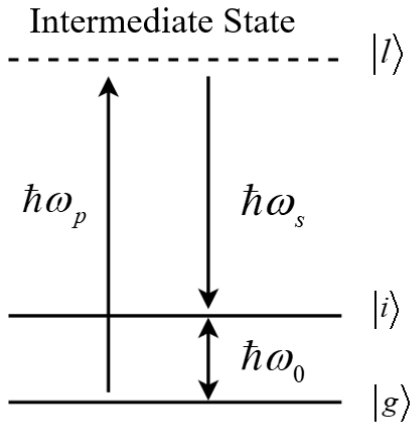

Fig. 2.1 The Raman scattering process based on the two-level model.

To simplify the analysis, we only consider the condition of discrete energy levels and define the initial state $|g\rangle$ in terms of the occupation numbers of the Stokes field N_s, molecules N_v and pump field N_p. The initial state would be: $|g\rangle = |N_s, N_v, N_p\rangle$. Applying the selection rules of the creation and annihilation operators, there are only two possible final states for which W is non-zero: $|i_1\rangle = |N_s + 1, N_v + 1, N_p - 1,\rangle$ and $|i_2\rangle = |N_s + 1, N_v + 1, N_p - 1,\rangle$. The scattering process related to final state $|i_1\rangle$ contributes to the generation of the Stokes photons ($\hbar\omega_p \rightarrow \hbar\omega_0 + \hbar\omega_s$) and the final state $|i_2\rangle$ contributes to the inverse process, in which the Stokes photons are attenuated to generate the pump photons ($\hbar\omega_0 + \hbar\omega_s \rightarrow \hbar\omega_p$). Intuitively, the net rate of the Stokes photons is the difference between the two processes, which is expressed as:

$$\frac{dN_s}{dt} = \rho_0 \left(\frac{\partial \alpha}{\partial r} \right)^2 \frac{4\pi^3}{n_p n_s^2 mc} I_p \sum_{k_s} \frac{\omega_s}{\omega_0} (\boldsymbol{e}_p \boldsymbol{e}_s)^2 (1 + N_s + N_v) \delta(\omega_s - \omega_p + \omega_0) \quad (2.10)$$

where ρ_0 is the molecule density; c is the light speed and I_p is the pump intensity which is defined as:

$$I_p = \hbar\omega_p c / n_p V \sum_{k_p} N_p \quad (2.11)$$

Equation 2.10 describes both the spontaneous and stimulated Raman scattering process. When the presented number of the Stokes photon is negligible, $N_s \ll 1$, the first term of equation 2.10 describes the spontaneous Raman scattering. The second term is then responsible for the stimulated Raman scattering. When large Stokes photons are presented, the number of the Stokes photons increases dramatically. The third term is responsible for the parametric process of the interaction between the laser fields and molecules. However, such process can be neglected in many cases since generally, N_v

is very small and is not much different from that at the thermal equilibrium.

2.1.1 Spontaneous Raman scattering

Here, we assume the polarization of the Stokes laser is the same as the incident pump laser $\boldsymbol{e}_p\boldsymbol{e}_s = 1$ and $N_s \ll 1$ for spontaneous Raman scattering. Neglecting the parametric process, equation 2.9 is reduced to the follows:

$$\frac{dN_s}{dt} = \rho_0 \left(\frac{\partial \alpha}{\partial r}\right)^2 \frac{4\pi^3}{n_p n_s^2 mc} I_p \frac{\omega_s}{\omega_0} \sum_{k_s} \delta(\omega_s - \omega_p + \omega_0) \tag{2.12}$$

The spontaneously scattered Stokes light power into the solid angle $\Delta\Omega$ which has the same polarization of the incident pump laser is calculated to be:

$$P_s = \hbar\omega_s \frac{dn_s}{dt} \tag{2.13}$$

$$= V\rho_0 \left(\frac{\partial \alpha}{\partial r}\right)^2 \frac{\hbar\omega_s^4 n_s}{2c^4 m\omega_0 n_p} I_p \Delta\Omega \tag{2.14}$$

The spontaneous Raman scattering cross section is introduced here:

$$\frac{\partial \sigma}{\partial \Omega} = \left(\frac{\partial \alpha}{\partial r}\right)^2 \frac{\hbar\omega_s^4 n_s}{2c^4 m\omega_0 n_p} \tag{2.15}$$

The spontaneous Raman scattering cross section is typically small, which is on the order of $10^{-30}\,\mathrm{cm}^2$ within the visible band. Applying the perturbation theory, the physical system is perturbed by the incident electromagnetic wave $H_{\mathrm{int}} = -\boldsymbol{p}E$. The spontaneous Stokes light power in equation 2.13 can be rewritten in term of electric dipole interaction:

$$P_s = V\rho_0 \frac{\left|\partial^2 \boldsymbol{p} / \partial t^2\right|^2}{4\pi c^3} \Delta\Omega \tag{2.16}$$

where $\boldsymbol{p}$ is the electric dipole moment. And combine equation 2.13 and 2.16, we get:

$$\left(\frac{\partial\alpha}{\partial r}\right)=\frac{2}{\omega_s^2}\left(\frac{m\omega_0}{\hbar n_s}\right)^{1/2}\left|\frac{\partial^2\boldsymbol{p}/\partial t^2}{E}\right| \tag{2.17}$$

The electric dipole moment may be calculated as [4]:

$$\boldsymbol{p}=\langle g|p|i\rangle=\frac{E}{2\hbar}\sum_l\left(\frac{p_{gl}p_{li}}{\omega_l-\omega_g-\omega_p}+\frac{p_{gl}p_{li}}{\omega_l-\omega_i-\omega_p}\right)\exp\left[-j\left(\omega_i-\omega_g-\omega_p\right)t\right] \tag{2.18}$$

where $p_{gl}=\left\langle\psi_g^0\middle|p\middle|\psi_l^0\right\rangle$ is the dipole matrix elements of the unperturbed system and $|l\rangle$ is the intermediate state. Substitute equation 2.17 with equation 2.18, we get:

$$\left(\frac{\partial\alpha}{\partial r}\right)=\left(\frac{m\omega_0}{\hbar^3 n_s}\right)^{1/2}\left|\sum_l\left(\frac{p_{gl}p_{li}}{\omega_l-\omega_g-\omega_p}+\frac{p_{gl}p_{li}}{\omega_l-\omega_i-\omega_p}\right)\right| \tag{2.19}$$

2.1.2 Stimulated Raman scattering

For the stimulated Raman scattering process, it is important to investigate the generation rate of the Stokes photon with wave vector $\boldsymbol{k}_s$:

$$\frac{dN_s(\boldsymbol{k}_s)}{dt}=\rho_0\left(\frac{\partial\alpha}{\partial r}\right)^2\frac{4\pi^3\omega_s}{n_p n_s^2 mc\omega_0}I_p(1+N_s(\boldsymbol{k}_s))\frac{\Gamma/\pi}{\left(\omega_s-\omega_p+\omega_0\right)^2+\Gamma^2} \tag{2.20}$$

where Γ is the damping rate of the homogeneously broadened molecular transitions induced by a narrow-linewidth pump laser. Again, the polarization of the presented Stokes photons are the same as the incident pump laser. It is interesting to note that when the initial number of the Stokes photons is not large $N_s(\boldsymbol{k}_s)\approx 1$, it grows nonlinearly with the pump intensity. When the initial number of the Stokes photons presented is large $N_s(\boldsymbol{k}_s)\gg 1$, it will grow exponentially as the pump intensity increases:

$$N_s(\boldsymbol{k}_s) \propto \exp(g_R I_p L) \tag{2.21}$$

where L is the light-matter interaction length and g_R is the Raman gain factor which is defined as:

$$g_R(\omega_s) = \rho_0 \left(\frac{\partial \alpha}{\partial r} \right)^2 \frac{4\pi^2 \omega_s}{n_p n_s^2 m c^2 \omega_0} I_p \frac{\Gamma}{\left(\omega_s - \omega_p + \omega_0 \right)^2 + \Gamma^2} \tag{2.22}$$

And the Raman gain factor at Raman resonance would be:

$$g_R(\omega_s) = \rho_0 \left(\frac{\partial \alpha}{\partial r} \right)^2 \frac{4\pi^2 \omega_s}{n_p n_s^2 m c^2 \omega_0 \Gamma} I_p \tag{2.23}$$

Both the scattering cross section and the gain factor of the stimulated Raman scattering depends on the damping rate of the molecular transitions which is quite different from that of the spontaneous Raman scattering in equation 2.15. The stimulated Raman gain factor for several materials are listed in Table 2.1 [5].

2.2 Semiclassical theory of stimulated Raman scattering

In section 2.1, the general theory of the stimulated Raman scattering based on quantum mechanics is introduced. The gain factor and scattering cross section are calculated in the steady state. However, information on the transient process and the individual molecular phase have not been explicitly revealed. In this section, the laser fields will be treated classically using semiclassical theory. The detailed process of the stimulated Raman scattering would be presented, and the time changed coherence of the excited Raman-active medium would be discussed.

Table 2.1 Properties of stimulated Raman scattering for different materials

Substance	Frequency shift (cm^{-1})	Linewidth (cm^{-1})	Gain Factor (G/I_p)
O_2(Liquid)	1552	0.117	145±40
N_2(Liquid)	2326.5	0.067	160±50
Benzene	992	2.15	28
CS_2	655.6	0.5	240
Nitrobenzene	1345	6.6	21
Bromobenzene	1000	1.9	15
Chlorobenzene	1002	1.6	19
Toluene	1003	1.94	12
$NiNbO_3$	256	23	89
$LiTaO_3$	201	22	44

Following the two-level system model depicted in Fig. 2.1, The system Hamiltonian can be written as the sum of the unperturbed system and the Raman interaction:

$$H = H_v - \frac{1}{2}\sum_i \left(\frac{\partial \alpha}{\partial r}\right) r_i \boldsymbol{E}_i \boldsymbol{E}_i \tag{2.24}$$

The wave function representing the *i*th individual molecule is expressed as:

$$\left|\Psi_i\right\rangle = a_i(t)\left|i\right\rangle + b_i(t)\left|g\right\rangle \tag{2.25}$$

The density operator of the molecular system is :

$$\hat{\rho} = \frac{1}{\rho_0}\sum_{i=1}^{\rho_0} \left|\psi_i\right\rangle\left\langle\psi_i\right| \tag{2.26}$$

The time evolved density operator may be expressed as；

$$\frac{\partial \hat{\rho}}{\partial t} = \frac{j}{\hbar}[\hat{\rho}, H] \tag{2.27}$$

where *j* is the imaginary unit. The expectation value of the vibrational coordinate would be:

$$\langle r \rangle = Tr(\hat{\rho} r) = \langle g | \hat{\rho} r | g \rangle + \langle i | \hat{\rho} r | i \rangle \tag{2.28}$$

The time evolved $\langle r \rangle$ and the probability of the population occupying the upper state ρ_{ii} can be expressed as:

$$\frac{\partial \langle r \rangle}{\partial t} + \frac{1}{T_2}\langle r \rangle = j\omega_0 r_{gi}(\rho_{gi} - \rho_{ig}) \tag{2.29}$$

$$\frac{\partial \rho_{ii}}{\partial t} + \frac{1}{T_1}(\rho_{ii} - \bar{N}) = \frac{j}{2\hbar}\frac{\partial \alpha}{\partial r}\boldsymbol{E}^2 r_{ig}(\rho_{gi} - \rho_{ig}) \tag{2.30}$$

where $\bar{N}$ is the mean value of the population occupying the upper state at thermal equilibrium. And two damping terms T_1 and T_2 are introduced, which are responsible for the relaxation related to the interaction between and within the molecules. T_1 reflects the lifetime of the upper excited state and the decay of the stored energy in the molecular system. T_2 represents the dephasing process.

Further, equations 2.29 and 2.30 can be rewritten by eliminating $\rho_{gi} - \rho_{ig}$:

$$\frac{\partial^2 \langle r \rangle}{\partial t^2} + \frac{2}{T_2}\frac{\partial \langle r \rangle}{\partial t} + \omega_0^2 \langle r \rangle = \frac{\omega_0 r_{ig}^2}{\hbar}\left(\frac{\partial \alpha}{\partial r}\right)\boldsymbol{E}\boldsymbol{E}(1 - 2\rho_{ii}) \tag{2.31}$$

$$\frac{\partial \rho_{ii}}{\partial t} + \frac{1}{T_1}\left(\rho_{ii} - \bar{N}\right) = \frac{1}{2\hbar\omega_0}\left(\frac{\partial \alpha}{\partial r}\right)E^2 \frac{\partial \langle r \rangle}{\partial t} \tag{2.32}$$

It is quite obvious that the motion of the molecular system is described a classical damped oscillator model. The driving force of the right term is related to the occupied

population of the upper state. The molecular element of r_{ig} may be approximated as $r_{ig} = \sqrt{\hbar / 2m\omega_0}$ [6]. And if the propagating light field is treated using the classical electromagnetic theory based on Maxwell's equation, the wave equation may be expressed as:

$$\nabla^2 \boldsymbol{E} - \left(\frac{\mu}{c}\right)^2 \frac{\partial^2 \boldsymbol{E}}{\partial t^2} - \frac{\gamma n}{c}\frac{\partial \boldsymbol{E}}{\partial t} = \frac{4\pi}{c^2}\frac{\partial^2 \boldsymbol{P}^{NL}}{\partial t^2} \tag{2.33}$$

where γ is the absorption coefficient which is used to describe the linear loss of the system. $\boldsymbol{P}^{NL}$ represents the nonlinear polarization contribution induced by the incident laser fields. The nonlinear polarization contribution comprises two parts: (a) interaction between the laser fields and the molecules through Raman scattering; (b) other off-resonant molecular transitions:

$$\boldsymbol{P}^{NL} = \rho_0 \left(\frac{\partial \alpha}{\partial r}\right)\langle r \rangle \boldsymbol{E} + \boldsymbol{P}^{NR} \tag{2.34}$$

It should be noted here that the Raman polarizability is treated as a scalar variable in equation 2.34 representing highly polarized Raman scattering. The scattered Stokes photons are polarized in the same direction to the incident laser fields. Polarization perpendicular to the incident laser fields is not contained.

Equations 2.31-2.34 are a complete set of differential equations describing the stimulated Raman scattering process. Reasonable assumptions may be made based on experimental situation to simplify the calculation.

2.2.1 Raman susceptibility

The nonlinear polarizability of Raman scattering process can be described by expanding the polarization as functions of the incident electromagnetic wave. In this section, the interested polarization term is the third-order polarization which is proportional to E^3:

$$P^{NL} = \chi^{(3)}(t)\boldsymbol{EEE} \tag{2.35}$$

where $\chi^{(3)}(t)$ represents the third-order susceptibility evolved in time. To describe the stimulated Raman scattering, it is convenient to express the nonlinear polarization in the frequency domain:

$$\boldsymbol{P}_l^{NL} = \frac{1}{8}\sum_{\substack{m,n,o \\ \alpha,\beta,\gamma}} \chi^{(3)}_{l,m,n,o}\left(-\omega_\delta;\omega_\alpha,\omega_\beta,\omega_\gamma\right)\boldsymbol{E}_m(\omega_\alpha)\boldsymbol{E}_n(\omega_\beta)\boldsymbol{E}_o(\omega_\gamma) \tag{2.36}$$

where the subscripts *l*, *m*, *n*, and represent the x, y, and z direction, and $\omega_\delta = \omega_\alpha + \omega_\beta + \omega_\gamma$. Then the polarization component of $\boldsymbol{P}_l^{NL}(\omega_\delta)$ may be described as:

$$\boldsymbol{P}_l^{NL}(\omega_\delta) = \sum_{m,n,o} \frac{D}{4}\chi^{(3)}_{l,m,n,o}\left(-\omega_\delta;\omega_\alpha,\omega_\beta,\omega_\gamma\right)\boldsymbol{E}_m(\omega_\alpha)\boldsymbol{E}_n(\omega_\beta)\boldsymbol{E}_o(\omega_\gamma) \tag{2.37}$$

where D is the degenerate number, e.g., for all 3 different frequency components, *D*=6; for 2 different frequency components, *D*=3; and for all 3 identical frequency components, *D*=1. The corresponding nonlinear susceptibility can be expressed as:

$$\tilde{\chi}^{(3)}_{l,m,n,o}\left(-\omega_\delta;\omega_\alpha,\omega_\beta,\omega_\gamma\right) = \frac{D}{4}\chi^{(3)}_{l,m,n,o}\left(-\omega_\delta;\omega_\alpha,\omega_\beta,\omega_\gamma\right) \tag{2.38}$$

It holds for the nonlinear susceptibility when changing the order of the frequency components of $\boldsymbol{E}(\omega_\alpha)$, $\boldsymbol{E}(\omega_\beta)$ and $\boldsymbol{E}(\omega_\gamma)$:

$$\tilde{\chi}^{(3)}_{l,m,n,o}\left(-\omega_\delta;\omega_\alpha,\omega_\beta,\omega_\gamma\right) = \tilde{\chi}^{(3)}_{l,m,n,o}\left(-\omega_\delta;\omega_\alpha,\omega_\gamma,\omega_\beta\right) = \tilde{\chi}^{(3)}_{l,m,n,o}\left(-\omega_\delta;\omega_\gamma,\omega_\beta,\omega_\alpha\right) \tag{2.39}$$

Due to the energy conservation, the Raman susceptibility describing the Raman scattering process which generates the Stokes photons can be described in the form of $\tilde{\chi}_R\left(-\omega_s;\omega_p,-\omega_p,\omega_s\right)$.

Actually, the full frequency dependence of the Raman susceptibility is complex and has been investigated in reference [7]. However, in this section, it is convenient to divide $\tilde{\chi}_R$ into two parts: (a) the resonant contribution which occurs when the difference of the ω_p and ω_s is close to the molecular transition ω_0. Near Raman resonance, the resonant Raman susceptibility $\tilde{\chi}_R^{res}$ is strongly frequency-dependent. (b) the non-resonant contribution which contains all the other molecular transitions tuned far away from the Raman resonance. The non-resonant Raman susceptibility $\tilde{\chi}_R^{NR}$ is weakly frequency-dependent. The total Raman susceptibility and the corresponding nonlinear polarization can be expressed as:

$$\tilde{\chi}_R = \tilde{\chi}_R^{res} + \tilde{\chi}_R^{NR} \tag{2.40}$$

$$\boldsymbol{P}^{NL} = \boldsymbol{P}_{res} + \boldsymbol{P}_{NR} \tag{2.41}$$

where

$$\boldsymbol{P}_{res} = \tilde{\chi}_R^{res} EEE \quad \text{and} \quad \boldsymbol{P}_{NR} = \tilde{\chi}_R^{NR} EEE\,. \tag{2.42}$$

In the following, the explicit form of the resonant Raman susceptibility is given to describe the Stokes photons generation. The nonlinear polarization and the Raman susceptibility may be rewritten as [2]:

$$\tilde{P}_{NL}(\omega)\int_{-\infty}^{+\infty} d\omega_p d\omega_s \chi_R(-\omega_s;\omega_p,-\omega_p,\omega_s)E_p(\omega_p)E_p^*(\omega_p)E_s(\omega_s) \tag{2.43}$$

$$\tilde{\chi}_R\left(-\omega_s;\omega_p,-\omega_p,\omega_s\right) = \frac{1}{4m}\left(\frac{\partial\alpha}{\partial r}\right)^2 \frac{\rho_0(1-2N)}{\omega_0^2-(\omega_p-\omega_s)^2+j(\omega_p-\omega_s)/T_2} + \chi_R^{NR} \tag{2.44}$$

The right term of equation 2.44 includes both the resonant and non-resonant contribution of Raman susceptibility. And the resonant part may be furtherly separated into real and imaginary parts as:

$$\tilde{\chi}_R = \chi_{re} + j\chi_{im} + \chi_R^{NR} \tag{2.45}$$

where

$$\chi_{re} = \frac{1}{4m}\rho_0\left(\frac{\partial\alpha}{\partial r}\right)^2 (1-2N)\frac{\omega_0^2 - \left(\omega_p - \omega_s\right)^2}{\left[\omega_0^2 - \left(\omega_p - \omega_s\right)^2\right]^2 + 4\left(\omega_p - \omega_s\right)^2 / T_2^2} \tag{2.46}$$

$$\chi_{im} = \frac{1}{2m}\rho_0\left(\frac{\partial\alpha}{\partial r}\right)^2 (1-2N)\frac{\left(\omega_p - \omega_s\right)/T_2}{\left[\omega_0^2 - \left(\omega_p - \omega_s\right)^2\right]^2 + 4\left(\omega_p - \omega_s\right)^2 / T_2^2} \tag{2.47}$$

Fig. 2.2 depicts the different contributions to the Raman susceptibility and its frequency dependence.

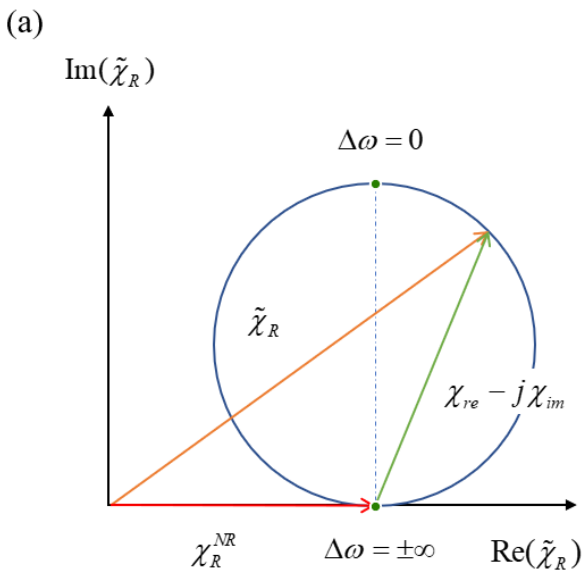

(b)

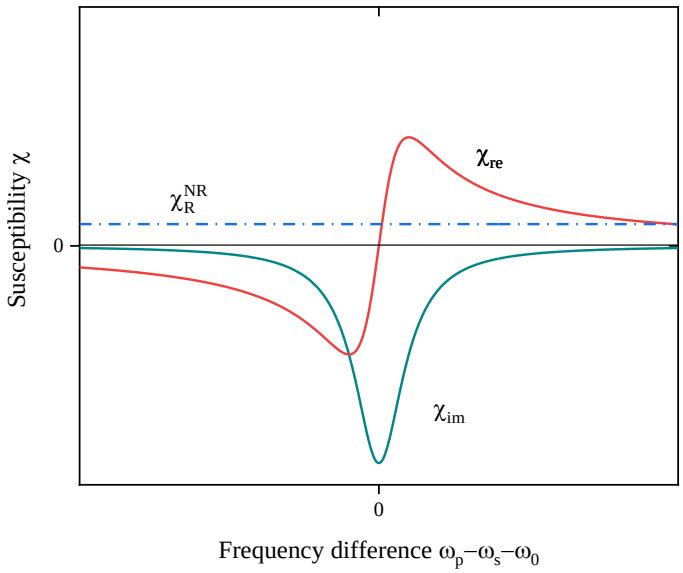

Fig. 2.2 (a) The complex Raman susceptibility and its contributions. Where $\Delta\omega = \omega_p - \omega_s$ is the frequency difference. (b) The frequency-dependent nonlinear susceptibility of the stimulated Raman scattering.

From equations 2.46 and 2.47, it is importantly noted that the imaginary part of the Raman susceptibility is a negative imaginary which is responsible for the Raman gain. The amplitude of the Stokes light under slowly varying envelope condition along its propagating direction may be approximated as:

$$\frac{dE_s}{dz} = -g_s E_s \tag{2.48}$$

where $g_s = -3j\frac{\omega_s}{n_s c}\chi_{im} I_p$ is the optical amplitude change coefficient. Since χ_{im} is pure negative imaginary, g_s is positive and the Stoke field would experience amplification. The real part of the Raman susceptibility determines the Raman-induced RI change. Such RI change may be expressed as:

$$\Delta n_R(\omega_s) = \frac{1}{2n_s}\chi_{re} I_p \tag{2.49}$$

It is interestingly noted that at Raman resonance $\Delta\omega = \omega_p - \omega_s = \omega_0$, the Raman-induced RI change disappears which is essentially different from those RI change modulated by other nonlinear processes, e.g., two photon resonances in third-harmonic generation [8]. If the frequency difference $\Delta\omega$ is tuned from the negative side, the RI change is also negative. If the frequency difference $\Delta\omega$ is tuned from the positive side, the RI change is also positive. It can be concluded that by tuning the frequency difference, both the magnitude and the sign of the induced RI change can be controlled. Near Raman resonance, the RI change can be very steep for Raman transitions with narrow linewidth. Though the magnitude of the RI is small, it can induce significant change of the group RI, which would lead to the modification of the group velocity of the optical pulses.

2.2.2 Coherent Raman scattering with two laser fields

In this section, the most extensively investigated coherent Raman scattering process with two incident laser fields ω_p and ω_s is introduced to experimentally study the characteristics of the Raman gain coefficient. Generally, when the frequency difference approaches the molecular transition, strong interactions between the incident laser fields and the molecular system occurs. Medium molecules can be strongly excited and persisted even after the laser fields are turned off. The incident Stokes light is amplified propagating in the medium with the pump light. Simultaneously, the phase of the Stokes light is also modified by the modulated medium RI induced by Raman scattering. One typical system is shown in Fig. 2.3. Two laser sources are used to generate the Raman scattering. One of them should be frequency-tunable to study the frequency-dependent Stokes amplification.

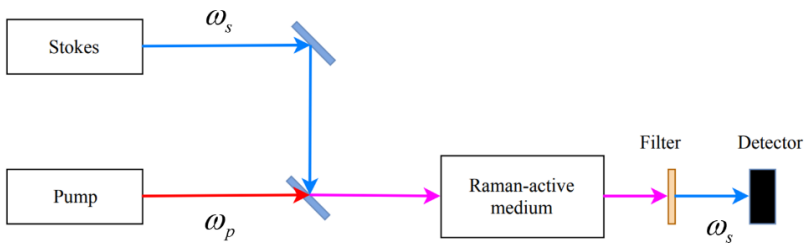

Fig. 2.3 Coherent Raman amplification with two incident laser fields

First, we assume that the incident Stokes laser field is much weaker than the pump field. And the amplification is not too strong that the pump laser is not depleted along the propagation direction. Neglect the optical attenuation of the system, the Stokes light field evolved along the propagating direction can be expressed as:

$$E_s(z) = E_s(0)\exp\left[-\frac{16\pi^2\omega_s}{n_p n_s c^2}\chi_{im} I_p z\right]\exp\left[\frac{16\pi^2\omega_s}{n_p n_s c^2}\chi_{re} I_p z\right] \tag{2.50}$$

where the first exponential term is related to the Stokes amplification and the second term describes the phase modulation of the Stokes light. And the output Stokes light is linearly proportional to the medium length and the incident pump intensity:

$$I_s(L) = I_s(0)\exp\left[g_R I_p L\right] \tag{2.51}$$

The peak value of the gain coefficient and its spectral distribution can be determined by such coherent Raman amplification experimentally:

$$g_R = \frac{1}{I_p L}\ln\left(\frac{I_s(L)}{I_0(L)}\right) \tag{2.52}$$

From equations 2.50 and 2.52, values of the χ_{im} and the Raman cross section are readily available.

Now, the condition of saturating amplification would be discussed in the following part.

The depletion of the pump has to be taken into consideration when the conversion efficiency goes beyond 10%. Neglecting the optical absorption, the saturating Stokes amplification is determined by:

$$\frac{\partial I_s(z)}{\partial z} = g_R I_s I_p \tag{2.53}$$

$$\frac{\partial I_p(z)}{\partial z} = -\frac{\omega_p}{\omega_s} g_R I_s I_p \tag{2.54}$$

Due to the energy conservation, each converted pump photon leads to a Stokes photon, which guarantees the total photon number is constant:

$$\frac{I_p(z)}{\omega_p} + \frac{I_s(z)}{\omega_s} = \frac{I_p(0)}{\omega_p} + \frac{I_s(0)}{\omega_s} \tag{2.55}$$

Combine equation 2.53 with 2.55, it would yield:

$$I_s(z) = \frac{\left[\frac{\omega_s}{\omega_p} I_p(0) + I_s(0)\right] \exp\left[g_R\left(I_p(0) + \frac{\omega_p}{\omega_s} I_s(0)\right) z\right]}{\frac{\omega_s I_p(0)}{\omega_p I_s(0)} + \exp\left[g_R\left(I_p(0) + \frac{\omega_p}{\omega_s} I_s(0)\right) z\right]} \tag{2.56}$$

The maximum Stokes photon conversion efficiency is readily available from equation 2.56:

$$\eta = \frac{I_s(z)}{I_p(0)} \le \frac{\omega_s}{\omega_p} + \frac{I_s(0)}{I_p(0)} \tag{2.57}$$

2.3 Rotational Raman scattering of the diatomic molecules

Pure rotational Raman spectroscopy provides powerful means to determine the molecular structure and to detect gas molecules with high sensitivity and good selectivity. Gas molecules can be excited both vibrational motions and rotational

motions. Most of this section is reviewed based on reference [9]. The vibrational energy levels of the diatomic molecule without rotational motion can be approximated as:

$$E(v) = hc\omega_e(v+1/2) - hc\omega_e x_e(v+1/2)^2 \tag{2.58}$$

where v is the quantum number of the vibrational states (v=0,1,2…); ω_e is the vibration frequency and x_e is the anharmonicity constant. The energy of the diatomic molecules may be given as:

$$E(J) = hcB_v J(J+1) - hcD_v J(J+1)^2 \tag{2.59}$$

where J is the quantum number for vibrational energy levels; B_v and D_v are rotational constant for vibration state v and the centrifugal constant. The rotation constant is defined as:

$$B_v = \frac{h}{8\pi^2 c}\left\langle \frac{1}{I_v} \right\rangle_{av} \tag{2.60}$$

where $\left\langle \frac{1}{I_v} \right\rangle_{av}$ is the average value of the reciprocal of the inertial moment of the vibration states. The centrifugal constant is defined as:

$$D_v = \frac{4B_v^3}{\omega_v^2} \tag{2.61}$$

where $\omega_v = (\omega_e - \omega_e x_e) - 2\omega_e x_e$. And for many cases, D_v can be neglected since it is much smaller than B_v. Hence the second term of the right part of equation 2.59 can be dropped when J is not large. It is clear from the theoretical SRS process stated in the previous section that the scattered Stokes light frequency is described as:

$$\omega_s = \omega_p - \frac{E(J) - E(J')}{h} \tag{2.62}$$

Given the selection rule $\Delta J=J-J'=\pm 2$, of which, Stokes lines take transition form of $J \rightarrow J+2$ while anti-Stokes lines take transition form of $J \rightarrow J-2$, Raman transition shift can be expressed as:

$$\left|\Delta\omega(J)\right| = \left(4B_v - 6D_v\right)\left(J+3/2\right) - 8D_v\left(J+3/2\right)^2 \tag{2.63}$$

where J = 0,1,2… for the Stokes light generation and J = 2,3,4… for the anti-Stokes light generation. Since D_v is neglectable compared with B_v, the frequency space of the different rotational Raman transitions is approximately to be $4B_v$. The energy levels and the corresponding rotational Raman spectrum of diatomic molecules are depicted in Fig. 2.4.

(a)

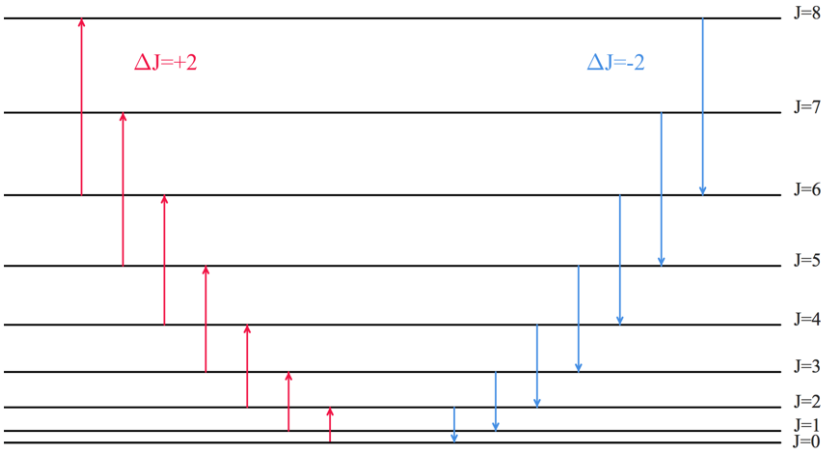

(b)

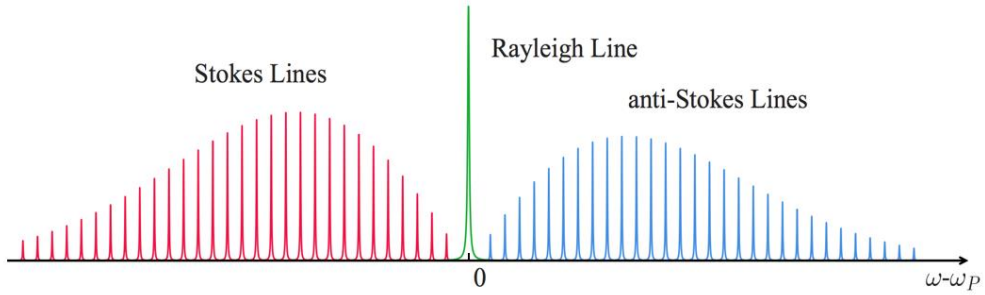

Fig. 2.4 Diagram of Raman transition energy levels and rotational Raman spectrum. (a) The first 8 energy levels involved in rotational Raman transitions where the application of selection rule $J \rightarrow J+2$ for Stokes lines and $J \rightarrow J-2$ for anti-Stokes lines. (b) The corresponding rotational Raman spectrum where ω is frequency of the scattered light and J is from 0 to 30.

The intensity of the Raman spectrum lines is given as:

$$I(J) \cong D_n S_J \exp\left[-\frac{E(J)}{kT}\right] \tag{2.64}$$

where k is Boltzmann's constant; T is the absolute temperature; D_n is the nuclear degeneracy number and $S_J = (J+1)(J+2)/(2J+1)$ for Stokes lines and $S_J = J(J-1)/(2J-1)$ for anti-Stokes lines. To calculate the value of the nuclear degeneracy of different Raman transitions, a full investigation of the wave function of the molecular system are discussed in the following part. The total wave function of the diatomic molecule may be written as:

$$\psi = \psi_e \psi_v \psi_r \psi_n \tag{2.65}$$

where the subscripts e, v, r and n represent the electric, vibrational, rotational and nuclear wave function, respectively. Now, we consider imposing the nuclear interchange on the complete wave function which transfers the coordinates in the way of

$\hat{i}\left[\psi(x,y,z)\right]=\psi(x,y,z)$ and $\hat{i}$ is the interchange operator. It is demonstrated that molecular wave functions with electric states of Σ_g^+, Σ_μ^-, ρ_g^+ and ρ_μ^- are symmetric while with electric states of Σ_g^-, Σ_μ^+, ρ_g^- and ρ_μ^+ are antisymmetric [10]:

$$\hat{i}\left[\psi_e(\Sigma_g^+)\right]=\psi_e(\Sigma_g^+) \tag{2.66}$$

$$\hat{i}\left[\psi_e(\Sigma_g^-)\right]=-\psi_e(\Sigma_g^-) \tag{2.67}$$

The vibrational wave function which depends on the bond distance is not affected by the interchange operator:

$$\hat{i}\left[\psi_v\right]=-\psi_v \tag{2.68}$$

The rotational wave functions are symmetric for the even J and antisymmetric for the odd J:

$$\hat{i}\left[\psi_r(J_{even})\right]=\psi_r(J_{even}) \tag{2.69}$$

$$\hat{i}\left[\psi_r(J_{odd})\right]=-\psi_r(J_{odd}) \tag{2.70}$$

The effect of the nuclear interchange may be demonstrated with a diatomic molecule with 1/2 spin. The spin eigenfunctions are S^+ and S^-, and the complete nuclear wave functions are [1]:

$$\begin{bmatrix}\psi_{n1}\\ \psi_{n2}\\ \psi_{n3}\\ \psi_{n4}\end{bmatrix}=\begin{bmatrix}S_1^+S_2^+\\ S_1^-S_2^-\\ \left(S_1^+S_2^- + S_2^+S_1^-\right)/\sqrt{2}\\ \left(S_1^+S_2^- - S_2^+S_1^-\right)/\sqrt{2}\end{bmatrix} \tag{2.71}$$

and

$$\hat{i}\begin{bmatrix}\psi_{n1}\\ \psi_{n2}\\ \psi_{n3}\\ \psi_{n4}\end{bmatrix}=\begin{bmatrix}\psi_{n1}\\ \psi_{n2}\\ \psi_{n3}\\ -\psi_{n4}\end{bmatrix} \tag{2.72}$$

For the 1/2 spin, three nuclear wave functions are symmetric and one nuclear wave function is antisymmetric. The number of different symmetric and antisymmetric nuclear wave functions that can be constructed for other nuclear spins depends on the nuclear spin.

Based on the Pauli exclusion, impose the interchange operator on the total wave functions of the Bosons, in which case the molecules are integer spin, the total wave function would be unchanged. However, impose the interchange operator on the total wave functions of the fermions, in which case the molecules are half-integer spin, the total wave function would change the sign. Thus, the total wave function should obey the following principles:

$$\hat{i}\left[\psi^{B}\right]=\psi^{B} \tag{2.73}$$

$$\hat{i}\left[\psi^{F}\right]=-\psi^{F} \tag{2.74}$$

For example, the diatomic molecules with 1/2 spin and the ground state of Σ_g^+, the total wave functions can be constructed as:

$$\psi=\psi_e\psi_v\psi_r\left(J_{odd}\right)\begin{bmatrix}\psi_{n1}\\ \psi_{n2}\\ \psi_{n3}\end{bmatrix} \tag{2.75}$$

$$\psi=\psi_e\psi_v\psi_r\left(J_{even}\right)\psi_{n4} \tag{2.76}$$

For Fermions, the total wave functions with odd *J* energy levels are combined with the symmetric nuclear wave functions and the total wave functions with even *J* energy

levels are combined with the antisymmetric nuclear wave functions. Contrarily, for Bosons, the total wave functions with odd *J* energy levels are combined with the antisymmetric nuclear wave functions and the total wave functions with even *J* energy levels are combined with the symmetric nuclear wave functions. As a result, the rotational Raman scattering is enhanced with a larger degenerate number, i.e., the rotational Raman scattering of the odd *J* levels are 3 times as strong as that originated from the even *J* levels for 1/2 spin molecules. Table 2.2 lists the degenerate number for molecules for different spin number and the molecular data for calculation of the rotational Raman lines.

Table 2.2 Molecular data for different diatomic molecules [9]

Molecule	B_e (cm^{-1})	ω_e (cm^{-1})	$\omega_e x_e$ (cm^{-1})	α_e (cm^{-1})	r_e (Å)	**Nuclear Spin**	J_{even}	J_{odd}
$^{1}H_2$	60.8	4395	117	2.99	0.742	1/2	1	3
$^{2}H_2$	30.43	3118	64.1	1.05	0.742	1	6	3
$^{14}N_2$	2.010	2360	14.64	0.0187	1.094	1	6	3
$^{16}O_2$	1.446	1580	12.07	0.0158	1.207	0	0	1
$^{19}F_2$	0.86	892	--	--	1.435	1/2	1	3
$^{35}Cl_2$	0.2438	565	4	0.0017	1.988	3/2	6	10

The rotational Raman lines of hydrogen are shown in Fig. 2.5.

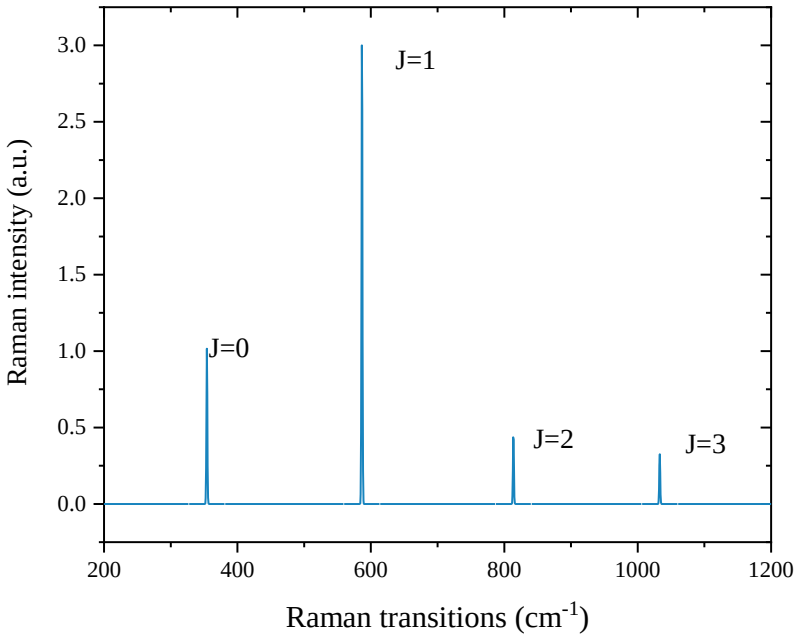

Fig. 2.5 The calculated rotational Raman spectrum of the hydrogen molecules

2.4 Summary

In this chapter, the stimulated Raman scattering process of the light-molecule interactions are introduced based on quantum mechanics theory. Raman susceptibility and the coherent Raman amplification are investigated using semiclassical theory. And the rotational Raman scattering of the diatomic gas molecules are calculated based on the total wave functions of the quantum mechanics theory. The results provide theoretical guidance for developing rotational Raman spectroscopy aiming for sensitive gas detection.

References

1. C. Cohen-Tannoudji, B. Diu, F. Laloë, J. Balla, and J. Streubel , *Quantenmechanik. Band 1*. (Walter de Gruyter, 2007).

2. A. Penzkofer, A. Laubereau, and W. Kaiser, "High intensity Raman interactions," Prog. Quantum Electron. **6**(2), 55–140 (1979).

3. C.-S. Wang, "Theory of stimulated Raman scattering," Phys. Rev. **182**(2), 482 (1969).

4. J. A. Koningstein, *Introduction to the Theory of the Raman Effect* (Reidel, 1972).

5. G. Agrawal and G. Agrawal, "Chapter 8 – Stimulated Raman Scattering," in *Nonlinear Fiber Optics* (2013), pp. 295–352.

6. and W. K. Giordmaine, Joseph A., "Driven Lattice Vibrations* J.," Phys. Rev. **144**(2), 676 (1966).

7. R. Glauber, *Quantum Optics* (Academic Press, 1969).

8. Guang S. He and Song H. Liu, *Physics of Nonlinear Optics* (WORLD SCIENTIFIC, 2000).

9. L. C. Hoskins, "Pure rotational Raman spectroscopy of diatomic molecules," J. Chem. Educ. **52**(9), 568 (1975).

10. I. Levine, *Quantum Chemistry. Volume II: Molecular Spectroscopy* (1970).

Chapter 3: Theory of Stimulated Raman Dispersion Spectroscopy

3.1 Introduction

Laser absorption spectroscopy (LAS) and its derivatives (e.g. photothermal and photoacoustic spectroscopy) are powerful techniques for energy and safety applications [1–3]. Probing absorptions of laser beams tuned to the molecular "finger-print" absorption lines offer chemical detection with high sensitivity and selectivity. However, sensors based on LAS are not suitable for molecules that have no absorptions within the operating wavelength range of the available lasers.

Stimulated Raman spectroscopy is a versatile technique for detecting trace chemicals that do not rely on the absorption lines of the targeted molecules. It has been widely applied for chemical identification and detection [4]. However, these reported works all investigated features of SRS using intensity-based measurement of the Raman gain. Information of molecules (e.g. concentration) is directly encoded in the amplitude of the received light, which is susceptible to light intensity fluctuation and hence fundamentally prevents the further improvement of the limit-of-detection (LOD).

It has been reported previously that the laser absorption spectroscopy sensors based on molecular dispersion have better immunity to intensity noise as well as a larger dynamic range over the intensity-based measurement [5–7]. The SRS-induced dispersion based stimulated Raman spectroscopy, is expected to provide the same advantages. We name this technique as stimulated Raman dispersion spectroscopy (SRDS). The SRS-induced dispersion is retrieved by measurement of the accumulated phase change using a stabilized interferometer, which offers extra benefit: the SRS-induced dispersion can be modulated by modulating the pump beam, which allows the use of a fixed probe with a

stabilized fiber interferometer to minimize the system noise and fluctuations resulting from a modulated probe beam. In this chapter, fundamentals of SRDS are presented, including models for deriving spectral signals, details of system implementation and detection optimization.

3.2 Theory

A pump laser beam (ω_{pump}) and a weaker probe laser beam (ω_{probe}) are co-propagating in the gas medium. When the frequency difference between the two laser beams is in the near a molecular Raman transition (ω_0) of gases, SRS induces a complex RI modulation of the gas material [8]:

$$\Delta n(\omega_{probe}) = -i\frac{cg_0 I_{pump}}{2\omega_{probe}\left\{1-i2\left[\omega_0-\left(\omega_{pump}-\omega_{probe}\right)\right]/\Gamma_R\right\}} \tag{3.1}$$

where $\Gamma/2\pi$ is the linewidth of the Raman resonance, c is light speed, g_0 is the peak gain coefficient that is proportional to gas concentration (C) and I_{pump} is the pump light intensity. The pump and probe beams interact with gas molecules, resulting in energy transfer from pump to probe and inducing a sharp RI (dispersion) change near the Stokes frequency, as illustrated in Fig. 3.1. The gain experienced by the probe beam is proportional to the imaginary part of $\Delta n(\omega_{probe})$, while the dispersion is related to the real part of $\Delta n(\omega_{probe})$. The steep variation of the Raman-induced dispersion illustrated in Fig. 3.1 can significantly modify the group RI of the probe beam and can effectively change the group velocity of the probe pulses near the Stokes wavelength. Optical pulses delay may be manipulated by tuning Raman-induced dispersion. Raman scattering in gases is extremely weak. However, the use of a HC-PCF enables tighter light field confinement, nearly perfect overlap of gas sample with light fields and long length for

light-gas interaction [4,9–11], which greatly enhances the Raman-induced dispersion.

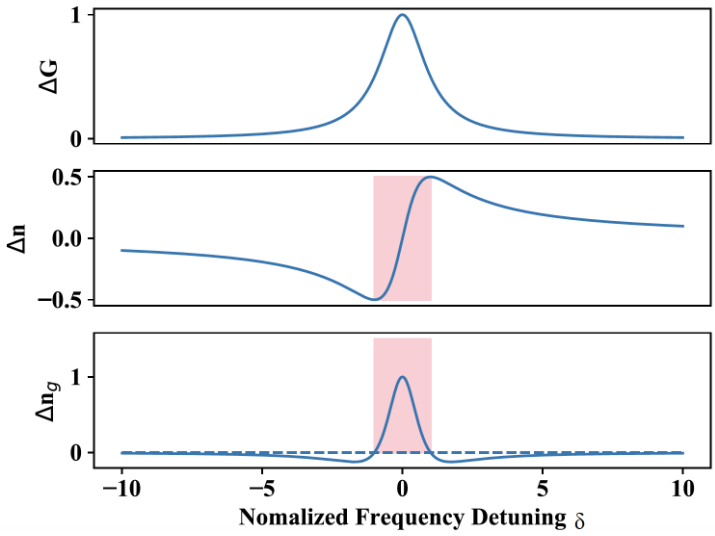

Fig. 3.1 The probe light experiences Raman gain (ΔG), RI change (Δn) and group RI change (Δn_g) at the vicinity of Stokes frequency ω_{Stokes}. $\delta = 2\left[\omega_0 - \left(\omega_{pump} - \omega_{probe}\right)\right]/\Gamma_R$. The shaded pink area indicates the linewidth of Raman resonance, which corresponds to $-1 \le \delta \le 1$.

Tuning of the laser induced dispersion with SRS in a gas-filled optical fiber has great flexibility. Firstly, the spectral location of the induced dispersion, being determined by $\omega_{Stokes} = \omega_{pump} - \omega_0$, can be tuned by varying the pump wavelength. The possibility of exciting multiple Raman transitions simultaneously in a hollow-core fiber filled with single or multiple gases with different concentration and by use of single or multiple pump sources would enable dispersion control at multiple spectral locations over a wide wavelength range. By using hollow-core fiber with wide transmission window (e.g., anti-resonant hollow-core fiber) covering multi-Raman transitions, highly sensitive multi-gases detection may be realized. Secondly, the Raman linewidth as well as the peak gain coefficient g_0 are gas-pressure dependent, which provides another degree of freedom to control the magnitude and spectral range of the induced dispersion, giving us extra flexibility for dynamically tuning Raman-induced dispersion. The pump light

intensity as well as the length of gas-filled fiber can also be adjusted to control the magnitude of dispersion.

3.3 Measurement of the Raman-induced Dispersion

In traditional Raman spectroscopy, a pump beam is used to excite the sample, and the amplification of the probe light around Stokes wavelength is measured to extract molecular information. However, in SRDS, a pump beam is used to modify the RI of sample medium and induce the phase modulation of the probe beam. The accumulated phase change of the probe beam over length L can be expressed as:

$$f_D(d) = \frac{2p}{l_{probe}} \mathrm{Re}\left[\Delta n(w_{probe}) \right] L = \left(\frac{d}{1+d^2} \right) \Delta f , \tag{3.2}$$

where L is interaction length of pump beam, probe beam and sample medium; the $\delta = 2\left[\omega_0 - \left(\omega_{pump} - \omega_{probe} \right) \right] / \Gamma_R$ is the linewidth-normalized frequency detuning parameter and $\Delta\phi = G/2$ is the peak phase change which is related to the accumulated gain $G = g_0 I_{pump} L$ at the Raman resonance.

3.3.1 Wavelength Modulation Method

Wavelength modulation method with harmonic signal detection is a powerful technology and employed widely for weak signal detection with high sensitivity [12]. To improve the signal-to-noise-ratio (SNR) of the measurement of the Raman-induced dispersion, we use a wavelength-modulated pump light to modulate the probe beam phase. The pump beam wavelength is sinusoidally modulated at high frequency (e.g. 50 kHz) and at the same time slowly scanned so that the wavelength difference between the pump and probe beam is tuned across Raman transition of sample medium. This modulated phase of the probe beam includes harmonic components of the modulation frequency. The

phase modulation is then converted to intensity modulation by an optical interferometer. The harmonic components of the interferometer output, which is linearly proportional to the harmonic components of the probe light phase modulation, is lock-in detected and used as the system output.

3.3.2 Modeling Harmonic Signal Spectra

Wavelength modulating pump light with $\omega(t)=\omega_{pump}+\Delta\omega_m \sin(\omega_m t)$, where Δw_m is the amplitude and w_m the frequency of wavelength modulation. Then equation 3.2 can be rewritten as:

$$\phi_D(t,\delta)=\left(\frac{\delta+\delta_m\cos(\omega_m t)}{1+\left(\delta+\delta_m\cos(\omega_m t)\right)^2}\right)\Delta\phi \tag{3.3}$$

where $\delta_m=2\Delta\omega_m/\Gamma_R$ is the linewidth-normalized wavelength modulation depth.

To determine the detected harmonic signal spectra of the wavelength modulated SRDS, equation 3.3 can be expanded in

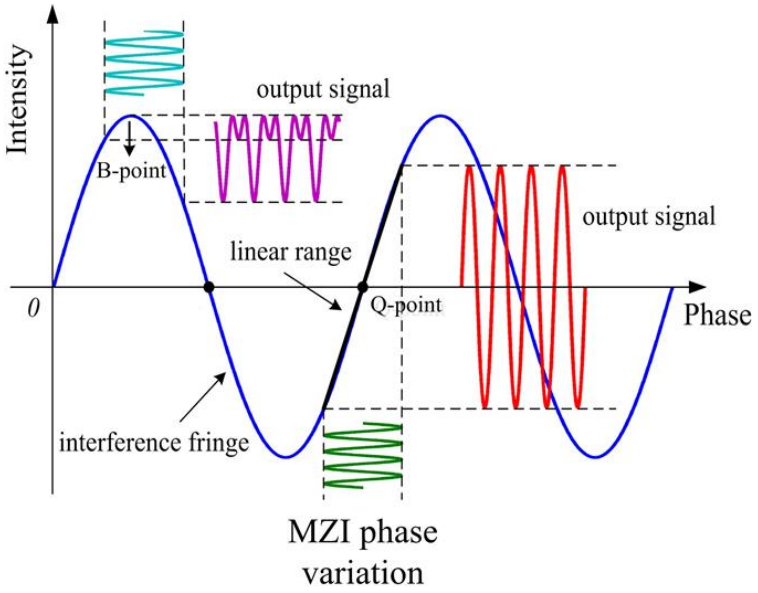

Fig.3.2 The illustration of the output signal of the interferometer as a function of the modulated phase signal.

terms of Fourier series by Fourier transformation. For dilute trace chemical detection, due to the small molecular density, the Raman gain and the phase change may be very small with low pump light intensity (i.e., $G \quad 1$ and $\phi_D(t,\delta) \ll 1$). Assuming at the quadrature of the interferometer shown in Fig. 3.2, i.e., $\sin(f_D(t,d)) \gg f_D(t,d)$, the detected signal of the photodetector can be expressed as:

$$i_{PD} \propto \mathrm{D}f\left(\frac{d + d_m\cos(w_m t)}{1+\left(d + d_m\cos(w_m t)\right)^2}\right) \tag{3.4}$$

To derive the harmonic components of equation 3.3 and 3.4, we first calculate the Fourier transform of the unmodulated phase change given in equation 3.2. Denoting the Fourier transform of $\phi_D(\delta)$ by $\varphi(\tau)$ and define it as：

$$\varphi(\tau) = \frac{1}{\sqrt{2\pi}}\int_{-\infty}^{+\infty}\phi_D(\delta)\exp(-i\delta\tau)d\delta = -i\Delta\phi\sqrt{\frac{\pi}{2}}\exp(-|\tau|) \tag{3.5}$$

where t is the conjugate variable of d. Here, applying Fourier transform pair：

$$f(t)\exp(i\omega_0 t) \leftrightarrow F(\omega-\omega_0) \tag{3.6}$$

and equation 3.5 to equation 3.3, the time-dependent of Fourier transform of the modulated phase change is given as:

$$j(t,t) = j(t)\exp[id_m t\cos(w_m t)] \tag{3.7}$$

Equation 3.7 can be expanded into a sum of harmonic signals of the pump wavelength modulation frequency using Jacobi-Anger formula:

$$\varphi(\tau,t)=\sum_{n=0}^{\infty}(2-\sigma_{n0})i^{n}\varphi(\tau)J_{n}(\delta_{m}\tau)\cos(n\omega_{m}t) \tag{3.8}$$

where σ_{n0} is the Kronecker's delta function ($\sigma_{n0}=0$ if $n\neq 0$; $\sigma_{n0}=1$ if $n=0$.) and J_n is the *n*th Bessel function. Inversely transform equation 3.8, the modulated SRS-induced phase change of equation 3.3 and the detected signal of equation 3.4 can be denoted as:

$$\phi_{D}(\delta,t)=\Delta\phi\sum_{n=0}^{\infty}c_{n}(\delta,\delta_{m})\cos(n\omega_{m}t) \tag{3.9-a}$$

$$i_{PD}\propto 4E_{sig}E_{ref}\Delta\phi\sum_{n=0}^{\infty}c_{n}(\delta,\delta_{m})\cos(n\omega_{m}t) \tag{3.9-b}$$

where $c_n(\delta,\delta_m)$ is the *n*th Fourier coefficient of the modulated SRS-induced phase change:

$$c_{n}(\delta,\delta_{m})=-\frac{1}{2}(2-\sigma_{n0})\int_{-\infty}^{+\infty}i^{n+1}\exp(-|\tau|)J_{n}(\delta_{m}\tau)d\tau \tag{3.10}$$

Though equation 3.10 shares similar formality with *n*th Fourier coefficients for a Lorentzian absorption/gain line-shape function, the derivation procedure for an analytical expression is mathematically different. Following the derivation in reference [13], $c_n(\delta,\delta_m)$ can be rewritten as:

$$c_{n}(\delta,\delta_{m})=-\mathrm{Re}[(2-\sigma_{n,0})\frac{i^{n+1}\left\{\sqrt{(1-i\delta)^{2}+\delta_{m}^{2}}-(1-i\delta)\right\}^{n}}{\delta_{m}^{n}\sqrt{(1-i\delta)^{2}+\delta_{m}^{2}}}] \tag{3.11}$$

However, equation 3.11 is in the form of complex which is not convenient for direct calculation. It is possible to derive the non-complex form of $c_n(\delta,\delta_m)$ and use it for simulation and curve-fitting based on methods introduced in reference [13]. The $c_n(\delta,\delta_m)$ may be rewritten in the following form [13]:

$$c_n(\delta,\delta_m) = -\frac{A_n}{\delta_m^n}\left[B_n + \frac{C_n S_+ + D_n S_-}{\sqrt{2}R}\right] \tag{3.12}$$

where $S_\pm$ are defined as $S_\pm = \sqrt{R \pm M}$, and in turn, $R = \sqrt{M^2 + 4\delta^2}$ and $M = 1 + \delta_m^2 - \delta^2$. Coefficients of A_n, B_n, C_n and D_n are defined as [13]:

$$A_n = 2 - \sigma_{n0} \tag{3.13}$$

$$\begin{aligned} B_n = &\sum_{a=0}^{a_{\max}} \sum_{b=0}^{a} \sum_{r=0}^{a-b} \sum_{s=0}^{r} \sum_{c=c_{\min}}^{c_{\max}} [(-1)^{a-b-r+c-1} \binom{n}{n-2a-1} \\ &\times \binom{a}{b}\binom{a-b}{r}\binom{r}{s}\binom{n-2a-1}{2c-n-b-1} 2^b \delta_m^{2s} \delta^{2(a-b-r+c)-n-1}] \end{aligned} \tag{3.14}$$

$$\begin{aligned} C_n = &\sum_{d=0}^{d_{\max}} \sum_{e=0}^{d} \sum_{r=0}^{d-e} \sum_{s=0}^{r} \sum_{f=f_{\min}}^{f_{\max}} [(-1)^{d-e-r+f-1} \binom{n}{n-2d} \\ &\times \binom{d}{e}\binom{d-e}{r}\binom{r}{s}\binom{n-d}{2f-n-e-1} 2^e \delta_m^{2s} \delta^{2(d-e-r+f)-n-1}] \end{aligned} \tag{3.15}$$

$$\begin{aligned} D_n = -sign(\delta) &\sum_{d=0}^{d_{\max}} \sum_{e=0}^{d} \sum_{r=0}^{d-e} \sum_{s=0}^{r} \sum_{g=g_{\min}}^{g_{\max}} [(-1)^{d-e-r+g} \binom{n}{n-2d} \\ &\times \binom{d}{e}\binom{d-e}{r}\binom{r}{s}\binom{n-d}{2g-n-e} 2^e \delta_m^{2s} \delta^{2(d-e-r+g)-n}] \end{aligned} \tag{3.16}$$

where coefficients $a_{\max}$, $c_{\min}$, $c_{\max}$, $d_{\max}$, $f_{\min}$, $f_{\max}$, $g_{\min}$ and $g_{\max}$ are given in Table 3.1 [13]:

Table 3.1 Definitions of coefficients used in equations 3.14-3.16

Coefficients	Definitions [a]
$a_{\max}$	$Int^-\left(\frac{n-1}{2}\right)$
$c_{\min}$	$Int^+\left(\frac{n+b-1}{2}\right)$
$c_{\max}$	$n-a+Int^-\left(\frac{b-2}{2}\right)$

$d_{\max}$	$Int^{-}\left(\frac{n}{2}\right)$
$f_{\min}$	$Int^{+}\left(\frac{n+e+1}{2}\right)$
$f_{\max}$	$n-d+Int^{-}\left(\frac{e+1}{2}\right)$
$g_{\min}$	$Int^{+}\left(\frac{n+e}{2}\right)$
$g_{\max}$	$n-d+Int^{-}\left(\frac{e}{2}\right)$

[a] *Functions of* $Int^{\pm}(x)$ *are defined as* $sign(x)ceil(|x|)$ *and* $sign(x)\,floor(|x|)$, *respectively, where* $sign(x)=-1$ *if* $x<1$ *and* $sign(x)=1$ *if* $x>1$. $ceil(x)$ *and* $floor(x)$ *extract the nearest integer of the variable x.*

For the convenience of the simulation, analytical results of B_n, C_n and D_n to derive the first four Fourier coefficients $c_n(\delta,\delta_m)$ are listed in Table 3.2.

3.3.3 Optimization of Modulation Depth

For wavelength modulated SRDS, only the first few harmonic signals are practical useful due to their larger signal amplitude. And among all these harmonic signals, the second harmonic (2*f*) has the largest SNR [12]. To briefly discussed the deduced harmonic components of the modulated dispersion signal, the first harmonic Fourier coefficient $c_1(\delta,\delta_m)$ is explicitly given as based on Equations 3.12-3.16:

Table 3.2 Expressions for the first 4 B_n, C_n and D_n coefficients

B_n	Definitions	C_n	Definitions	D_n	Definitions
B_1	-1	C_1	1	D_1	$sign(\delta)\delta$
B_2	2δ	C_2	-4δ	D_2	$-sign(\delta)(-2-\delta_m^2+2\delta^2)$
B_3	$4+\delta_m^2-4\delta^2$	C_3	$-4-3\delta_m^2+12\delta^2$	D_3	$-sign(\delta)(12\delta+3\delta_m^2\delta-4\delta^3)$
B_4	$-24\delta-4\delta_m^2\delta+8\delta^3$	C_4	$32\delta+16\delta_m^2\delta-32\delta^3$	D_4	$-sign(\delta)(8+8\delta_m^2+\delta_m^4$ $-48\delta^2-8\delta_m^2\delta^2+8\delta^4)$

$$c_1(\delta,\delta_m)=\frac{2}{\delta_m}\left[1-\frac{S_+ +|\delta|S_-}{\sqrt{2}R}\right] \tag{3.17}$$

If the normalized frequency detuning is set to be 0 ($\delta=0$), the value of $c_1(\delta=0,\delta_m)$ at Raman resonance can be written as:

$$c_1(\delta=0,\delta_m)=\frac{2}{\delta_m}\left[1-\frac{1}{\sqrt{1+\delta_m^2}}\right] \tag{3.18}$$

From equation 3.18, the value of $c_1(\delta,\delta_m)$ at Raman resonance is a function of the phase modulation depth and reaches the maximum when $\delta_m=\sqrt{1+\sqrt{5}}/\sqrt{2}\approx 1.27$.

Similarly, the maximal amplitudes can be determined for other harmonic Fourier coefficients with an optimal modulation depth. Here, we investigated the relationship between the modulation depth and the maximum value of $c_n(\delta,\delta_m)$. In Fig 3.3(a) and (b), the maximum values of the first four Fourier coefficients as functions of δ_m are depicted and the optimal modulation depth δ_m^{opt} can be extracted. The optimal modulation depths δ_m^{opt} are 1.27, 2.84, 3.15 and 4.44 for c_1, c_2, c_3 and c_4 respectively.

(a)

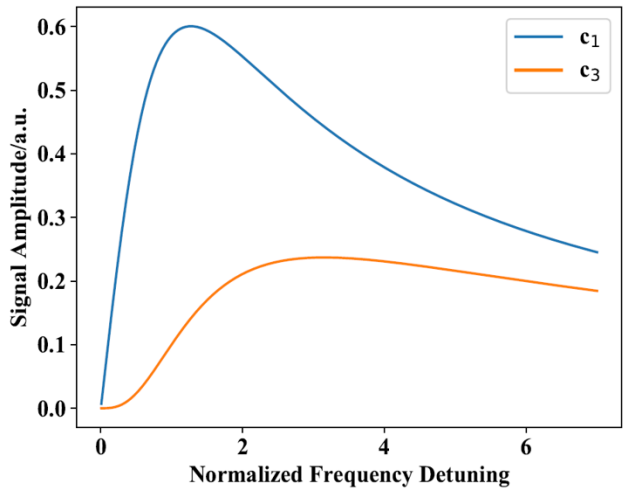

(b)

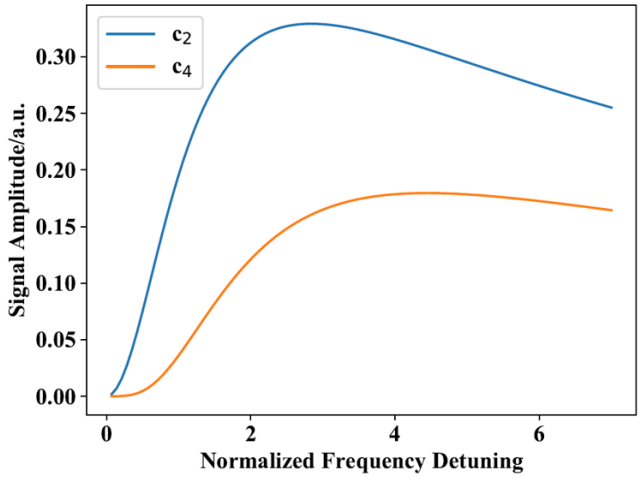

Fig. 3.3 (a) The maximum value of the first and third Fourier coefficient c_1 and c_3 as a function of the normalized modulation depth δ_m. The optimal modulation is extracted numerically as 1.27 and 3.15 respectively. (b) The maximum value of the second and fourth Fourier coefficient c_2 and c_4 as a function of the normalized modulation depth δ_m. The optimal modulation is extracted numerically as 2.84 and 4.44 respectively.

The line shapes of the first four Fourier coefficients as functions of the normalized detuning with the corresponding optimal modulation depth are depicted in Fig. 3.4 (a)

and (b). Odd Fourier coefficients are symmetric functions with maximum values locate at Raman resonance while even Fourier coefficients are anti-symmetric functions with maximum values locate shift from Raman resonance. Hence, the maximum value of the 1*f* and 2*f* component of the Raman-induced phase change can be expressed as:

$$f_D^{1f}(t)_{\max} = \Delta f c_1(d = 0, d_m = 1.272)\cos(w_m t) = 0.6\Delta f \cos(w_m t) \tag{3.19}$$

$$f_D^{2f}(t)_{\max} = \Delta f c_2(d = 1.792, d_m = 2.84)\cos(2w_m t) = 0.33\Delta f \cos(2w_m t) \tag{3.20}$$

Since the line shape of the 2*f* component is anti-symmetric to the Raman resonance, $\phi_D^{2f}(t)$ reaches its minimum value when $\delta = 1.792, \delta_m = 2.84$ and giving:

$$f_D^{2f}(t)_{\min} = \Delta f c_2(d = -1.792, d_m = 2.84)\cos(2w_m t) = -0.33\Delta f \cos(2w_m t) \tag{3.21}$$

Note that the optimized modulation depth $\delta_m = 2.84$ obtained here for SRDS is nearly 30% larger than that used for wavelength modulated LAS ($\delta_m = 2.2$), which is due to the different line shape function used for derivation of the *n*th Fourier coefficients. The Lorentz function ($f(x) = 1/(1+x^2)$) is used for the wavelength modulated LAS, while the Lorentz function ($f(x) = x/(1+x^2)$) is used for the wavelength modulated SRDS.

(a)

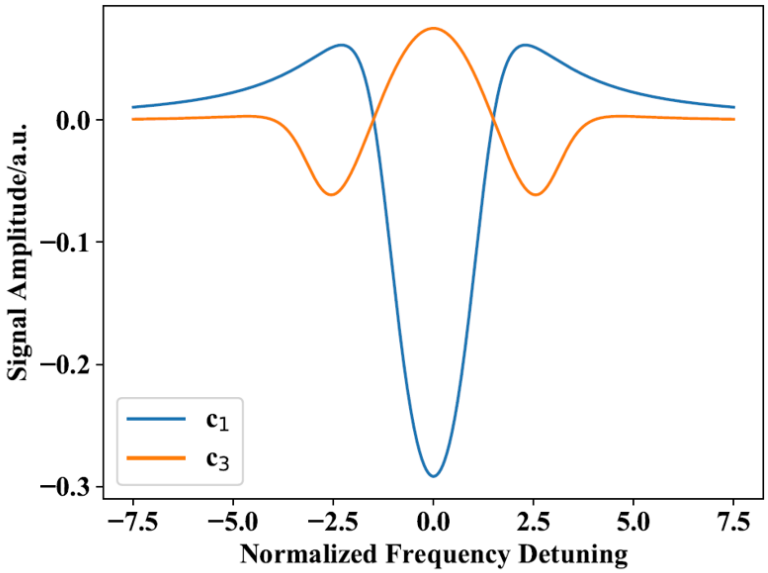

(b)

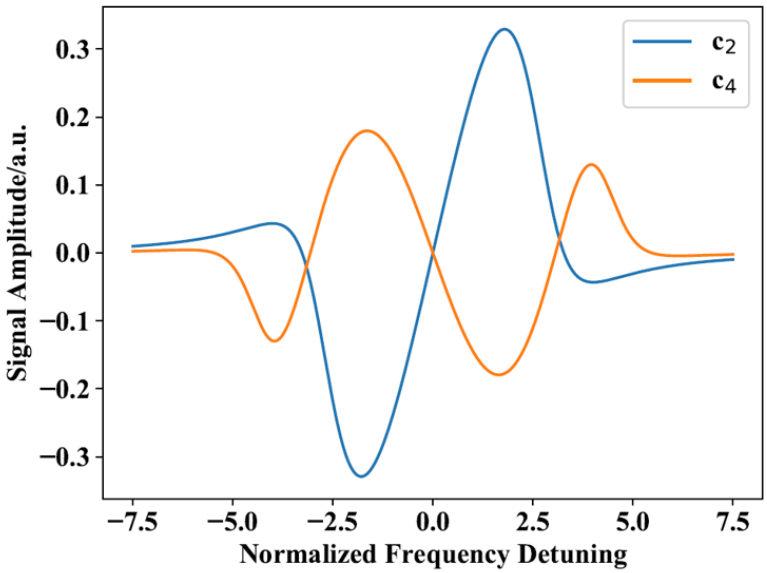

Fig. 3.4 (a) The line shape of the first and third Fourier coefficient c_1 and c_3 as a function of the normalized frequency detuning δ with corresponding optimal modulation of 1.27 and 3.15 respectively. (b) The line shape of the first and third Fourier coefficient c_2 and c_4 as a function of the normalized frequency detuning δ with corresponding optimal modulation of 2.84 and

4.44 respectively.

3.4 Summary

In this chapter, the general theory of SRDS and its applications for gas detection and tuning of optical pulse delay are presented. Theory of the SRD spectral signals measured using optical interferometers are developed. The mathematical descriptions of the harmonic signals with wavelength modulation is derived in detail. The dependence of the measured harmonic signals on modulation depth is calculated. Based on this calculation, optimal modulation depth is given to obtain the largest amplitude of the measured signal. This chapter offers useful theoretical understanding and guidance on SRDS optimization and modeling.

References

1. D. E. Vogler and M. W. Sigrist, "Near-infrared laser based cavity ringdown spectroscopy for applications in petrochemical industry," Appl. Phys. B Lasers Opt. **85**(2–3), 349–354 (2006).
2. T. H. Risby and S. F. Solga, "Current status of clinical breath analysis," Appl. Phys. B Lasers Opt. **85**(2–3), 421–426 (2006).
3. P. A. Martin, "Near-infrared diode laser spectroscopy in chemical process and environmental air monitoring," Chem. Soc. Rev. **31**, 201–210 (2002).
4. P. G. Westergaard, M. Lassen, and J. C. Petersen, "Differential high-resolution stimulated CW Raman spectroscopy of hydrogen in a hollow-core fiber," Opt. Express **23**(12), 1209–1215 (2015).
5. P. Martín-Mateos, J. Hayden, P. Acedo, and B. Lendl, "Heterodyne Phase-Sensitive Dispersion Spectroscopy in the Mid-Infrared with a Quantum Cascade Laser," Anal. Chem. **89**(11), 5916–5922 (2017).

6. M. Nikodem and G. Wysocki, "Molecular dispersion spectroscopy - new capabilities in laser chemical sensing," Ann. N. Y. Acad. Sci. **1260**(1), 101–111 (2012).

7. W. Ding, L. Sun, L. Yi, and X. Ming, "Dual-sideband heterodyne of dispersion spectroscopy based on phase-sensitive detection," Appl. Opt. **55**(31), 8698–8704 (2016).

8. J. B. Khurgin, R. S. Tucker, and R. S. Tucker, *Slow Light*, Optical Science and Engineering (CRC Press, 2008), **140**.

9. F. Benabid, F. Couny, J. C. Knight, and T. A. Birks, "Compact, stable and efficient all-fibre gas cells using hollow-core photonic crystal fibre," Nature **434**(March), 463–466 (2005).

10. J. L. Doménech and M. Cueto, "Sensitivity enhancement in high resolution stimulated Raman spectroscopy of gases with hollow-core photonic crystal fibers," Opt. Lett. **38**(20), 4074–4077 (2013).

11. F. Yang and W. Jin, "All-fiber hydrogen sensor based on stimulated Raman gain spectroscopy with a 1550-nm hollow-core fiber," in *Optical Fiber Sensors Conference (OFS), 2017 25th* (2017), **0**(0), p. 103233C.

12. W. Jin, Y. Cao, F. Yang, and H. L. Ho, "Ultra-sensitive all-fibre photothermal spectroscopy with large dynamic range," Nat. Commun. **6**, (2015).

13. J. Westberg, P. Kluczynski, S. Lundqvist, and O. Axner, "Analytical expression for the nth Fourier coefficient of a modulated Lorentzian dispersion lineshape function," J. Quant. Spectrosc. Radiat. Transf. **112**(9), 1443–1449 (2011).

Chapter 4: Highly sensitive hydrogen detection with stimulated Raman dispersion spectroscopy

4.1 Introduction

In chapter 3, theory of the SRDS have been presented. Optimized modulation depth has been calculated to obtain the maximum amplitudes of the harmonic signals. In this chapter, I extend the SRDS for sensitive hydrogen detection. Firstly, I measured the 2*f* signal of the SRS-induced dispersion in hydrogen-filled HC-PCF and experimentally validated the relationship between the measured harmonic signal magnitude and modulation depth presented in chapter 3 using a stabilized optical fiber Mach-Zehnder interferometer (MZI). Secondly, with the all-fiber MZI, I demonstrate a highly sensitive hydrogen detection system.

4.2 Preparation of the HC-PCF gas cell

The Raman frequency shift of $S_0(0)$ rotational Raman transition of hydrogen is ω_0 =354.36 cm^{-1} [1]. If the pump beam wavelength is near 1532nm, then probe beam at the Stokes wavelength is near 1620nm. The HC-PCF used here is NKT HC-1550-06. The fiber has a wide transmission window from 1480 to 1650 nm, which can cover both the pump and Stokes beams with low transmission loss. The transmission loss of the hollow core fiber is less than 20 dB/km from 1500 nm to 1700 nm. A ~7-m-long HC-PCF is coupled to single mode fibers (SMFs) with ceramic ferrules and sleeves to form a micro gas cell. The ends of the SMFs are 8° cleaved to minimize the Fresnel reflection shown in Fig. 4.1(a). Hydrogen molecules diffuse in and out the HC-PCF through the air gaps at the joint point. The transmission loss of the fabricated HC-PCF gas cell is evaluated by measurement of the transmitted power difference incident in and out the gas cell. Fig.

4.1(b) shows the transmission spectrum of the HC-PCF gas cell measured using Agilent 8190a, a photonic all parameter analyzer. The measured insertion loss for the pump beam (~1532 nm) is ~ 4.5 dB and for the probe beam (~1620 nm) is ~5.6 dB. Fig. 4.1(c) shows the Fourier transform result of the transmission spectrum in Fig. 4(b). The fundamental core mode (LP_{01}) and the surface mode are labeled out respectively. The coupling process is optimized with help of an optical microscope to suppress any higher order mode transmitting within HC-PCF. Over 25 dB surface mode suppression is achieved to minimize the interferometric fringes resulting from multi-modes-interferences which may deteriorate the performance of detection system.

(a)

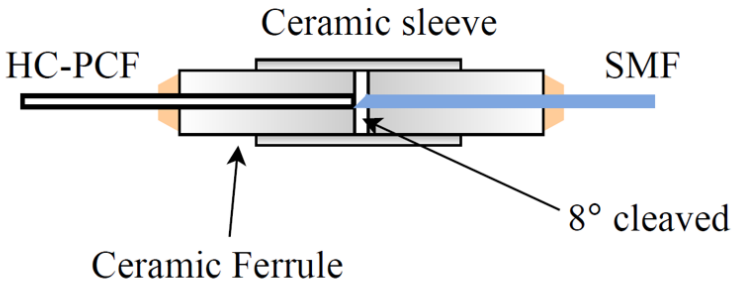

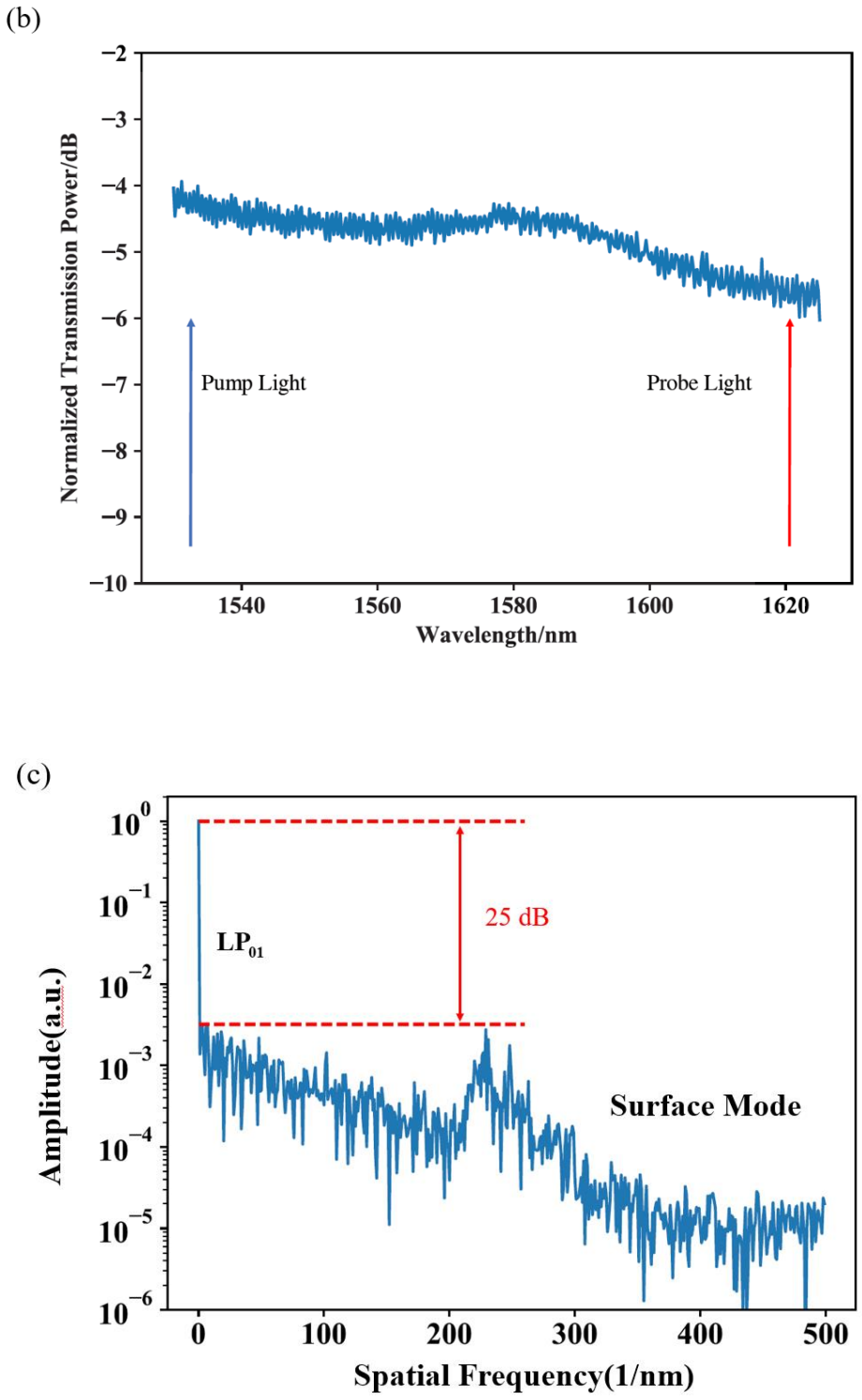

Fig. 4.1 (a) Schematic drawing of a coupling point between HC-PCF and SMF. (b) The transmission spectrum of the fabricated HC-PCF gas cell. (c) The Fourier transform of the transmission spectrum with surface mode suppression over 25 dB compared with the LP_{01} mode.

4.3 Sensitive hydrogen sensing system with SRDS in HC-PCF

4.3.1 2*f* signal measurement of the SRD

Fig. 4.2(a) illustrates the experiment setup. Hydrogen and nitrogen mixtures with different ratios are filled into the fabricated HC-PCF gas cell through the gap between SMF and HC-PCF. The Raman frequency shift of the $S_0(0)$ rotational Raman transition of hydrogen is ω_0=354.36 cm^{-1} [1]. The pump laser is a distributed feedback (DFB) semiconductor laser and its wavelength is around 1532.1 nm. An Er-doped fiber amplifier (EDFA) is used to amplify the pump power.

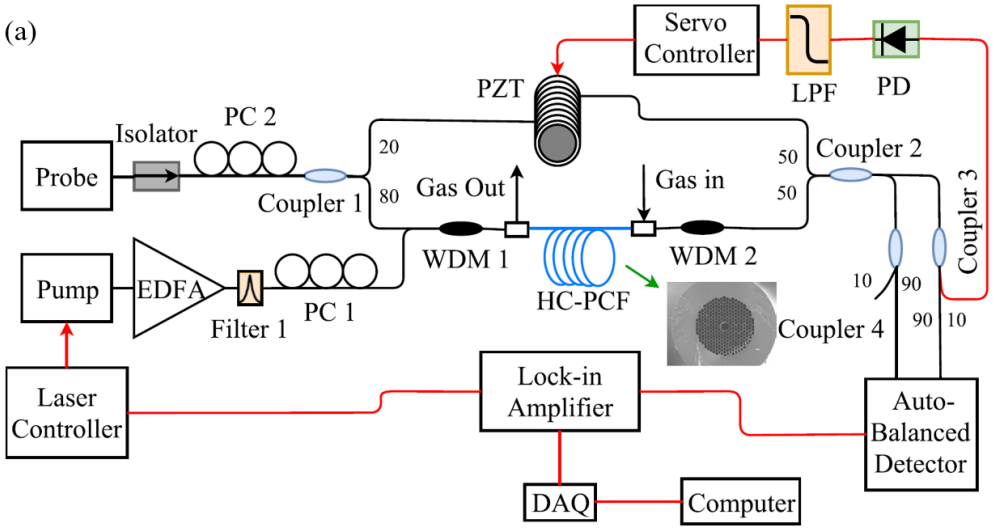

Fig. 4.2 (a) Experimental setup for laser-induced dispersion measurement. LPF: low-pass-filter; DAQ: data acquisition; PC: polarization controller; PZT: piezoelectric transducer to eliminate the phase fluctuation. Inset is the cross section image of the HC-PCF (HC-1550-06 fiber with hollow core radius of ~5.5 μm). Filter 1 is used to filter out the amplified spontaneous emission (ASE) noise of the EDFA. WDM 1&2: 1620nm/1530nm wavelength-division multiplexer.

From equation 3.1, the Raman-induced dispersion is proportional to the accumulated phase change of the probe light, which can be detected by using an optical

interferometer (e.g., a Sagnac interferometer [2] or MZI [3]) powered by a probe beam tuned near the Stokes wavelength. Here we used an all-fiber MZI to measure the Raman dispersion in hydrogen-filled HC-PCF. The MZI is powered by an external cavity diode laser (ECDL) and its wavelength fixed at ~1620 nm. To make sure the measurement of the Raman-induced dispersion has high SNR, a technique similar to the wavelength modulation spectroscopy is used [3]: the pump wavelength is sinusoidally modulated at f = 51 kHz, and it is simultaneously scanned so that the wavelength difference between the pump and probe can be tuned across the $S_0(0)$ Raman transition of hydrogen. The Raman-induced dispersion modulates the probe beam phase. The modulated phase is then converted to an intensity change by the MZI stabilized at quadrature using a servo-loop feedback [3]. The $2f$ output of the MZI is demodulated by a lock-in amplifier.

Firstly, the $2f$ component of the SRD in hydrogen-filled HC-PCF is measured when the modulation depth δ_m is changed. The measured $2f$ signal amplitude $a_2(\delta_m)$ is a function of the modulation depth δ_m shown in blue dots in Fig. 4.3. The $2f$ signal reaches its maximum amplitude at the optimal modulation depth δ_m^{opt}=2.84, giving a_2 = 0.33 [4], which agrees with the calculation given in Chapter 3 depicted in a solid line in Fig. 4.3.

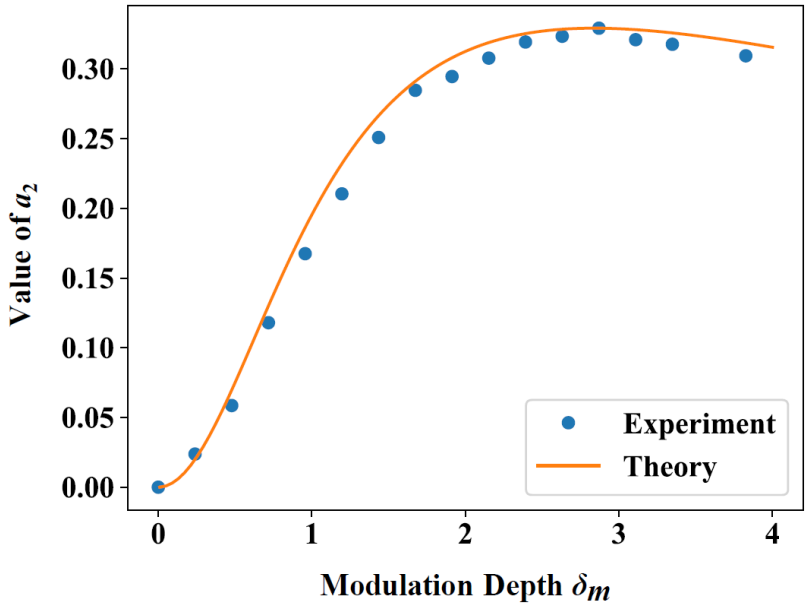

Fig. 4.3 The measured 2*f* signal amplitude of MZI output as a function of modulation depth. Blue dots are experiment results and the solid line is calculation based on formulas in Chapter 3.

Fig. 4.4(a) shows the measured 2*f* signal for pure hydrogen when 3.5 bar hydrogen is filled inside the hollow core with a pump power of ~100 mW delivered to the HC-PCF. The corresponding peak pump intensity is estimated to be 0.314 MW/cm^2 at the center of the hollow core. The numerically calculated 2*f* signal based on the formulations developed in Chapter 3 is compared with the measured 2*f* signal shown in Fig. 4.4 (b), and the measurement agrees well with the calculation.

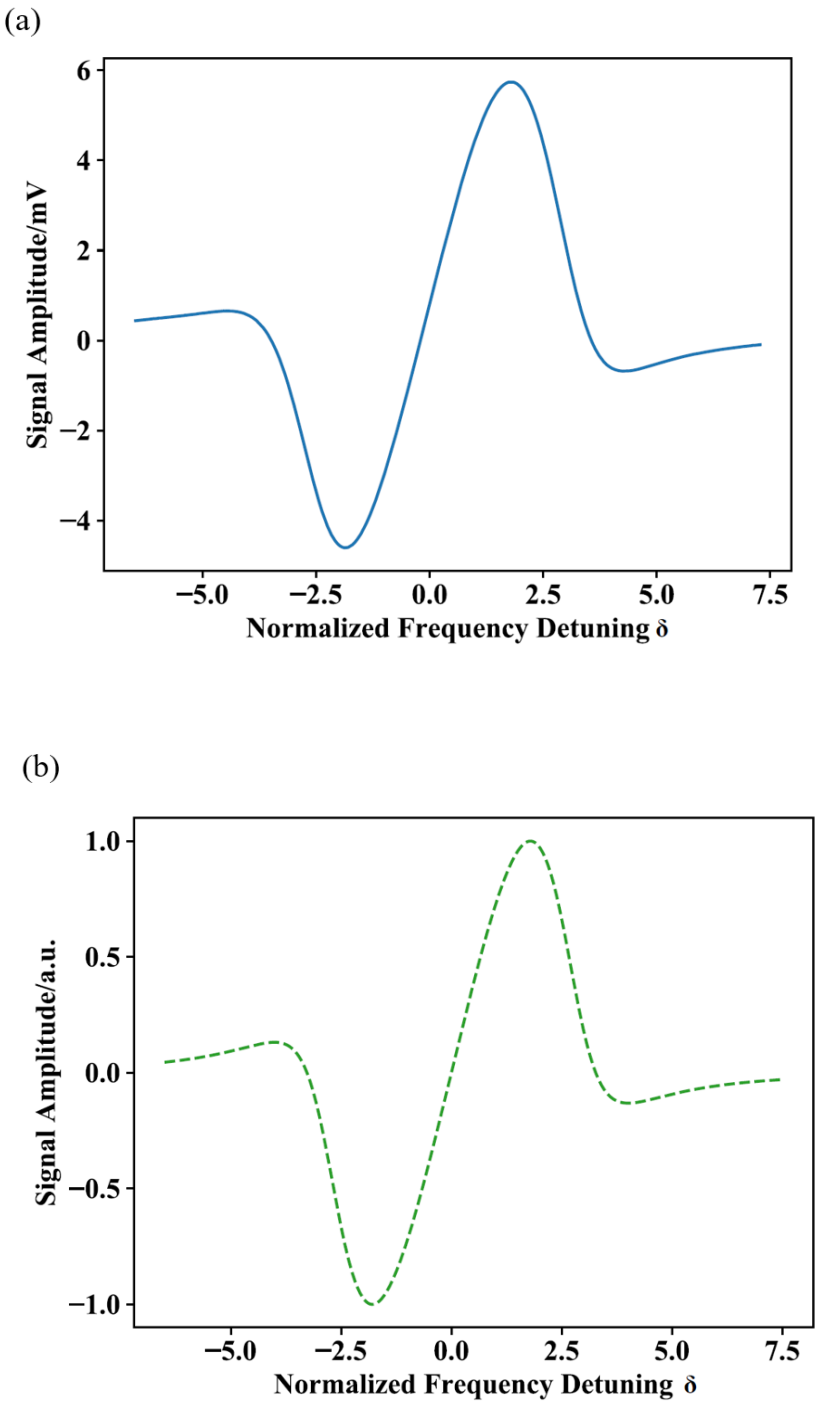

Fig. 4.4 (a) Measured and (b), calculated 2*f* signal due to laser-induced dispersion near the $S_0(0)$ transition of hydrogen. Pure hydrogen is filled into the HC-PCF with a pressure of 3.5 bar. The modulation depth is set to be 2.84.

The Raman-induced dispersion can be tuned in a linear way by changing gas

concentration. Fig. 4.5(a) depicts the detected 2*f* signal around the Raman transition with pump power of ~100 mW in HC-PCF for different hydrogen concentration of 4, 20 and 100% at 3.5 bar. Peak-to-peak amplitude of the 2*f* signal has a linear relationship with gas concentration as depicted in Fig. 4.5(b). The magnitude of dispersion change can also be changed by adjusting pump laser power. The measured 2*f* signal for a 20% hydrogen balanced in nitrogen with four different pump power levels is depicted in Fig. 4.5(c). Fig. 4.5(d) shows that the measured 2*f* signal is linearly proportional to the pump power, agreeing with the prediction from Chapter 3. Such an SRS-induced dispersion can be useful for a range of applications such as precision gas spectroscopy and optical pulse walk-off cancellation [5].

(a)

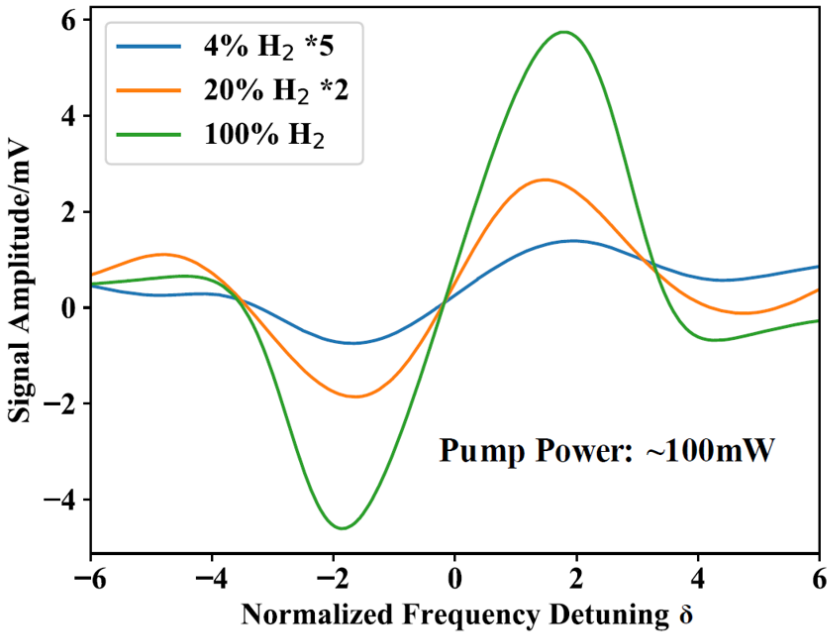

(b)

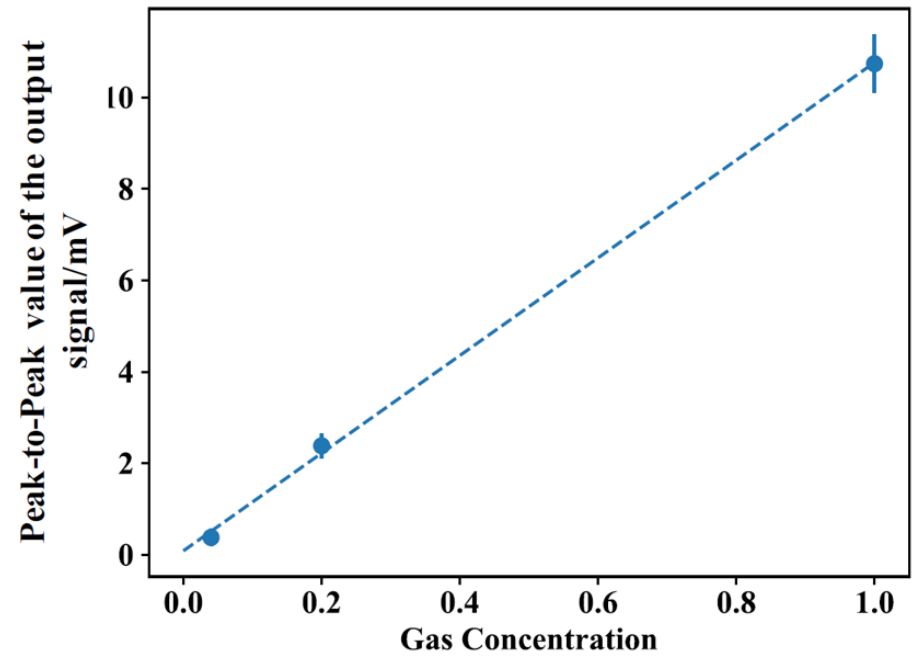
Peak-to-Peak value of the output signal/mV
0
2
4
6
8
10
0.0
0.2
0.4
0.6
0.8
1.0
Gas Concentration

(c)

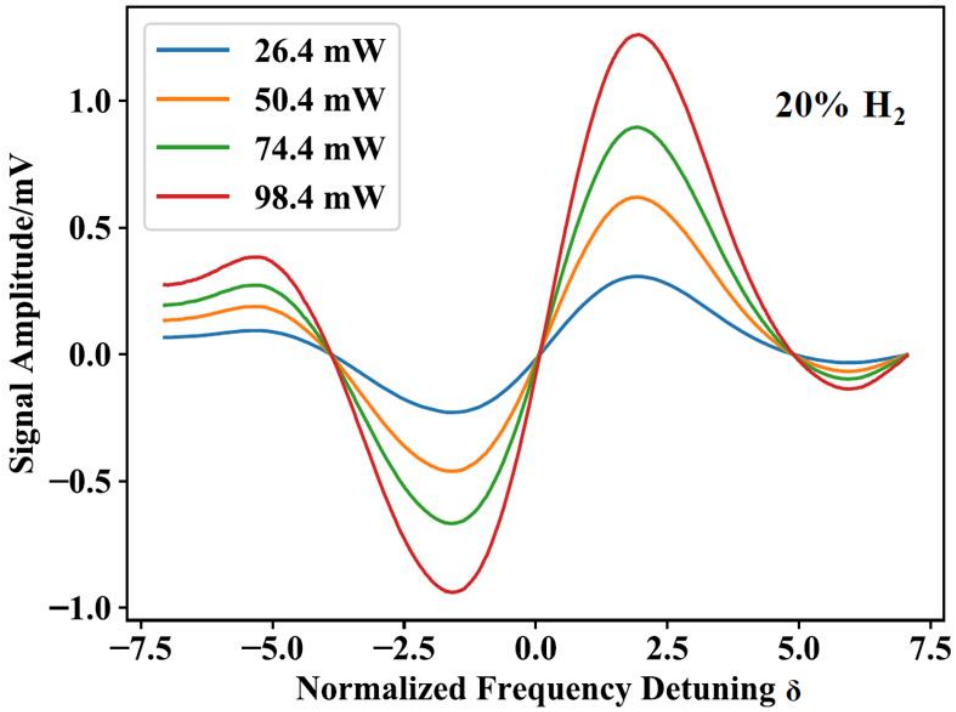
26.4 mW
50.4 mW
74.4 mW
98.4 mW
20% H2
Signal Amplitude/mV
1.0
0.5
0.0
−0.5
−1.0
−7.5
−5.0
−2.5
0.0
2.5
5.0
7.5
Normalized Frequency Detuning δ

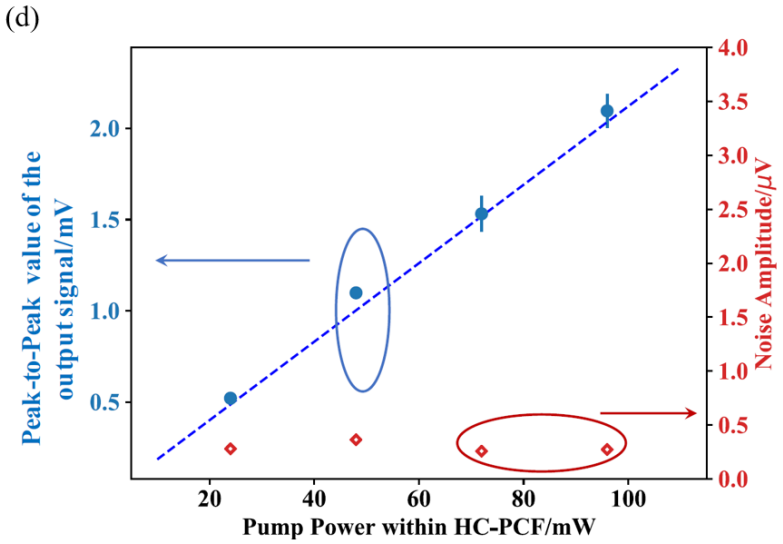

Fig. 4.5 The measured results of actively tuning Raman-induced dispersion in HC-PCF. (a) and (b) are the results of adjusting SRS-induced dispersion by changing hydrogen concentration. (a) Measured 2*f* output signals when pump beam is scanned across the $S_0(0)$ Raman transition of hydrogen of different concentration. The 2*f* output signals for 4% and 20% hydrogen are scaled up 5 and 2 times respectively for better presentation; (b) The peak-to-peak value of 2*f* output signal as function of gas concentration. Error bars show the standard deviation from 10 measurements and their magnitudes are scaled up 10 times for better clarity. (c) and (d) are results of controlling SRS-induced dispersion by changing pump power with 20% hydrogen; (c) The 2*f* output signal when pump wavelength is tuned across Raman transition line with different power levels and 20% hydrogen; (d) Peak-to-peak value of 2*f* output signal for 20% hydrogen and the standard deviation of noise as functions of pump power levels. Error bars show the standard deviation from 10 measurements.

4.3.2 Noise performance of the detection system

To furtherly extend the technique for high sensitivity hydrogen detection, we evaluated the system noise performance by tuning the pump wavelength away from the Raman resonance and fix the wavelength at 1531.956 nm. The standard deviation of noise for

different pump power levels in HC-PCF is shown in Fig. 4.5 (d) in red diamonds. For a pump power of～98.4 mW, the peak-to-peak 2*f* output signal for 20% hydrogen is ~2.2 mV and the standard deviation of noise is 0.273 μV with 1s lock-in time constant, corresponding to a detection bandwidth of 0.094 Hz. This gives an SNR of 8059. The detection limit in terms of noise equivalent concentration (NEC) for an SNR of unity is then estimated to be 25 ppm or a normalized NEC (NNEC) of ~17.4 ppm/(m·W). The dynamic range of the system is estimated to be more than 4 orders of magnitude from the minimum detection level to 100% hydrogen. The largest phase modulation for 100% hydrogen is estimated to be ~10^{-3} rad, well within the linear region around the quadrature point of the MZI. From Fig. 4.5(d), the 2*f* signal increases approximately linearly with the pump power while the noise level remained relatively unchanged, indicating further improvement of detection limit is possible by simply increasing the pump power level.

One of the most intuitive limiting factors of detection limit is the performance of the MZI system. The fiber MZI system used here is inherently sensitive to environmental fluctuation (e.g. acoustics and vibrations) and hence it will affect the system performance. In this experiment, the environmental disturbance is in time suppressed by a PZT phase compensator. The working point drift of MZI system may be determined by comparing the amplitude fluctuation of the output signal of a stabilized MZI with the interference fringes contrast of MZI without stabilization (i.e., the amplitude of the output signal periodically change from -1V to 1 V corresponding to the phase change of π). The standard deviation of the working point drift is measured to be 0.0432° depicted in Figure 4.6(a). The working point drift induced measurement error is defined by $\Delta C/C = 1 - \cos(0.0432°) = 2.84\times10^{-7}$. In the test of detection limit, for 20% hydrogen, the drift induced gas concentration uncertainty is 56.8 ppb, which is much lower than the system detection limit and hence the stability of the MZI working point has little impact

on the detection limit.

However, the PZT servo-based phase compensator may introduce unwanted noise over a wide frequency range and these noise components may be large compared with the modulated phase signal shown in Figure 4.6 (b), which is measured by the electrical signal analyzer (ESA). Once the PZT is powered on, high frequency noise components emerge which is believed to be the contribution of electric noise. Those noise components fall into the detection band can not be separated from the SRD signal. Much effort has been made to optimize the voltage applied on the PZT and minimized the electric noise impact. To minimize the detection noise, we first analyze the noise spectrum of the interferometer output. Besides the detected harmonic signals at 51 kHz and 102 kHz, a strong mechanical interference is also observed, which may affect the detection performance. To suppress the mechanical interference, notch filters are adopted. By applying notch filters, 10 dB reduction of the noise floor is observed shown in Figure 4.6 (b).

(a)

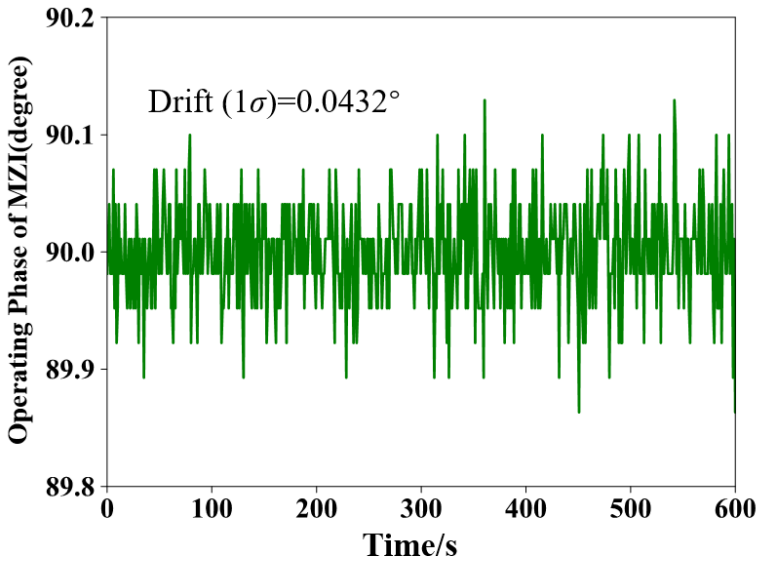

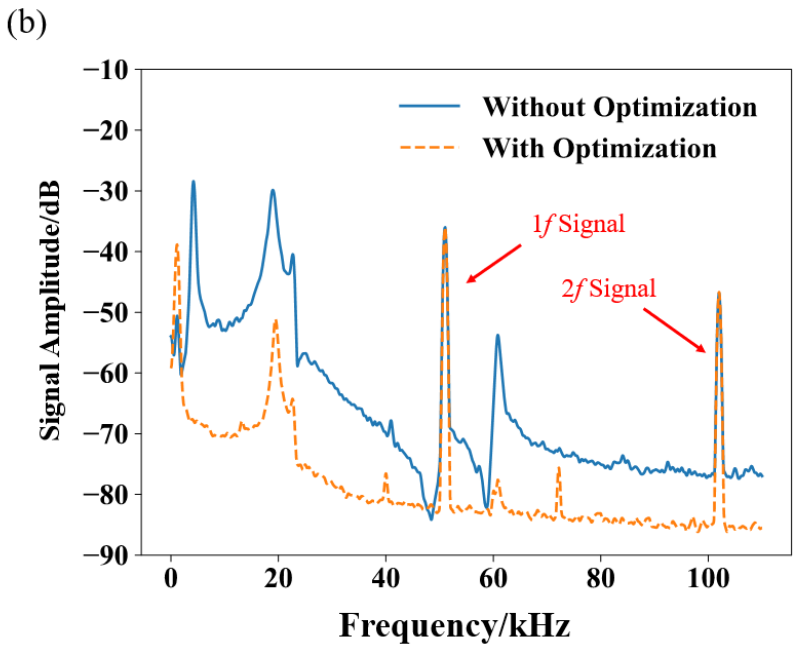

Fig. 4.6 (a) Output phase fluctuation of the stabilized MZI at its quadrature point. (b) The signal spectrum of the MZI output as the pump light is wavelength modulated around $S_0(0)$ Raman transition of hydrogen. The noise floor induced by PZT is significantly suppressed by 9 dB with an optimized voltage applied on the PZT.

4.4 Discussions

In this chapter, experiments were conducted at room temperature in a lab environment, and no notable influence of temperature on the measured SRS induced dispersion (i.e., dispersion line-shape and magnitude) was observed. However, Raman resonances (i.e., amplitude, resonance frequency and linewidth) are temperature dependent and would affect the characteristics of Raman dispersion when temperature variation becomes large [6], [7]. A full investigation of the effect of temperature on Raman dispersion in gas-filled HC-PCFs should be conducted, particularly for high temperature applications.

In our experiments, gas is filled into the HC-PCF through gaps between the HC-PCF and

SMF. It took long time (i.e., 1-2 hours) to achieve a uniform distribution of concentration and pressure along the 7-m-long HC-PCF, which is not suitable for practical applications. A faster response may be realized by drilling multiple micro-channels along the sensing HC-PCF by using femtosecond laser. With multiple micro-channels along a 2.3-m-long HC-PCF, gas diffusion process as short as ~40s at atmospheric condition has been demonstrated [8].

For the current system, the limiting factor of the performance of gas detection in terms of NNEC is the instability of the MZI perturbated by environmental noise and mode interference noise of the HC-PCF, since the HC-PCF can support multiple guiding modes. Better vibration isolation and high-order mode suppression in the HC-PCF may be employed to reduce the system noise level. Other noise sources such as laser fluctuation and the instability of laser sources may also need to be addressed in our future work. The minimum detectable phase change at shot-noise limited system performance is estimated as[9]:

$$\Delta\phi_{\min} = \sqrt{\frac{2h\nu_{probe}B}{\eta P_{probe}}}, \tag{4.1}$$

where h is the Planck constant, ν_{probe} is probe light frequency. B is detection bandwidth. η is photodetector efficiency and P_{probe} is probe light power received by photodetector. We consider probe light (~1620 nm) power received by photodetector is 120 μW, the detection bandwidth is 0.094 Hz and the photodetector efficiency is 0.765, then the minimum detectable phase change would be ~1×10^{-8} rad. In this experiment, 100% hydrogen with 7m-long HC-PCF is pumped by 100 mW pump light. the shot-noise limited NEC is 4 ppm, despite the deterioration of SNR by factor of 4 caused by wavelength modulation and 2f signal detection scheme[10]. The lowest detection limit of this experiment is ~7 times worse than shot-noise limited performance. Hence, it is

possible to further improve the sensitivity of measurement by further suppression system noise level, using higher pump power and longer HC-PCF.

By using hollow-core fiber with a broadband transmission window, multi-gas detection may be performed. A straightforward configuration for multiple gases detection may be to use a fixed probe laser and a wavelength-tunable pump laser copropagating in the hollow-core fiber. The pump wavelength is continuously scanned so that the frequency difference between the probe and the pump can be tuned across multiple Raman transitions. With a fixed probe laser, the optical interferometer for phase detection can be fully stabilized, and the system noise can be minimized. Fig. 4.7 shows the calculated pump wavelengths and the magnitude of the rotational Raman process for oxygen, nitrogen and carbon dioxide, assuming that the probe wavelength is fixed to 1550 nm [11]–[13]. A tunable pump laser with wavelength from 1530 to 1550 nm would allow the detection of the multiple Raman lines of these gases.

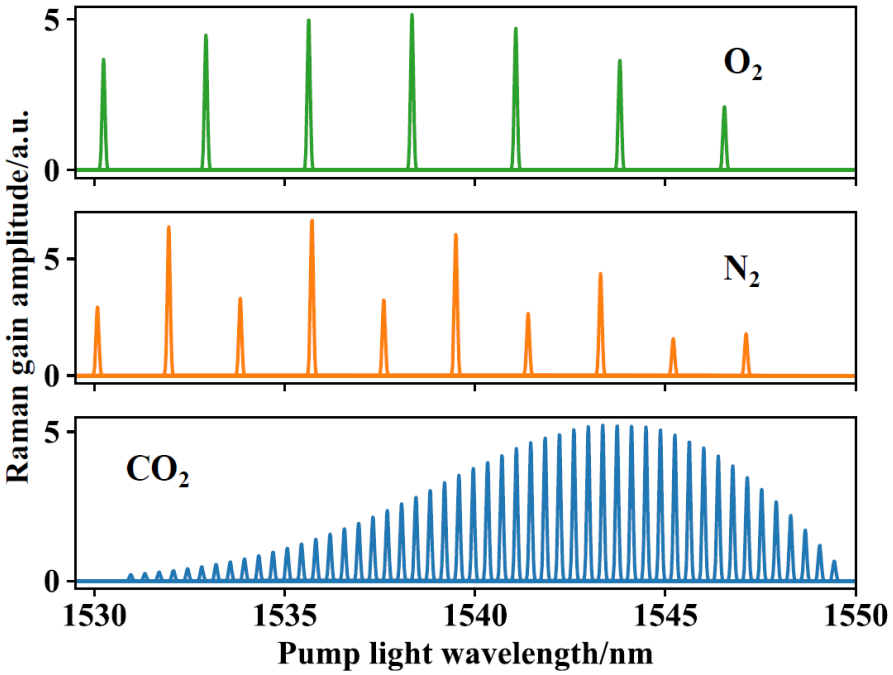

Fig. 4.7 Calculated rotational Raman transitions of oxygen, nitrogen and carbon dioxide.

4.5 Summary

In this chapter, a stabilized all-fiber MZI is implemented to measure the Raman-induced dispersion of hydrogen in 7m-long HC-PCF. The 2*f* signal of the Raman-induced dispersion is measured, and its amplitude as a function of the modulation depth is experimentally verified. The detection system is extended for sensitive hydrogen detection and has achieved a normalized noise-equivalent concentration of 17.4 ppm/(m·W) at 3.5 bar and a dynamic range over 4 orders of magnitude. The noise performance and the limiting factors of the detection system are discussed. With the development of hollow-core fibers with lower loss, broader transmission window and better mode quality [14], multi-gases detection using SRDS is achievable.

References

1 R. G. Wenzel, “Stimulated Rotational Raman Scattering in CO2-Pumped Para-H2,” *IEEE J. Quantum Electron.*, vol. QE-19, no. 9, pp. 1407–1413, 1983.

2 Y. Lin *et al.*, “Pulsed photothermal interferometry for spectroscopic gas detection with hollow-core optical fibre,” *Sci. Rep.*, vol. 6, no. 1, p. 39410, Dec. 2016.

3 W. Jin, Y. Cao, F. Yang, and H. L. Ho, “Ultra-sensitive all-fibre photothermal spectroscopy with large dynamic range,” *Nat. Commun.*, vol. 6, 2015.

4 J. Westberg, P. Kluczynski, S. Lundqvist, and O. Axner, “Analytical expression for the nth Fourier coefficient of a modulated Lorentzian dispersion lineshape function,” *J. Quant. Spectrosc. Radiat. Transf.*, vol. 112, no. 9, pp. 1443–1449, 2011.

5 G. Fanjoux and T. Sylvestre, “Cancellation of Raman pulse walk-off by slow light,” *Opt. Lett.*, vol. 33, no. 21, pp. 2506–2508, 2008.

6 M. Rokni and A. Flusberg, “Stimulated Rotational Raman Scattering in the Atmosphere,” *IEEE J. Quantum Electron.*, vol. 22, no. 7, pp. 1102–1108, 1986.

7 B. W. K. Herring G C, Dyer M J, “Temperature and density dependence of the linewidths and line shifts of the rotational Raman lines in N2 and H2,” *Phys. Rev. A*, vol. 34, no. 3, p. 1944, 1986.

8 F. Yang, W. Jin, Y. Lin, C. Wang, H. Lut, and Y. Tan, “Hollow-core microstructured optical fiber gas sensors,” *J. Light. Technol.*, vol. 35, no. 16, pp. 3413–3424, 2017.

9 D. L. Mazzoni and C. C. Davis, “Trace detection of hydrazines by optical homodyne interferometry.,” *Appl. Opt.*, vol. 30, no. 7, pp. 756–64, 1991.

10 J. Ye, L.-S. Ma, and J. L. Hall, “Ultrasensitive detections in atomic and molecular physics: demonstration in molecular overtone spectroscopy,” *J. Opt. Soc. Am. B*, vol. 15, no. 1, p. 6, 1998.

11 L. C. Hoskins, “Pure rotational Raman spectroscopy of diatomic molecules,” *J. Chem. Educ.*, vol. 52, no. 9, p. 568, 1975.

12 H. Finsterholzl, J. G. Hochenbleicher, and G. Strey, “Intensity Distribution in Pure Rotational Raman-Spectra of Linear-Molecules in Ground and Vibrational 2 States Application To Acetylene,” *J. Raman Spectrosc.*, vol. 6, no. 1, pp. 13–19, 1977.

13 B. L. M. Klarenaar, F. Brehmer, S. Welzel, H. J. van der Meiden, M. C. M. van de Sanden, and R. Engeln, “Note: Rotational Raman scattering on CO_2 plasma using a volume Bragg grating as a notch filter,” *Rev. Sci. Instrum.*, vol. 86, no. 4, p. 046106, 2015.

14 S. Gao *et al.*, “Hollow-core conjoined-tube negative-curvature fibre with ultralow loss,” *Nat. Commun.*, vol. 9, no. 1, p. 2828, 2018.

Chapter 5: Toward practical hydrogen sensors with Stimulated Raman Dispersion Spectroscopy

5.1 Introduction

In Chapter 4, Stimulated Raman dispersion spectroscopy has been applied for hydrogen detection with high sensitivity and good selectivity[1]. A pump-probe configuration is typically used to generate and detect the stimulated Raman dispersion when the frequency difference between the pump and probe beams matches Raman transition of the hydrogen molecules. An optical interferometer powered by the probe beam is used to measure the probe beam phase modulation resulted from SRD. With an MZI configuration, short-term noise-equivalent hydrogen concentration down to ppm level has been demonstrated 7 meters of HC-PCFs. However, the operation point of the MZI is not stable over a longer term (e.g., an hour) even with a servo-control loop, making the system difficult for practical gas detection. And using meters long HC-PCF makes it hard to reduce the time of filling gas.

A low-finesse FPI can be formed by natural reflections at the joints between HC-HCF and single mode fibers (SMFs), as illustrated in Fig. 1. The Raman-induced dispersion is detected by the low-finesse FPI operating by the probe beam near the Stokes wavelength. The FPI detection scheme enables very compact sensing configuration as well as better immunity against environmental perturbation since the SMFs are merely used for light transmission and do not act as part of the interferometer. Low frequency external perturbation on the SMF has minimal effect on the phase detection since the reflected probe beams pass through the SMF almost at the same time (e.g., the time difference is less than 1 ns for 15 cm long sensing HC-PCF) and hence the two beams basically experience the same perturbation and hence the differential difference is insensitive to

the perturbation. And the short length of HC-PCF makes it possible to realize fast response time.

In this chapter, I present a hollow-core fiber FPI hydrogen sensor based on stimulated Raman dispersion spectroscopy with simple, compact size, faster response time, good long-term stability and the potential for practical applications.

5.2 Basics of FPI for hydrogen detection

5.2.1 Theory of a hollow-core FPI

A miniature hollow-core FPI is proposed in Fig. 5.1 for fast hydrogen detection. The FPI consist of a section of HC-PCF attached by two flat fiber end faces of two SMF pigtails, which forms a low finesse fiber Fabry-Perot cavity. The length of the FPI is typically several centimeters. Too short cavity length (<0.5 cm) leads to small signal magnitude and limits the sensitivity of the hydrogen sensor. Too long cavity length (>20 cm) causes narrow free space rage (FSR) of the FPI and mode interference (MI) fringes. Such interferometric fringes induce extra interference of the detected signal and hence reduce the SNR of the sensing system.

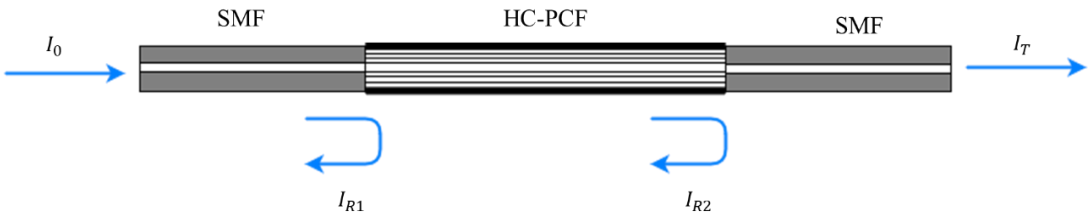

Fig. 5.1 Schematic of the proposed FPI with HC-PCF fiber.

The two flat end faces of the SMF and HC-PCF/SMF joints form a low finesse FPI shown in Fig. 5.1. Ideally, the coupling loss of each HC-PCF/SMF joint is neglected and the reflectivity of the two end faces of SMFs are considered to be equal to R ($\ll 1$), the reflected and transmitted light intensity out of the FPI may be as:

$$I_R = I_0 R[1+\exp(G)+2\exp(G/2)\cos\phi] \tag{5.1}$$

$$I_T = I_0 \exp(G) - 2I_0 R\exp(G/2)\cos\phi \tag{5.2}$$

with

$$\phi = 4\pi n_{eff} L/\lambda_{probe} + \phi_0 \tag{5.3}$$

where I_0, I_R and I_T are the incident probe light, the reflected light and the transmitted light intensity, respectively; G is the Raman gain of the probe light near Stokes wavelength; ϕ is the accumulated phase change experienced by the probe light; n_{eff} is the effective RI of the gas medium; L is the length of the FPI, λ_{probe} is the probe light wavelength and ϕ_0 is a constant phase bias. In equation 5.2, the higher power of R is ignored. Backward Raman scattering is not considered here for its weak effect compared with forward Raman scattering[2]. The minus before the second term of equation 5.2 is due to reflection phase change, indicating a phase shift of π between the reflected and the transmitted spectrums. When the frequency difference between the probe beam and a wavelength modulated pump beam matches a Raman transition of hydrogen molecules, ϕ is modulated as :

$$\phi = \phi_{DC} + \phi(t) \tag{5.4}$$

where ϕ_{DC} is the DC phase shift component and $\phi(t)$ is the Raman-induced phase modulation component, which is proportional to the hydrogen concentration. With properly selected the probe length wavelength, the FPI can be operated at quadrature point (i.e. $\phi_{DC} = (m+0.5)\pi$, where m is an integer).

5.2.2 Fabrication of a hollow-core FPI

The FPI shown in Fig. 5.1(a) is implemented by butt coupling one end with ceramic sleeve and ferrules depicted in Fig. 5.2 (a) and fixed with ultraviolet (UV) curing glue.

Both end faces of HC-PCF and SMF are cleaved to be flat. Gas may enter the FPI through a micro gap between HC-PCF and SMF by diffusion. As it is shown in Fig. 5.2(c), with help of the microscope, a micro-channel with 1 μm width is left to allow gas molecules to diffuse into the hollow core fiber. The other end is joined by fusion one cleaved SMF end face with the cleaved HC-PCF. To fully exploit the advantages of HC-PCF, it is essential to join the SMF with HC-PCF with minimum coupling loss. However, due to the micro-hole structure, it is still challenging to splice HC-PCF to SMF. In this section, I will demonstrate a low-loss splicing method to join HC-PCF with SMF. The micro-hole collapse of HC-PCF during fusion process is the main factor that contributes to coupling loss. An effective method to avoid the collapse is to use low splicing current and shorten the fusion time. However, there is a tradeoff between the coupling loss and the mechanical strength of the joint point since lower splicing current causes lower coupling loss and weaker mechanical strength. Besides splicing current, the overlap distance should be considered. For butt coupling, HC-PCF and SMF merely touch each other. However, for splicing process, two fibers needed to be pushed further since they are softened by the discharge current. When using weaker fusion current, both fiber tips will not be softened enough, a suitable overlap distance needs to be applied to avoid misalignment resulting from large overlap distance.

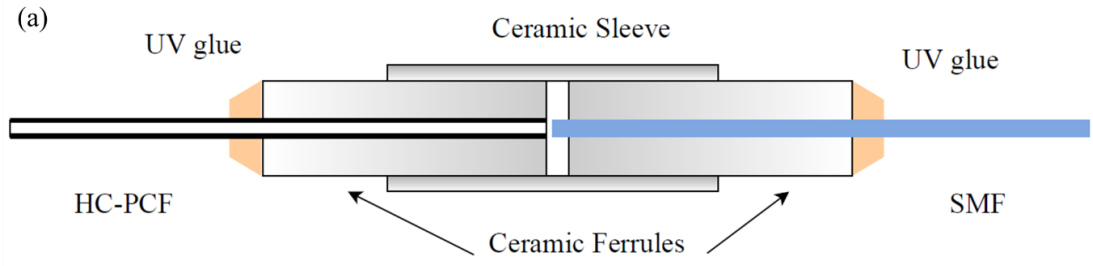

(b)

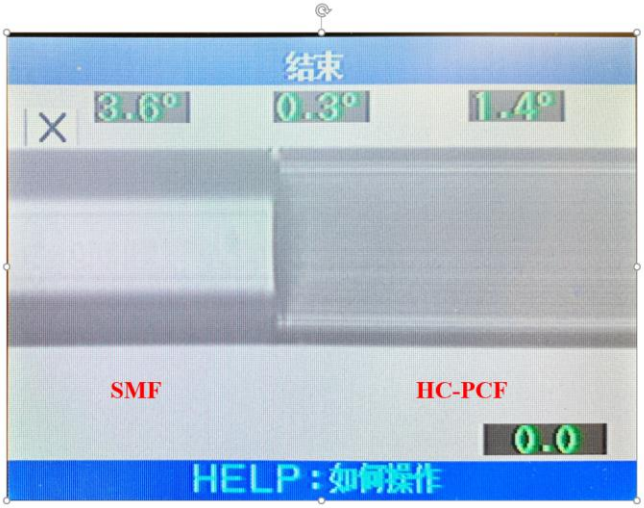

(c)

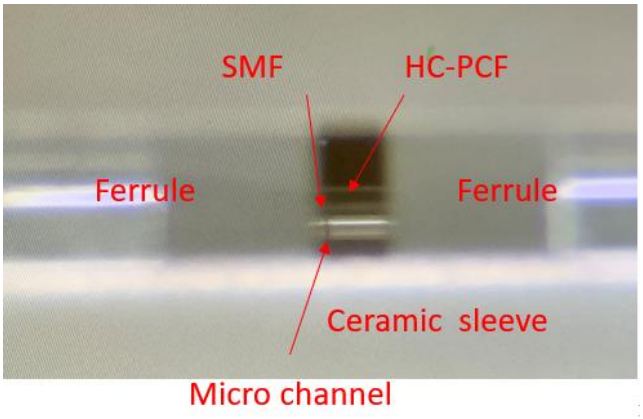

Fig. 5.2 (a) Butt coupling of HC-PCF with SMF using ceramic sleeve and ceramic ferrules. (b) The screenshot of the fiber fusion splicer after the fusion process of the SMF and HC-PCF. The coupling loss of the splicing point is estimated to be 2dB. (c) The picture of the joint point of the hollow core fiber and single mode fiber with a 1 μm wide micro-channel.

Based on the general principles introduced above, I experimentally demonstrated the low-coupling-loss splicing of SMF and HC-PCF (HC-1550-06, from NKT Photonics). The mode field diameters of HC-1550-06 and SMF are similar, which allows low-loss coupling. It is found that the HC-PCF is more readily to achieve the softening point than SMF. To obtain good mechanical strength of the splicing point, the overlap distance is

set to be 10 μm. The collapse of the micro-holes of HC-PCF is sensitive to the fusion current. When the fusion current is set low, e.g., 9 mA with fixed fusion time of 0.3 s, most micro-holes remain unaffected by the heated discharge. Slightly increase the fusion current from 9 mA to 11 mA, the micro-holes gradually collapse from inner circles to outer circles corresponding to the thermal distribution induced by fusion current. The coupling loss is determined to increase as the micro-holes collapse[3]. The optical microscopy image of the spliced joint of HC-PCF and SMF is given in Fig. 5.2(b). The coupling loss of the splicing joint is estimated to be 2 dB.

5.3 Evaluation of the hollow-core FPI performance

5.3.1 Measurement of the FPI spectrum

To evaluate the performance of the hollow core FPI, the reflected and transmitted spectrum of the FPI is measured using the experimental setup depicted in Fig. 5.3. Light emitted from a broadband source is launched into the "1" port of the circulator and reflected by the FPI via the "2" port. The reflected light is received by an optical spectrum analyzer (OSA) through port "3". The transmitted spectrum is recorded by connecting the output SMF pigtail of the FPI to the OSA.

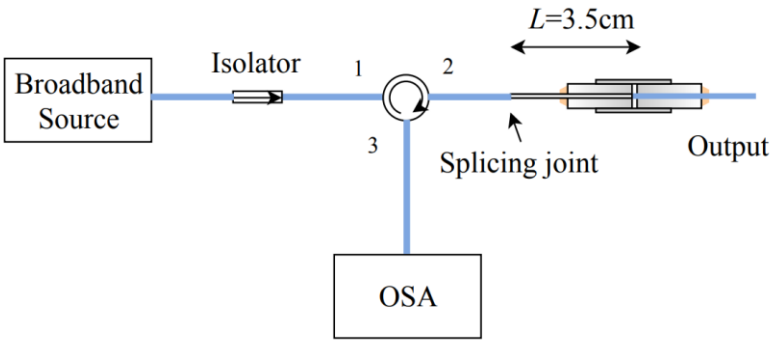

Fig. 5.3 Experimental setup for measurement of the reflected and transmitted spectrum of FPI.

The measured spectrums are shown in Fig. 5.4 with the wavelength resolution and step are set to be 10 pm and 1 pm respectively. Based on the measured reflected spectrum, the FSR of the FPI is nearly 38 pm. Given the relationship between the cavity length L and the measured FSR:

$$L = \lambda_{probe}^2 / (2FSR) \tag{5.5}$$

With the probe light wavelength $\lambda_{probe} \approx 1620$ nm and FSR=38 pm, the cavity length L is estimated to be 3.5 cm.

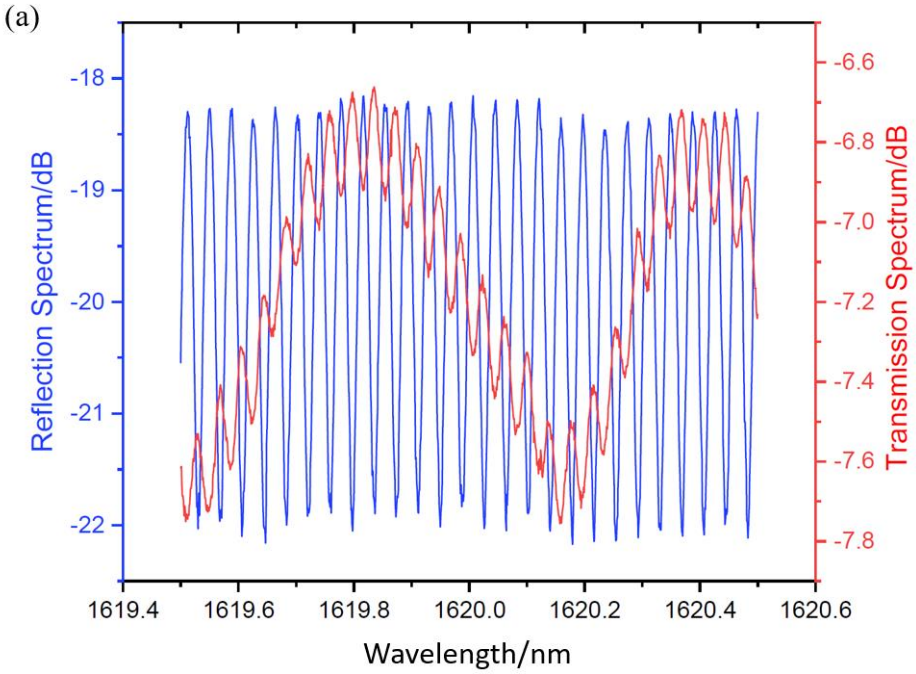

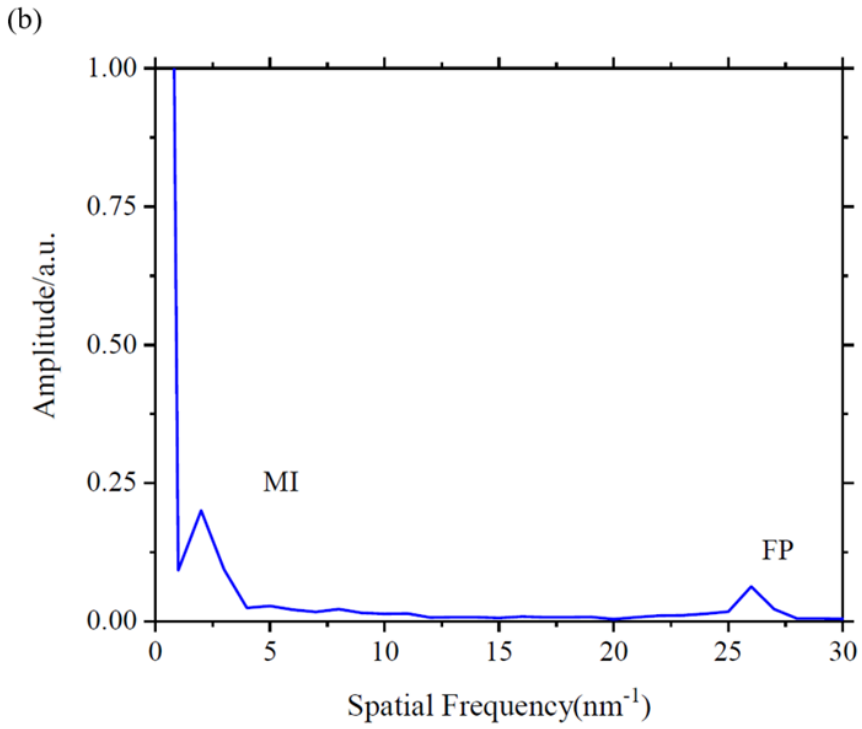

Fig. 5.4 (a) The measured reflected and transmitted spectrums of a 3.5 cm long FPI. (b) The Fourier transform of the FPI transmitted spectrum.

The measured transmitted spectrum (red line) in Fig. 5.4 is π phase shifted compared with the reflected spectrum (blue line). Due to the coupling loss, the two transmitted light beams which experience higher coupling loss of the FPI, induce an interference pattern with much smaller visibility compared with the reflected spectrum. A periodic fringe with an FSR of 0.65 nm is superimposed on the FPI transmitted interference spectrum. The fast Fourier transform (FFT) of the FPI transmitted spectrum is shown in Fig. 5.4(b) with two interference peaks. One peak at the spatial frequency of 2/nm is identified as the interference between the fundamental core mode and the cladding modes of HC-CF with effective RI difference of 0.075[4]. Another peak at spatial frequency of 26/nm is identified as the FP interference.

5.3.2 Stabilization of the FPI

For practical applications, the cavity length variation of a hollow-core fiber based FPI which is sensitive to environmental perturbations, i.e., vibrations and temperature variations, which induces fluctuations of the detected phase signal. The phase fluctuation would significantly limit the NEC of the sensing system. In this section, a piezo-mechanically actuated hollow-core fiber based FPI with feedback servo loop is introduced to eliminate the environment influence on the detected signal. The cavity length is locked to a stable probe laser so that λ_{probe} is fixed at the quadrature point of the FPI. As it is shown in Fig. 5.5(a), the FPI is mounted on a PZT (P-888.91, Physik Instrumente) with two fixing points on the HC-PCF using UV glue. The experimental setup shown in Fig. 5.5(b) is used to lock the FPI cavity length to a stable ECDL.

(a)

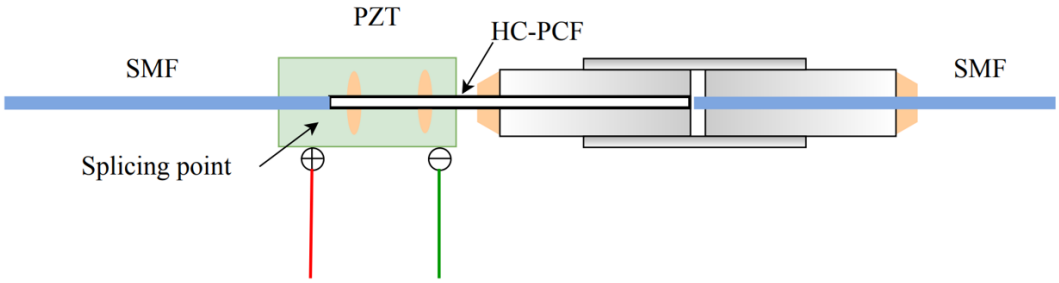

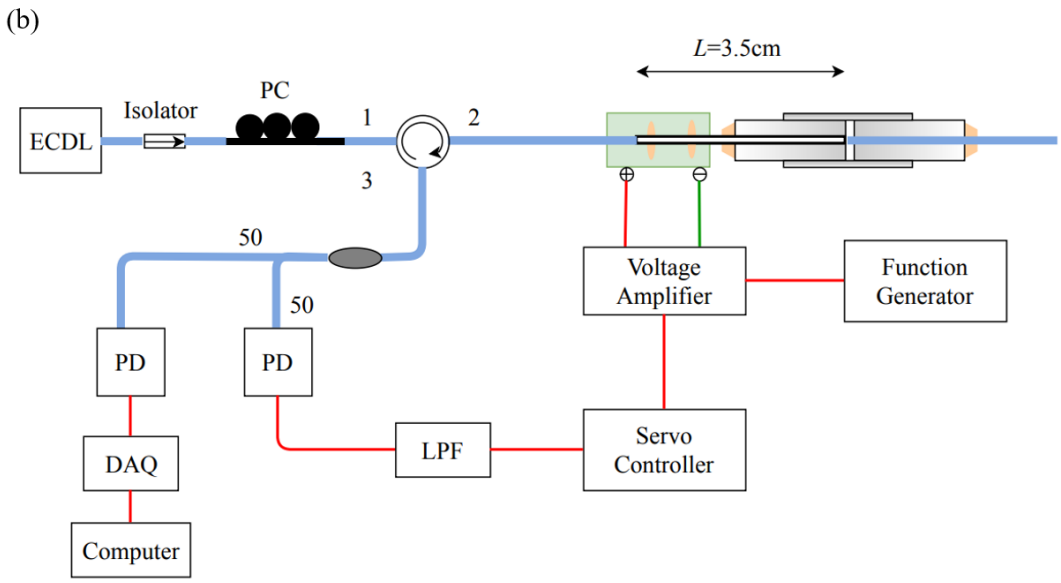

Fig. 5.5 (a) Diagram of the hollow-core based FPI mounted on a PZT. (b) Experimental setup to lock the FPI cavity length to the ECDL. The cutoff frequency of the LPF is set to be 320Hz.

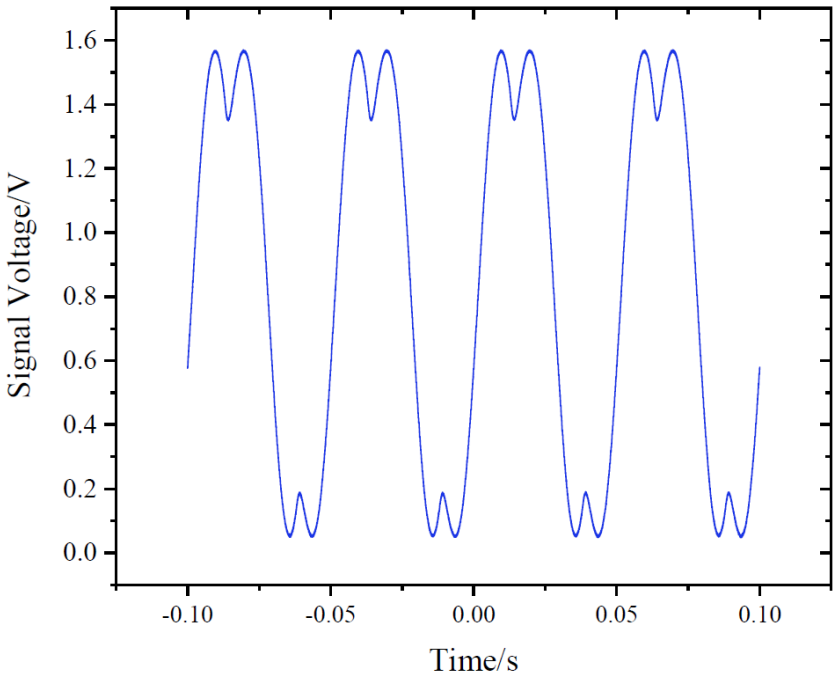

Fig. 5.6 The monitored signal with a triangular wave voltage (amplitude of 1V and frequency of 20 Hz) applied on the PZT to actively stretch the FPI cavity length.

Light from ECDL is launched into the FPI. The reflected light via optical circulator is split into two beams. One is used to monitor the detected light intensity fluctuation caused by cavity length variation. The other beam is detected by a PD and filtered by a lowpass filter. The filtered signal is sent into a servo controller to stabilize the PTI length. A function generator is used to generate phase change by applying a triangular wave voltage with an amplitude of 1V and frequency of 20Hz on a PZT to linearly stretch the FPI cavity length. The monitored light intensity signal is given in Fig. 5.6. Gradually decreasing the amplitude of the applied triangular wave and tuning the DC voltage bias to ensure λ_{probe} is near the quadrature point of the FPI. Then turn on the servo controller to actively stretch the cavity length and furtherly decrease the amplitude of the triangular wave until it is 0. The environmental perturbations are eliminated and stable output of the FPI is detected which is shown in Fig. 5.7. At this moment, even if the triangular wave is applied on the PZT with larger amplitude (e.g., 3V), no fluctuation of the monitored light intensity is observed.

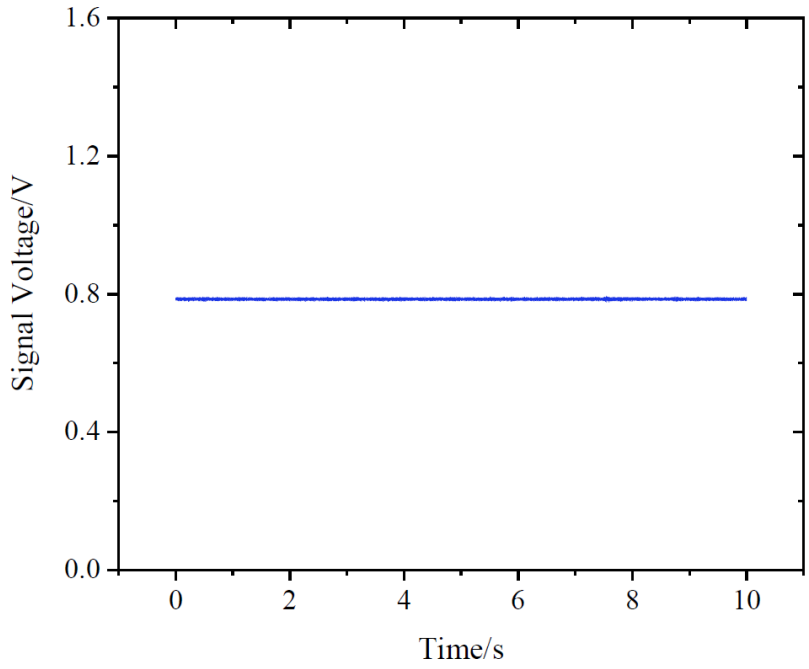

Fig. 5.7 The monitored signal when the servo controller is activated and the FPI cavity length is locked to a stable ECDL.

The stability of the locked FPI cavity in terms of phase variations can be evaluated by comparing the fluctuations of the monitored signal with the signal amplitude shown in Fig. 5.6. The phase variation of the stabilized FPI output is shown in Fig. 5.8. The standard deviation of the detected phase fluctuation is about 0.13°. Such phase fluctuations can be converted into light intensity variation by FPI and deteriorate the lower hydrogen detection limit. For phase fluctuation of 0.13° around quadrature point, the slope change of the phase-to-intensity transfer function can be determined to be $1-\cos(0.13^\circ)=2.65\times10^{-6}$. For gas detection of hydrogen concentration of 100%, the relative measurement uncertainty due to this slope variation would be $\Delta C=2.65\times10^{-6}$ (2.65 ppm), which is a fundamental limiting factor of the detection limit of our hydrogen detection system.

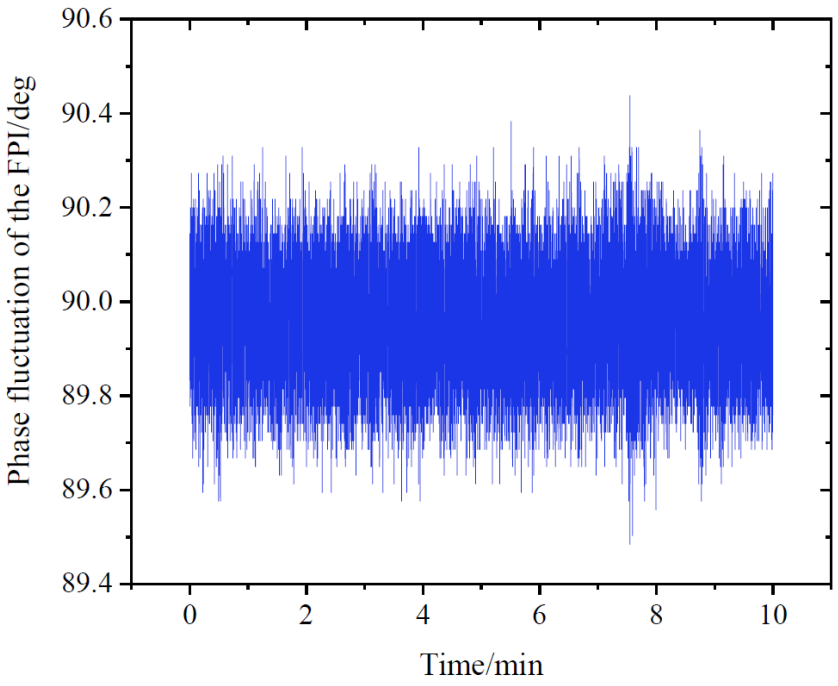

Fig. 5.8 Output phase fluctuation of the stabilized FPI at its quadrature point.

5.4 Hydrogen detection based on a hollow-core FPI

5.4.1 Experimental setup

Fig. 5.9 depicts the experimental setup for hydrogen detection based on SRDS using a 3.5 cm long hollow-core FPI. The FSR of the FPI is ~40 pm. The FPI is stabilized using a servo controller which actively stretches the PZT to minimize the environmental perturbation as described in the previous section. An ECDL is operated with a fixed wavelength of 1620.4 nm as the probe light and is locked to the quadrature point of the FPI. The pump laser used here is a DFB laser which is sinusoidally wavelength modulated around 1532.5 nm with a modulation frequency of 51 kHz. Simultaneously, the wavelength of the DFB laser is slowly scanned so that the frequency difference between the probe and pump light is tuned across the $S_0(0)$ hydrogen Raman transition. The reflection and transmission of the FPI is received by an auto-balanced detector (Nirvana, 2017). The 2*f* of the detected signal is demodulated by a lock-in amplifier (Stanford research systems, SR830).

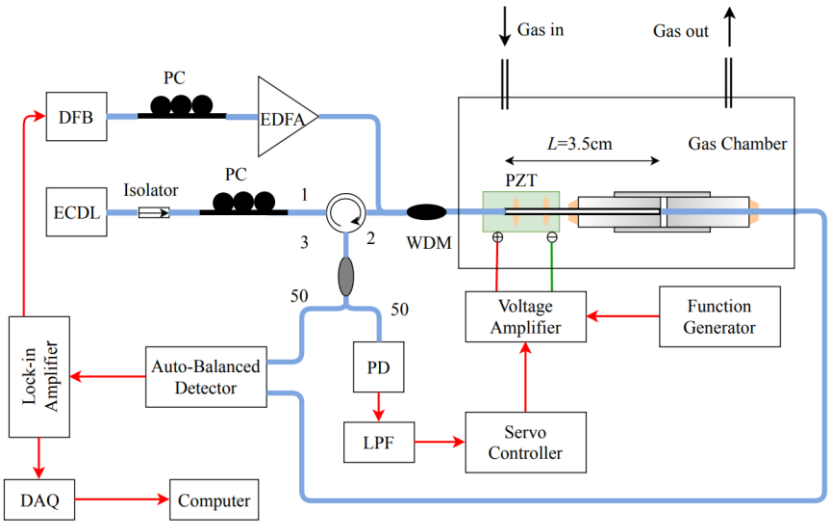

Fig. 5.9 Experimental setup for hydrogen detection with SRDS using a 3.5 cm long hollow-core FPI

5.4.2 Hydrogen detection results

The hydrogen detection experiment is conducted using pure hydrogen at atmospheric pressure and room temperature. The sinusoidal modulation amplitude of the lock-in amplifier output is 56 mV. The time constant of the lock-in amplifier is 1s with filter slope of 18 dB/Oct. The demodulated 2*f* signals of the measured SRD with pump power ranging from 25 to 125 mW delivered in HC-PCF are shown in Fig. 5.10(a).

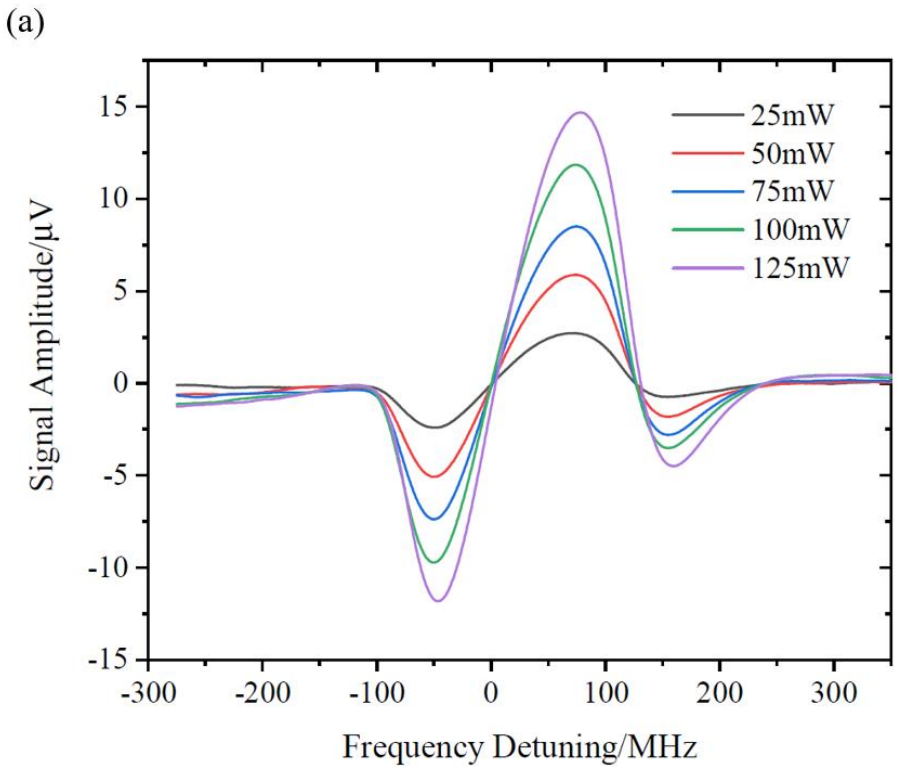

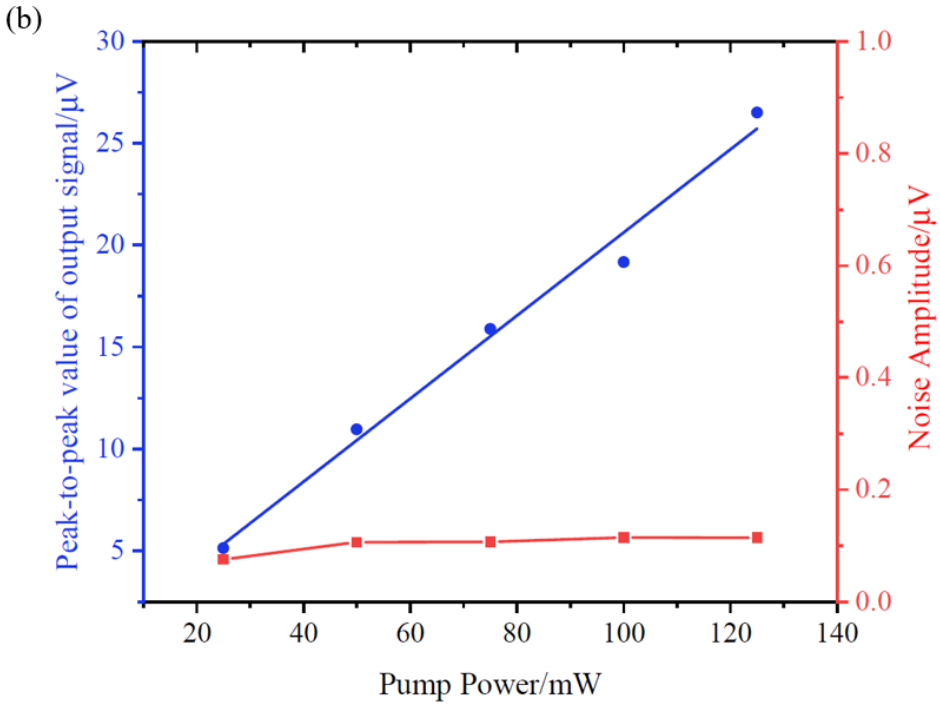

Fig. 5.10 (a) The measured 2*f* signal of the SRD when pump laser is slowly scanned across the $S_0(0)$ Raman transition with different pump power ranging from 25 to 125 mW delivered within the HC-PCF. (b) The peak-to-peak value of the demodulated 2*f* signal is linearly proportional to the pump power delivered within the HC-PCF and the standard deviation of the noise is as a function of the pump power.

To evaluate the performance of the hydrogen detection system, the detection noise is measured by tuning the pump wavelength away from the Raman resonance to 1532.893 nm. The standard deviation of noise for different pump power levels ranging from 25 to 125 mW is shown in Fig. 5.10(b) as the red squares. For a pump power of 125 mW launched in the HC-PCF, the peak-to-peak value of the 2*f* output signal for 100% hydrogen is 26.5 μV and the standard deviation of noise is 0.11 μV for 1s lock-in time constant, corresponding to the detection bandwidth of 0.094 Hz, which gives an SNR of 240. The detection limit in terms of NEC for an SNR of unity is then estimated to be 0.42%. The normalized detection limit of the Fabry Perot interferometer is 18.3 ppm/(m · W). The Fabry Perot interferometer has a similar performance to the

Mach-Zehnder interferometer. In Fig. 5.10(b), the peak-to-peak value of the 2*f* output signal increases approximately linearly with the pump power while the noise level remained relatively unchanged, indicating further improvement of detection limit is possible by simply increasing the pump power level.

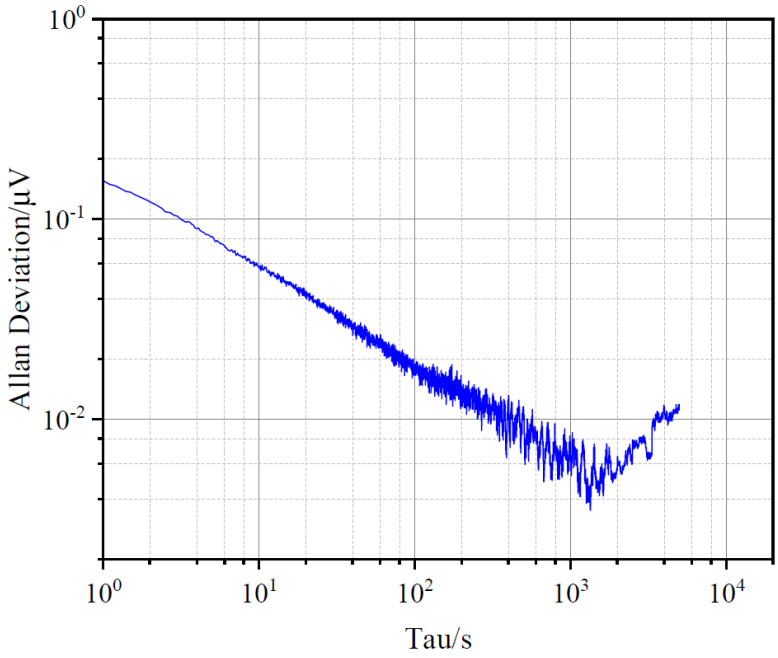

Fig. 5.11 Allan deviation plot calculated from a 3h-long period noise record with 125 mW pump light delivered within the HC-PCF. The optimal integration time is estimated to be 1300s.

Allan deviation analysis is also conducted here to investigate the stability of the proposed hydrogen sensor based on SRDS using a hollow-core FPI [5], [6]. The stability of the detection system allows using longer time constant to average out white noise component, which can further improve the lower detection limit of the hydrogen detection system. The 2*f* output signal for 100% hydrogen is recorded for 3 hours when the pump light is tuned away from the Raman transition resonance and fixed at 1532.893 nm with pump power of 125 mW in HC-PCF. The time constant of the lock-in amplifier is set to be 100ms. The Allan deviation plot calculated from the 3h-long noise record is

shown in Fig. 5.11. The optimal integration time t is determined to be ~1300s. The noise after being averaged with the optimal Tau is estimated to be 7×10^{-3} μV and the corresponding NEC for an SNR of unity is then estimated to be 264 ppm.

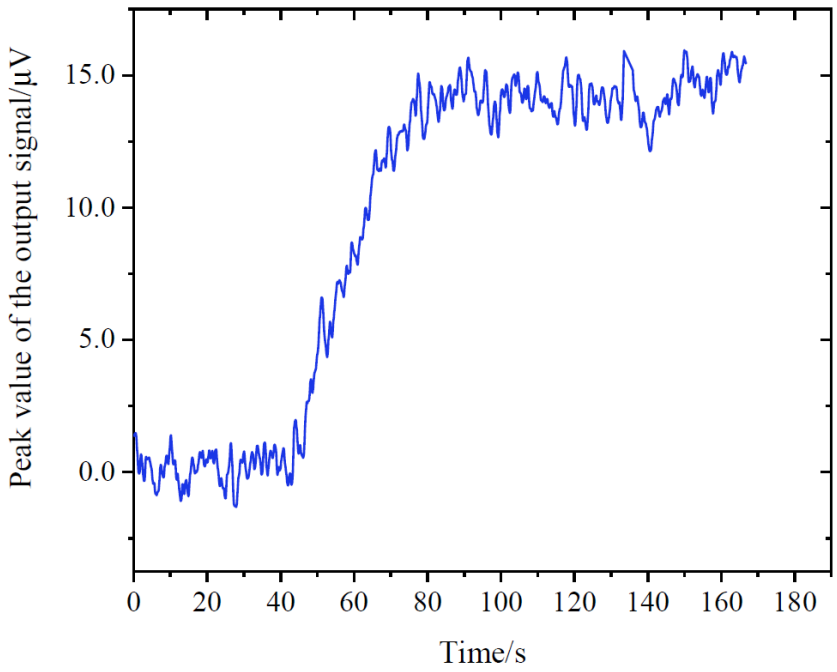

Fig. 5.12 The 2*f* output signal as a function of time during hydrogen filling process.

In this experiment, the gas chamber volume is nearly 1.25L (25 x 10 x 5 cm). The hydrogen filling process is monitored with the proposed hollow-core FPI. Since the relatively large volume of the gas chamber, it takes longer time (compared with the response time of the hydrogen sensor) for hydrogen concentration in the gas chamber to reach that of the source gas [7]. During the filling process, the pump is tuned to the wavelength where the 2f signal magnitude reaches its maximum. Fig. 5.12 shows the monitored 2*f* output signal change as 100% hydrogen is filled into the gas chamber with pump power of 125 mW delivered into the HC-PCF. The time constant of the lock-in amplifier is set to be 300 ms. The output signal starts increasing at ~40s and gradually becomes stable after 85s, giving a response time of 45s.

To evaluate the long-term performance of the proposed hydrogen sensor, the maximum value of the 2*f* output signal for 100% hydrogen is monitored for 6 hours with pump power of 125 mW in HC-PCF shown in Fig. 5.13. The time constant of the lock-in amplifier is set to be 1s. The amplitude of the 2*f* output signal fluctuation is about 0.12 μV, giving a relative signal variation of 0.83%.

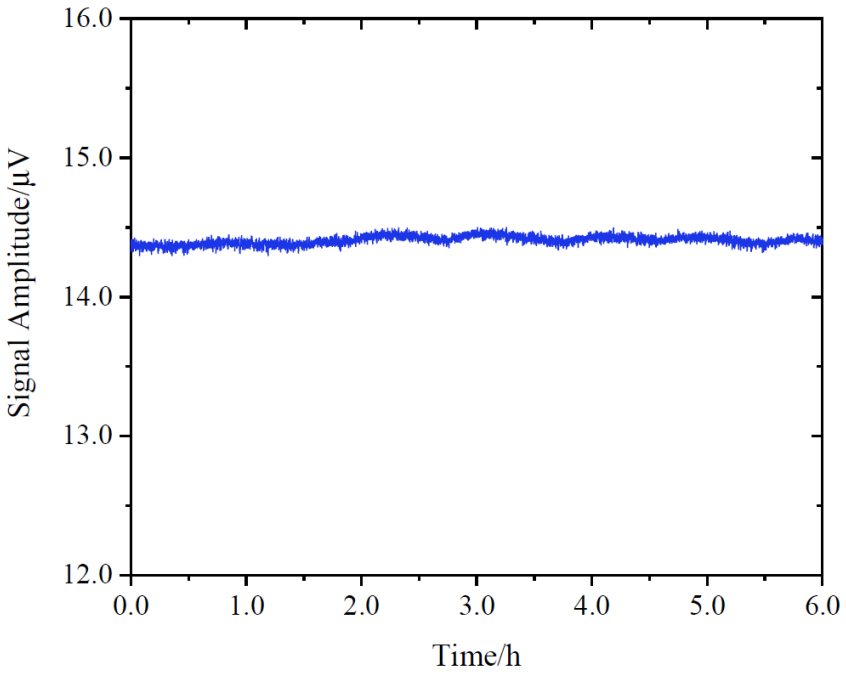

Fig. 5.13 The monitored 2*f* output signal for 100% hydrogen with pump power of 125 mW

5.4.3 Discussions

Compared with the hydrogen detection scheme using an all-fiber MZI introduced in Chapter 4, measurement of the Raman-induced phase change using a hollow-core FPI is not affected by the background signal. In Chapter 4, the pump light and probe light are co-propagating within a section of SMF before entering the HC-PCF. The $S_0(0)$ Raman

transition of hydrogen is ~354.4 cm^{-1} which is located within the Raman gain spectrum of the SMF shown in Fig. 5.14 [8]. Since only the sensing arm of the MZI experience the SRS process of the SMF, the detected phase change would contain that phase modulation induced by SRS in SMF. Though the Raman gain coefficient of the SMF is nearly 1×10^{-13} m/W, which is nearly an order smaller than the Raman gain coefficient of hydrogen, it provides a strong enough background signal which may interfere the signal measurement. Additionally, copropagating with the strong power pump light, the probe light would be additionally phase-modulated through cross-phase modulation (XPM) effect in SMF since XPM in hollow-core fibers is significantly weaker[9]. Contributes of the XPM effect to the detected background signal[10]:

$$\Delta\phi_{XPM} = 2\times 2\pi / \lambda_{probe} n_2 I_{pump} L_{SMF} \tag{5.6}$$

where n_2 is the nonlinear-index coefficient and L_{SMF} is the length of SMF that probe light and pump light are co-propagating in the sensing arm of the MZI. However, for the hollow-core FPI, it only detects the phase difference between the two reflected/transmitted light which travel through the same SMF and no background signal because the Raman gain and XPM in air can be neglected [11], [12].

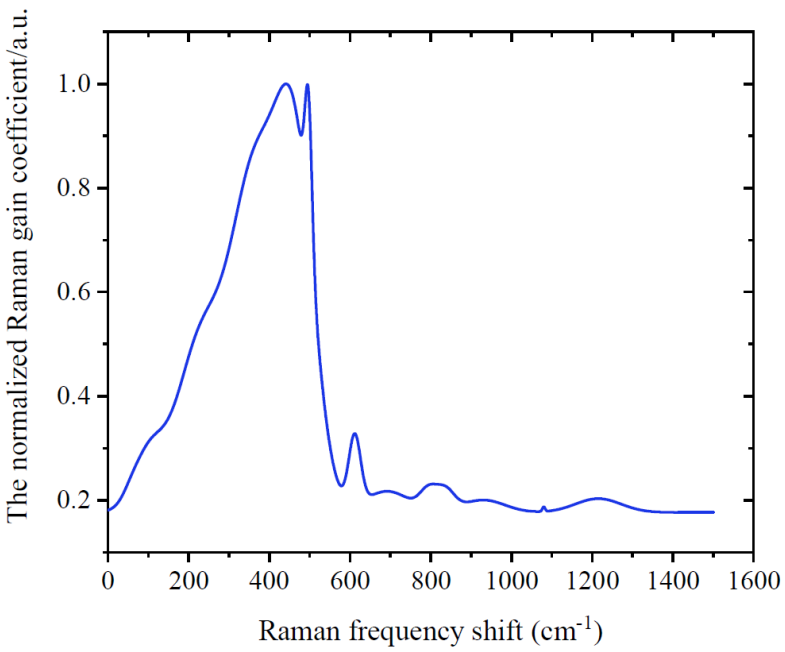

Fig. 5.14 The calculated normalized Raman gain spectrum

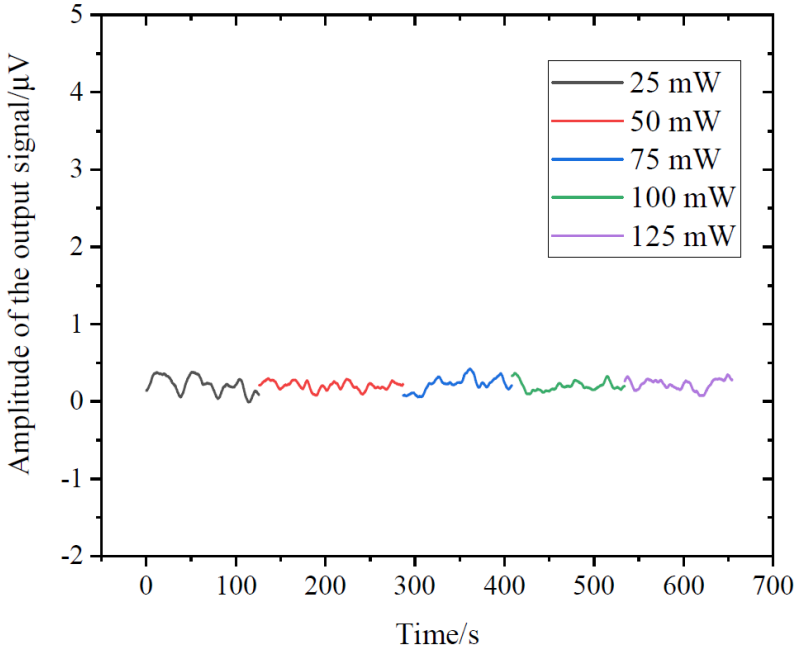

Fig. 5.15 The measured background signal of the hydrogen sensor using hollow-core FPI with pump light power ranging from 25-125 mW.

To evaluate the background signal of the hydrogen detection system, the wavelength of the pump light is tuned away from the Raman transition resonance. Fig. 5.15 depicts the 2*f* output signals when the pump light power is increased from 25 to 125 mW. The time constant of the lock-in amplifier is 1s. It is shown that the 2*f* output signals are remained stable and close to zero as the pump light power delivered within the HC-PCF increased, indicating that no significant background signal is measured using the hollow-core FPI.

5.5 Summary

In this chapter, a hydrogen sensor based on SRD using a hollow-core FPI is proposed. Compared with the detection scheme using all-fiber MZI, it has smaller size and faster response time. And due to the operation principle of the hollow-core FPI, the detected SRD of hydrogen is generally immunized from the background signals of the Raman and XPM effects in SMF. With a 3.5 cm-long how-core FPI, hydrogen detection with detection limit of 0.42% using 1s integration time constant is demonstrated in this chapter. Lower detection limit of 264 ppm may be realized by conducting the Allan deviation analysis and applying the optimal integration time constant of ~1300s. The demonstrated system shows a good long-term stability.

References

1 H. Bao, W. Jin, Y. Miao, and H. L. Ho, “Laser induced dispersion with stimulated Raman scattering in gas-filled optical fiber,” *J. Light. Technol.*, vol. 37, no. 9, pp. 1–1, 2019.

2 F. Yang, Y. Zhao, Y. Qi, Y. Z. Tan, H. L. Ho, and W. Jin, “Towards label-free distributed fiber hydrogen sensor with stimulated Raman spectroscopy,” *Opt. Express*, vol. 27, no. 9, p. 12869, 2019.

3 C. L. Zhao, L. Xiao, M. S. Demokan, W. Jin, and Y. Wang, “Fusion Splicing Photonic Crystal Fibers and Conventional Single-Mode Fibers: Microhole Collapse Effect,” *J. Light. Technol.*, vol. 25, no. 11, pp. 3563–3574, 2007.

4 Y. Tan, W. Jin, F. Yang, H. L. Ho, and H. Kong, “High finesse hollow-core fiber resonating cavity for high sensitivity gas sensing application,” *J. Light. Technol.*, vol. 10323, no. 1, pp. 1–4, 2017.

5 P. Werle, R. Mücke, and F. Slemr, “The limits of signal averaging in atmospheric trace-gas monitoring by tunable diode-laser absorption spectroscopy (TDLAS),” *Appl. Phys. B Photophysics Laser Chem.*, vol. 57, no. 2, pp. 131–139, 1993.

6 P. Werle, “Accuracy and precision of laser spectrometers for trace gas sensing in the presence of optical fringes and atmospheric turbulence,” *Appl. Phys. B Lasers Opt.*, vol. 102, no. 2, pp. 313–329, 2011.

7 Y. Cao, W. Jin, H. L. Ho, L. Qi, and Y. H. Yang, “Acetylene detection based on diode laser QEPAS: Combined wavelength and residual amplitude modulation,” *Appl. Phys. B Lasers Opt.*, vol. 109, no. 2, pp. 359–366, 2012.

8 D. Hollenbeck and C. D. Cantrell, “Multiple-vibrational-mode model for

fiber-optic Raman gain spectrum and response function," *J. Opt. Soc. Am. B*, vol. 19, no. 12, pp. 2886–2892, 2002.

9 R. W. Boyd, *Nonlinear optics*. Academic Press, 2008.

10 G. Agrawal, *Chapter7 Cross-Phase Modulation*. 2013.

11 M. Rokni and A. Flusberg, "Stimulated Rotational Raman Scattering in the Atmosphere," *IEEE J. Quantum Electron.*, vol. 22, no. 7, pp. 1102–1108, 1986.

12 P. S. J. Russell, P. Hölzer, W. Chang, A. Abdolvand, and J. C. Travers, "Hollow-core photonic crystal fibres for gas-based nonlinear optics," *Nat. Photonics*, vol. 8, no. 4, pp. 278–286, 2014.

Chapter 6: Tuning of group delay with stimulated Raman scattering induced dispersion in hydrogen-filled HC-PCF

6.1 Introduction

In previous chapters, stimulated Raman induced RI change has been measured and applied for sensitive hydrogen detection. Though the RI change is small, it results in steep RI change near the $S_0(0)$ Raman transitions of hydrogen molecules due to its narrow linewidth. Such induced dispersion can, in principle, be dynamically adjusted by changing the pump laser wavelength and power level as well as the gas pressure, composition and concentration. Such method provides possibilities of controlling dispersion in HC-PCF with high flexibility. In this chapter, I report the first demonstration of dynamical group delay control by exploiting SRS induced dispersion in a hydrogen-filled HC-PCF. By varying the pump power level, the signal pulse delay can be tuned continuously in a linear fashion. Tuning of optical pulse delay on the scale of nanosecond is realized.

6.2 Theory of SRS induced Group Delay

When a pump beam (ω_{pump}) and a signal beam (ω_{signal}) are copropagating within Raman-active medium, and their frequency difference matches the Raman frequency shift (ω_0), i.e., $\omega_{pump} - \omega_{signal} = \omega_0$, SRS induces Raman gain near the Stokes wavelength, which is associated with the imaginary part of the Raman susceptibility $\chi_R(\omega_{signal})$ of the gas

medium. SRS also induces a RI change related to the real part of $\chi_R(\omega_{signal})$, which may be expressed as [1]:

$$\Delta n(\omega_{signal}) = \frac{cg_0 I_{pump}}{2\omega_{signal}} \frac{\delta}{1+\delta^2} \tag{6.1}$$

where c is the speed of light, g_0 is the peak gain coefficient that is proportional to the gas concentration (C), I_{pump} is the pump light intensity, $\delta = 2\left[\omega_0 - \left(\omega_{pump} - \omega_{signal}\right)\right] / \Gamma_R$ is the linewidth-normalized frequency detuning parameter and $\Gamma_R / 2\pi$ is the Raman linewidth. Due to the narrow linewidth of Raman resonances of hydrogen, the rapid RI variation would lead to a considerable change of the group RI and hence appreciable change in the group velocity and pulse group delay. The relationship between the SRS-induced RI and group RI change near a Raman resonance is shown in Fig. 6.1.

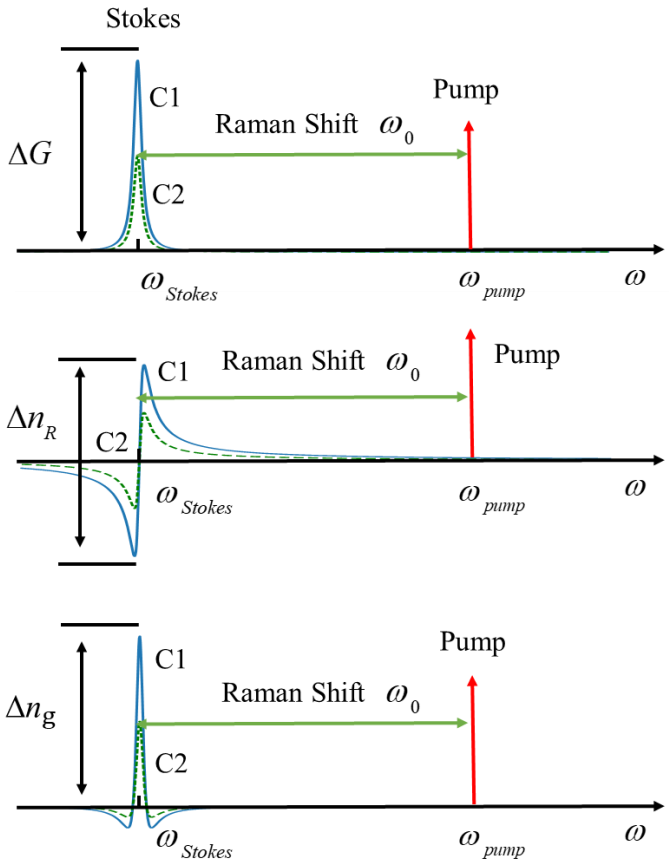

Fig. 6.1 The signal pulses (ω_{signal}) experience a Raman gain, Raman-induced RI change and group RI change near the Raman transition (ω_0).

The group delay experienced by a signal pulse near Stokes wavelength over length L is established as[2]:

$$\Delta t_g = \frac{L}{v_g} = \frac{G}{\Gamma_R}\frac{1-\delta^2}{\left(1+\delta^2\right)^2} \tag{6.2}$$

where $G = g_0 I_{pump} L$, v_g is the group velocity. As can be seen from Eq. (2), the group delay is proportional to the Raman gain at the Stokes wavelength ($\delta = 0$) over the Raman linewidth and can be dynamically tuned by varying pump power.

The Raman linewidth of hydrogen is pressure dependent, which gives us another degree of freedom to control the signal pulse delay. Two pressure-dependent effects, i.e., molecular collisions (Γ_C) and fiber-wall collisions (Γ_W), contribute to the Raman linewidth:

$$\Gamma_R = \Gamma_C + \Gamma_W \tag{6.3}$$

Molecular collisions contribute a Lorentz broadening line-shape, which, for the $S_0(0)$ transition of hydrogen, may be expressed as[3]:

$$\Gamma_C / 2\pi = 1.876 / P + 84P \tag{6.4}$$

However, in the small hollow core (e.g. the core radius of HC-1550-06 fiber is ~5 μm) of the HC-PCF, collisions between the inner wall of the hollow core and hydrogen molecules may contribute to the linewidth, which may be expressed as[4]:

$$\Gamma_W / 2\pi = \frac{5.784 D_0}{r^2 \rho(P)\left(1+6.8\frac{\bar{l}}{r}\right)} \tag{6.5}$$

where D_0 is the molecular self-diffusion coefficient at the room temperature, r is the core radius of HC-PCF, ρ is the gas density which is proportional to gas pressure and $\bar{l}$ is the mean free path of hydrogen molecules. The calculated linewidth of the $S_0(0)$

Raman resonance of hydrogen as a function of gas pressure in HC-1550-06 fiber is depicted in Fig. 6.2(a). The linewidth gradually decreases and then increases as the gas pressure increases from low pressure limit to the high pressure region. The narrowest linewidth of the $S_0(0)$ Raman resonance of hydrogen is estimated to be 95 MHz. The group delay with different hydrogen pressure when the Raman gain of the signal light is 3dB at Raman resonance is given in Fig. 6.2(b). Given 3dB Raman gain, the maximum group delay is 1.15 ns when the hydrogen pressure is nearly 0.57 bar within the HC-PCF.

(a)

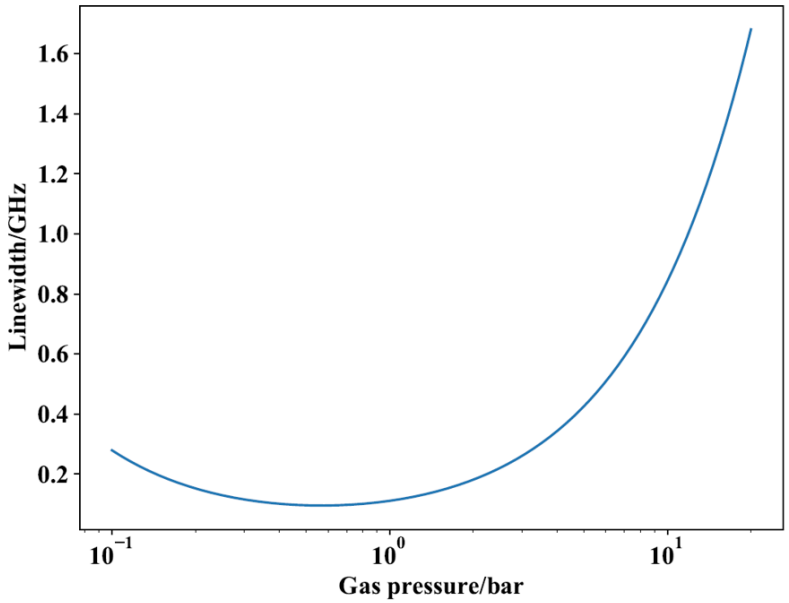

(b)

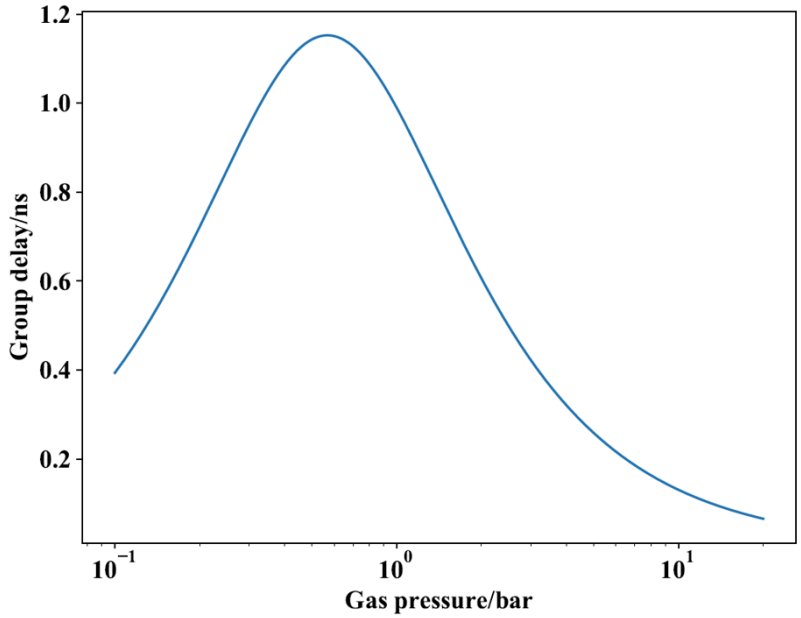

Fig. 6.2 (a) The linewidth of the $S_0(0)$ Raman transition as a function of hydrogen pressure within HC-PCF. The core radius of the HC-PCF is about 5.5 μ m. (b) The Raman-induced group delay as a function of gas pressure when the Raman gain of the signal light is 3 dB at Raman resonance.

6.3 Determination of the SRS-induced group RI change

To evaluate the magnitude of RI and group RI ($n_g = c / v_g$) change, we measured the laser-induced RI change around the $S_0(0)$ transition (=354.36 cm^{-1}) of hydrogen using an 80-m-long HC-PCF (NKT HC-1550-06) filled with pure hydrogen at the gas pressure of 4 bar. The experimental setup is shown in Fig. 6.3(a). The pump beam from a DFB laser with wavelength around 1532.1 nm is intensity-modulated sinusoidally at 50 kHz by an acoustic-optic modulator (AOM). A fiber MZI powered by a signal laser beam from an ECDL is used for the RI measurement. The wavelength of the signal beam is fixed at the Stokes wavelength (1620.055 nm) and the SRS-induced RI change is determined by measuring the accumulated phase change of the signal light. The

accumulated phase change is related to the Raman induced RI change by:

$$\Delta\phi(\delta) = \frac{2\pi}{\lambda_{signal}} \Delta n(\omega_{signal}) L = \frac{1}{2}\left(\frac{\delta}{1+\delta^2}\right) g_0 I_{pump} L \tag{6.6}$$

The SRS-induced group RI change is given by[5]:

$$\Delta n_g(\delta) = \frac{c g_0 I_{pump}}{\Gamma_R} \frac{1-\delta^2}{\left(1+\delta^2\right)^2} \tag{6.7}$$

The first harmonic (1*f*) of the MZI output, which is linearly proportional to the induced phase change, is lock-in detected. The detected phase change is calibrated by comparing it with a reference phase modulation produced by a PZT phase modulator when the pump is off. The calibration phase modulator is also driven sinusoidally at 50 kHz, with the driven voltage increased slowly until a phase modulation amplitude of π rad is achieved. The output of the MZI is shown in Fig. 6.3(b). The amplitude of the phase modulation applied to the PZT is then reduced by a factor of 100π, i.e., the amplitude of the phase modulation is 0.01 rad. For a fiber MZI which is stabilized at its quadrature point, the output signal is linearly proportional to the phase modulation $\Delta\phi$ since $\sin(\Delta\phi) \approx \Delta\phi$.

The magnitude of the lock-in detected phase change due to SRS-induced dispersion is compared with that generated from the calibration phase modulator by use of an ESA. The details about the calibration procedure can be found in Ref. [6]. The SRS-induced RI can then be recovered by using equation 6.6. The recovered RI change around the $S_0(0)$ Raman transition of hydrogen is shown in Fig. 6.3(c). A very sharp RI change is obtained near Raman resonance. The maximum RI change is $2.89*10^{-11}$ with ~25 mW pump power delivered into the HC-PCF, corresponding to a group RI change of $1.22*10^{-4}$ based on equation 6.7. The group RI change is nearly 7 orders of magnitude larger than

the RI change, which may be used to effectively reduce the group velocity of signal pulses around the Stokes wavelength.

(a)

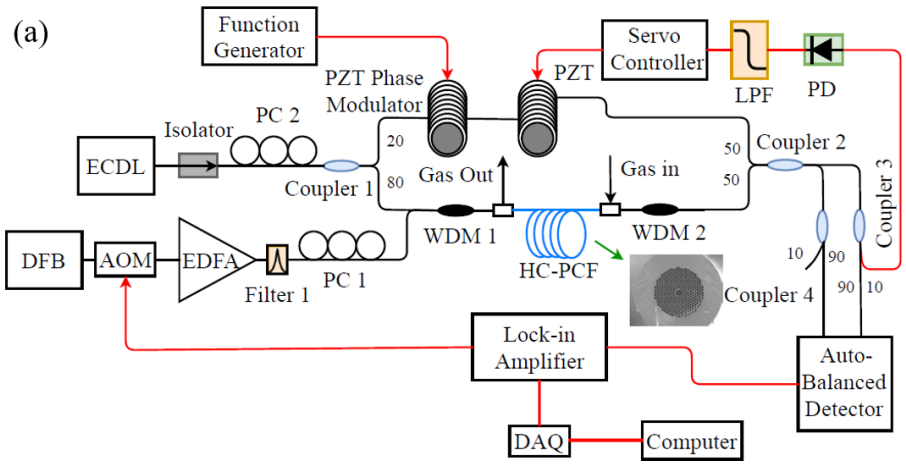

(b)

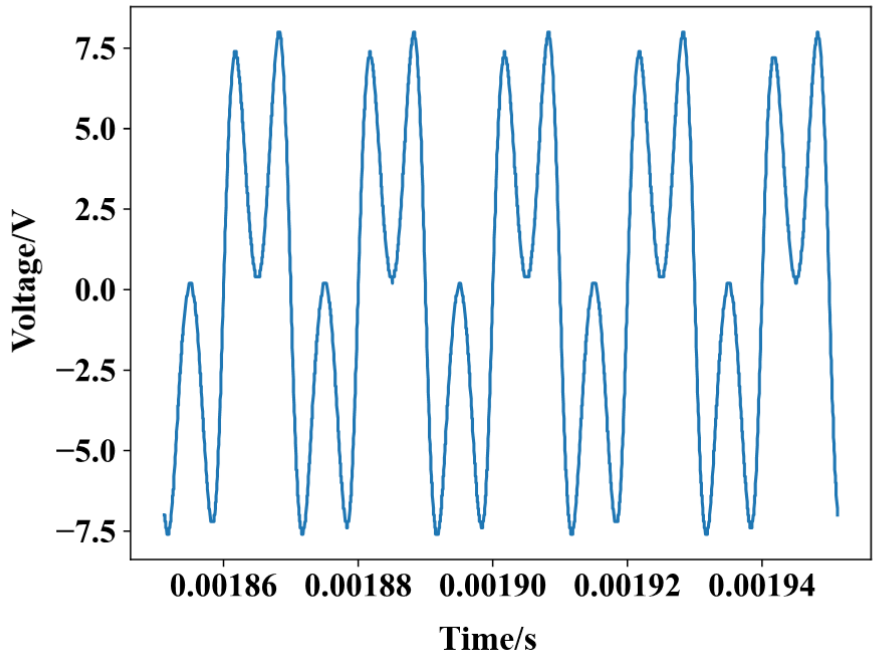

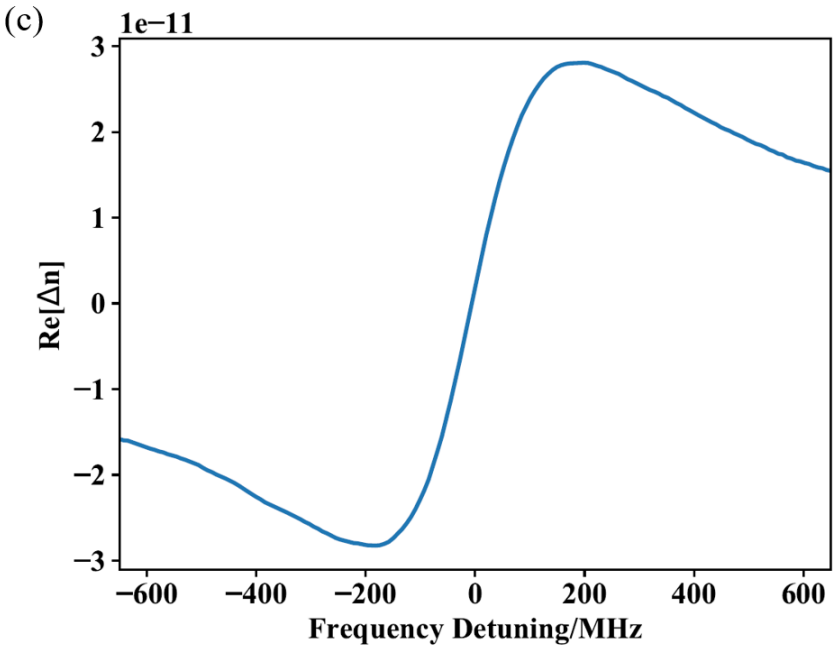

Fig. 6.3 (a) Experimental setup for measurement of SRS-induced dispersion. (b) The MZI output with the phase modulation amplitude is π rad and modulation frequency is 50 kHz when pump light is off. (c) SRS-induced RI change measured with an 80-m-long HC-PCF filled with 4-bar hydrogen and recovered using equation 6.6.

6.4 Measurement of the tunable pulse delay

6.4.1 Experimental setup

To demonstrate the tunable group delay of optical pulses with the hydrogen-filled HC-PCF, a stimulated Raman system operating at the $S_0(0)$ Raman transition of hydrogen is set up and shown in Fig. 6.4. The 3-ns-duration Gaussian signal pulses are generated by modulating the CW output of an ECDL and its wavelength is fixed at Stokes wavelength of 1620.38 nm. The 150-ns-duration rectangular pump pulses are generated by modulating the CW output of a DFB laser fixed at ~1532.39 nm. The pump pulses are amplified by an EDFA and combined with signal pulses via a WDM. Pump pulses and signal pulses are co-propagating and overlapping temporally within the

hydrogen-filled HC-PCF by delayed synchronization. 4-bar pure hydrogen is pressurized into the 80-m-long HC-PCF. At the output from the HC-PCF, the pump pulses are filtered out by the second WDM and the delayed signal pulses are recorded by an oscilloscope.

6.4.2 Experiment results of tunable pulse delay

The peak power level of the pump pulses is actively tuned to induce delay of signal pulses. Fig. 6.5(a) shows the measured signal pulses with 0 and 10 dB Raman amplification. The pulse delay is ~1 ns, giving a relative delay factor of 0.33 when the Raman gain is 10 dB. The peak power of the pump pulses and signal pulses delivered to the HC-PCF are estimated to be ~1.66 W and ~0.1 mW, respectively. Dynamically controlling of signal pulse delay from 0 to 1 ns can be achieved by tuning the power level of the pump pulses. Fig. 6.5(b) shows that the signal pulse delay varies linearly with increasing Raman gain from 0 to 10 dB. The Raman gain is determined by measuring the amplification of Stokes light propagating through the HC-PCF. The output signal pulses have broader duration than the input pulses. The pulse broadening factor is measured to be B=1.32 with $B = t_{out} / t_{in}$, where t_{in} and t_{out} are the full width at half maximum (FWHM) of the input and output signal pulses at Stokes wavelength respectively. The maximum RI and group RI variation can be determined using equations 6.6 and 6.7. For the 10 dB Raman amplification, which gives maximum group delay of 1 ns, the group velocity reduction of signal pulses at Stokes wavelength is calculated to be $\Delta v_g = 1.12 \times 10^6$ m/s. The change of RI and group RI are estimated to be =~10^{-9} and = 3.75×10^{-3}, respectively. By changing hydrogen pressure in HC-PCF, the normalized pulse delays are varied correspondingly. In Fig. 6.5(b), the slopes of the fitting lines infer normalized pulse delays of 0.142 ns/dB, 0.1ns/dB and 0.068 ns/dB with hydrogen pressure of 2.5, 4 and 5.5 bar, respectively. Given the normalized pulse

delay and based on equation 6.2, the linewidth of the $S_0(0)$ Raman resonance of hydrogen can be estimated to be 259, 368 and 540 MHz for 2.5, 4 and 5 bar hydrogen within HC-PCF, respectively.

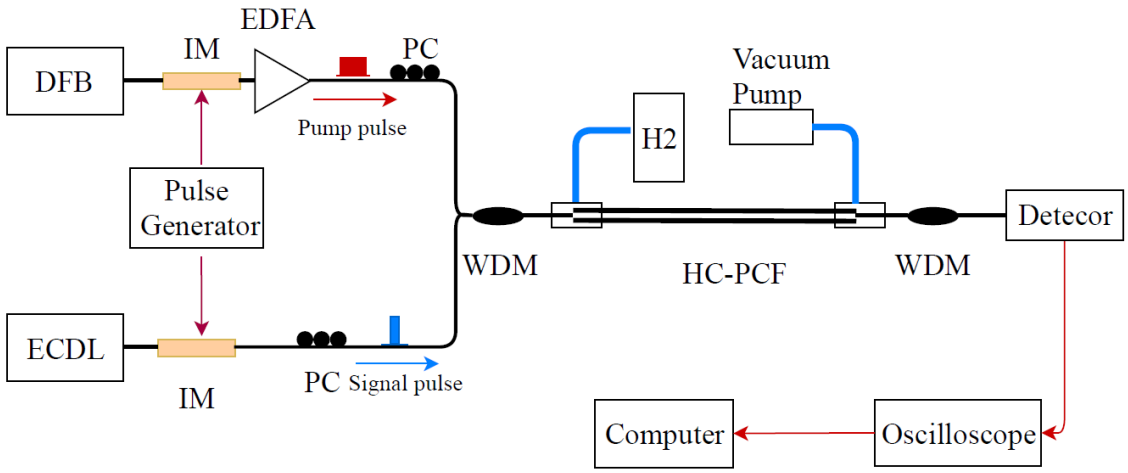

Fig. 6.4 Experimental setup of dynamically controlling laser-induced pulse delay with SRS in a hydrogen-filled HC-PCF. IM represents intensity modulator.

(a)

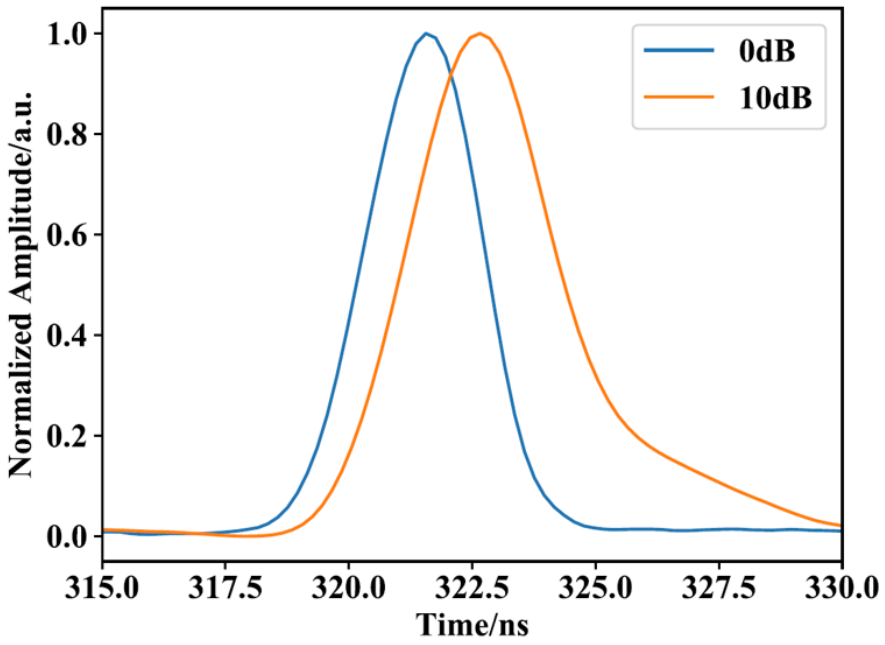
0dB
10dB
Normalized Amplitude/a.u.
1.0
0.8
0.6
0.4
0.2
0.0
315.0
317.5
320.0
322.5
325.0
327.5
330.0
Time/ns

(b)

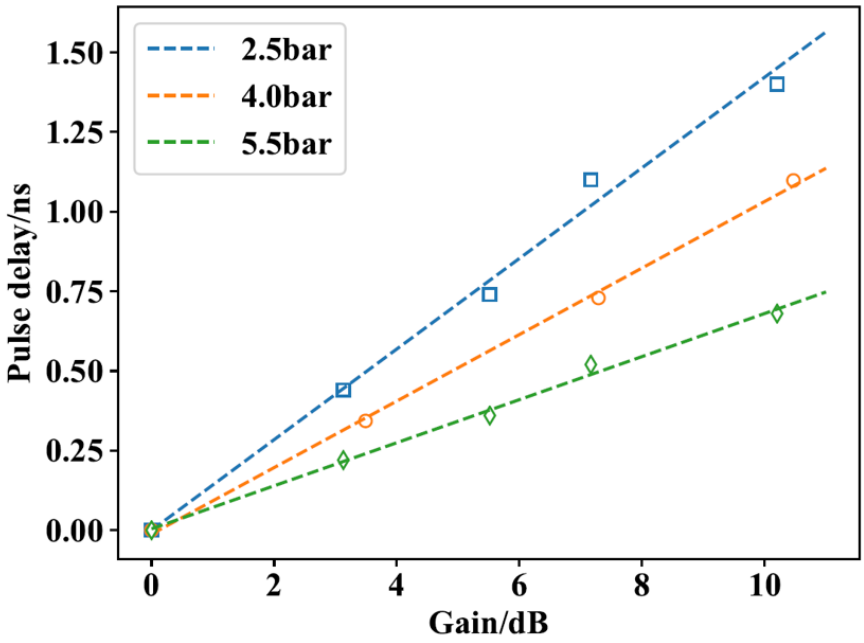
2.5bar
4.0bar
5.5bar
Pulse delay/ns
1.50
1.25
1.00
0.75
0.50
0.25
0.00
0
2
4
6
8
10
Gain/dB

Fig. 6.5 (a) Observation of 1 ns signal pulse delay with Raman gain of 10 dB using 4 bar hydrogen-filled, 80m-long HC-PCF. (b) Demonstration of dynamically controlling signal pulse delay by varying Raman gain with different hydrogen pressure.

To verify the theoretical relationship between the normalized pulse delay and hydrogen pressure within HC-PCF, the linewidth of $S_0(0)$ Raman resonance of hydrogen is measured using the experimental setup shown in Fig. 6.6.

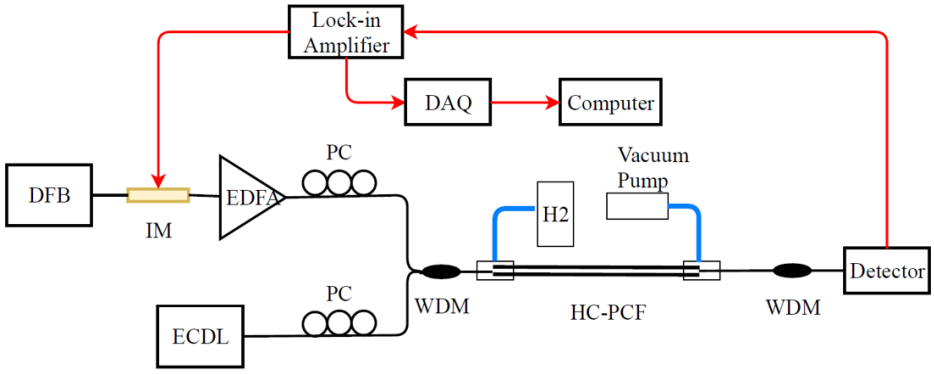

Fig. 6.6 Experiment setup for the measurement of Raman resonance linewidth with different hydrogen pressure within HC-PCF.

The signal beam is from a CW ECDL laser while the pump beam is from a CW DFB laser and intensity-modulated at 100 kHz. The pump power level delivered to the HC-PCF is ~15 mW. The frequency difference between the pump and signal beams is tuned to match the $S_0(0)$ Raman transition of hydrogen. The Raman gain profile is lock-in detected when the pump wavelength is tuned across the Raman transition. In Fig. 6.7(a), the measured Raman gain lines show various linewidth with 2.5, 4 and 5.5 bar hydrogen pressurized into the same 80-m-long HC-PCF. The corresponding Raman linewidth is estimated to be 230, 334 and 524 MHz. As it is shown in Fig. 6.7(b), the measured Raman linewidth agrees with the theory prediction. The corresponding group delays for optical pulses propagating in 80m-long HC-PCF filled with 2.5, 4 and 5.5 bar

hydrogen, are calculated and shown in Fig. 6.7(c) in blue line when Raman gain is kept as 10 dB. The measured pulse delay is also depicted in red squares, which agrees well with theory calculation.

(a)

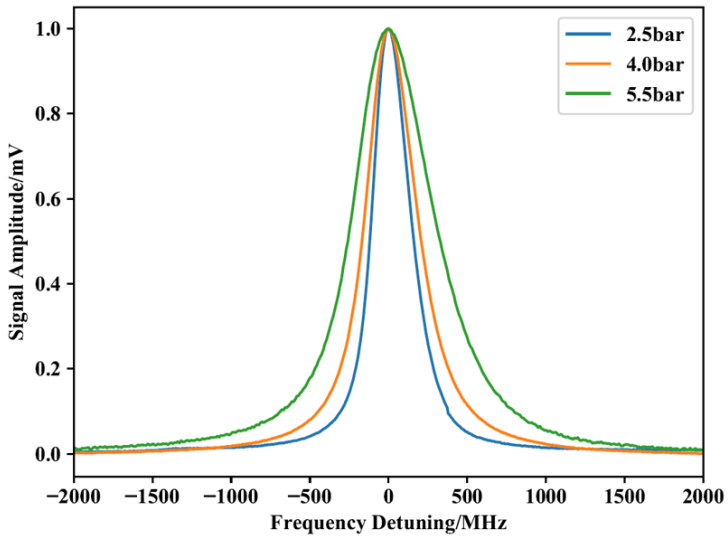

(b)

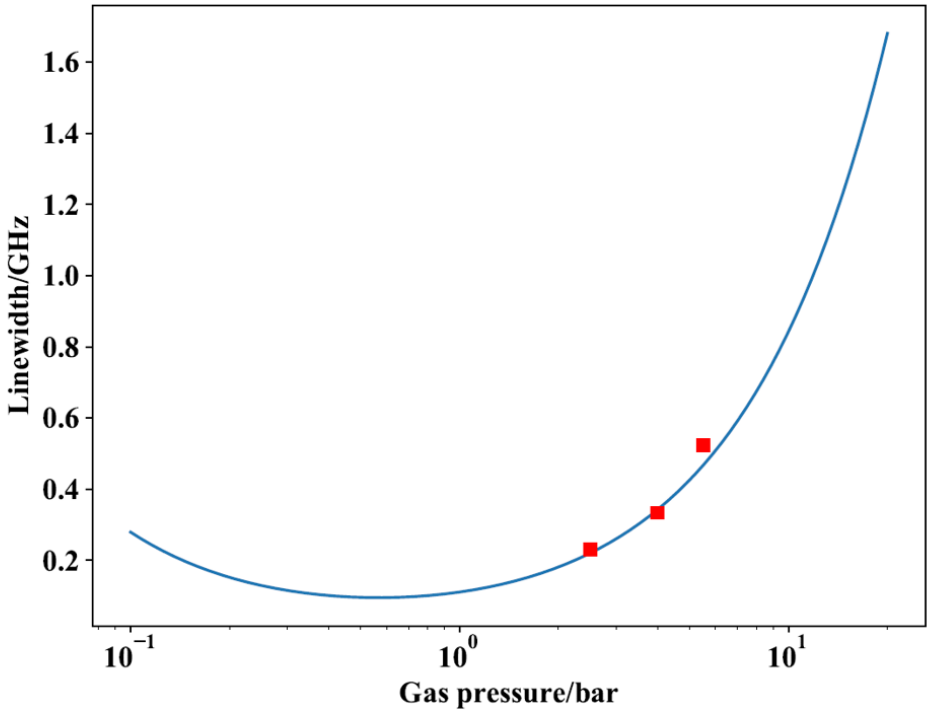

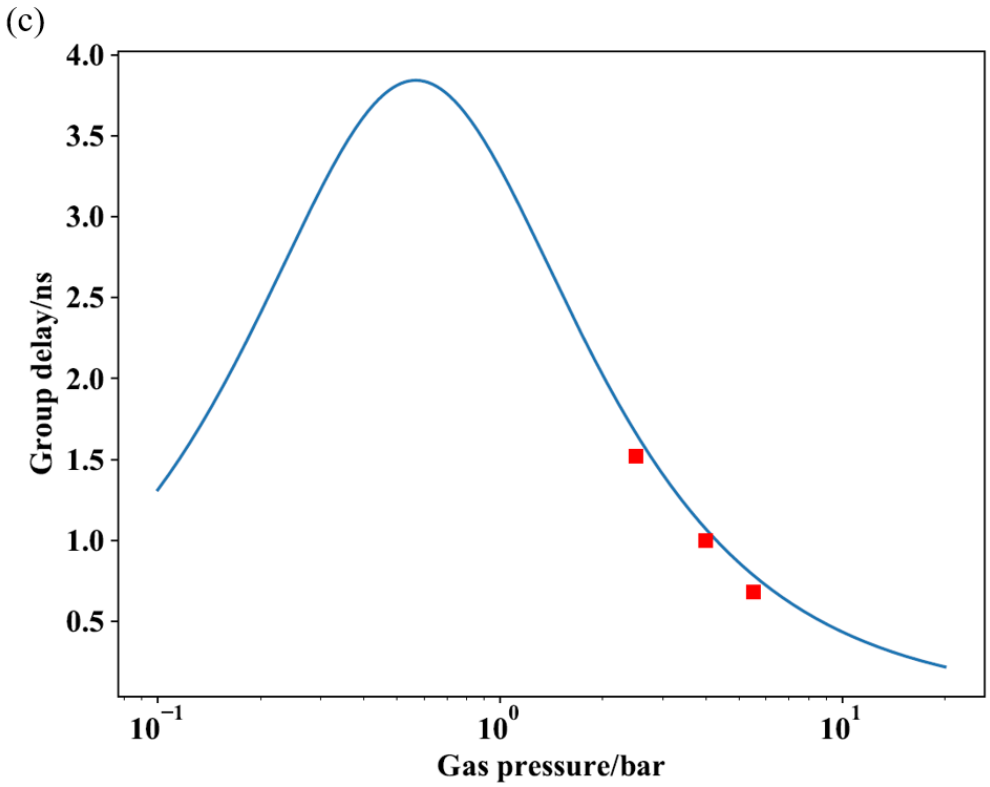

Fig. 6.7 (a) The measured Raman resonance of the 80-m-long hydrogen-filled HC-PCF. The linewidth of the Raman resonance is estimated to be 230, 334 and 524 MHz for 2.5, 4 and 5.5 bar hydrogen, respectively. (b) The comparison between the calculated (blue line) and the measured (red squares) linewidth of Raman resonance. (c) The comparison between the calculated (blue line) and the measured (red squares) group delays for optical pulses propagating in 80m-long HC-PCF filled with 2.5, 4 and 5.5 bar hydrogen when Raman gain is set as 10 dB.

Using SRS in gas-filled HC-PCF to control group delay has extra benefits. Gas-filled HC-PCF has a much higher damage threshold and can handle much higher pump power level than silica fibers[7]. Hence it potentially allows larger pulse delay by using a higher Raman gain. Relative delay factor surpasses 1 is possible with higher pump power level, which may be useful for a range of application in communication, signal processing and sensing systems.

6.5 Summary

In this chapter, the dynamic control of group delay using SRS-induced dispersion in hydrogen-filled optical fibers is demonstrated. Small but rapid variation of Raman-induced RI, which leads to significant group velocity change of signal pulses at Stokes wavelength, is measured. We have achieved pulse delay as much as 1.42 ns with Raman gain of 10 dB in an 80-m-long HC-PCF filled with 2.5-bar hydrogen. The signal pulse delay is actively tuned by adjusting the pump power level and gas pressure inside the hollow core. This technology is compatible with the existing optical fiber system and would have the potential to be applied for optical communication systems with capacity of wavelength complexing.

References

1 Guang S. He and Song H. Liu, *Physics of Nonlinear Optics*. WORLD SCIENTIFIC, 2000.

2 Y. Okawachi *et al.*, “Tunable all-optical delays via brillouin slow light in an optical fiber,” *Phys. Rev. Lett.*, vol. 94, no. 15, pp. 1–4, 2005.

3 B. W. K. Herring G C, Dyer M J, “Temperature and density dependence of the linewidths and line shifts of the rotational Raman lines in N2 and H2,” *Phys. Rev. A*, vol. 34, no. 3, p. 1944, 1986.

4 E. L. Cussler, *Diffusion : mass transfer in fluid systems*. Cambridge University Press, 2009.

5 G. Agrawal and G. Agrawal, “Chapter 8 – Stimulated Raman Scattering,” in *Nonlinear Fiber Optics*, 2013, pp. 295–352.

6 F. Yang, W. Jin, Y. Lin, C. Wang, H. Lut, and Y. Tan, “Hollow-core microstructured optical fiber gas sensors,” *J. Light. Technol.*, vol. 35, no. 16, pp. 3413–3424, 2017.

7 J. C. Travers, W. Chang, J. Nold, N. Y. Joly, and P. St. J. Russell, “Ultrafast nonlinear optics in gas-filled hollow-core photonic crystal fibers [Invited],” *J. Opt. Soc. Am. B*, vol. 28, no. 12, p. A11, 2011.

Chapter 7: Conclusions and future work

7.1 Conclusions

In this thesis, I propose and studied the stimulated Raman dispersion spectroscopy in HC-PCF and applied it for sensitive gas detection and tuning of optical pulses. The contributions of this thesis are listed as follows:

(1) Theory of the SRDS has been developed. We propose a highly sensitive interferometric detection method to measure the Raman-induced dispersion via wavelength modulation. The relationships between the measured harmonic signals and the Raman-induced dispersion is presented. The amplitude of the harmonic signals as functions of modulation depth is revealed and the optical modulation depth to acquire the largest harmonic signals have been calculated.

(2) Laser-induced dispersion via SRS in gas-filled optical fibers is measured by using an all-fiber MZI system. The system is extended for demonstration of hydrogen detection with high sensitivity. Detection limit of a normalized noise-equivalent concentration of 17.4 ppm/(m·W) at 3.5 bar and a dynamic range over 4 orders of magnitude using meters-long HC-PCF. The noise level of the system is evaluated, and the limiting factors of the system performance are discussed.

(3) To develop a practical hydrogen sensor with compact size the high performance, a hydrogen sensor based on SRDS with a hollow-core FPI is proposed. Such sensor is 3.5 centimeters long and is generally immunized from the background signals of the Raman

and XPM effects in SMF. Hydrogen detection limit of 264 ppm is achieved with an optimal integration time constant of ~1300s. The response time of the sensing head is estimated to be 45s. Such detection system also has good long-term stability, which can work stably for at least 6 hours.

(4) I extend the SRDS in hydrogen for dynamical controlling of the group velocity of optical pulses. The theory for the group velocity control is presented. The sharp dispersion change around the $S_0(0)$ Raman resonances hydrogen is measured. Pulse delay as much as 1.42 ns with Raman gain of 10 dB in an 80-m-long HC-PCF filled with 4-bar hydrogen has been realized. Tuning of optical pulse delay is demonstrated by actively adjusting the pump power level and gas pressure inside the hollow core.

7.2 Future work

So far, I have investigated the principles and some applications of the stimulated Raman dispersion phenomena, including sensitive gas detection and optical pulse delay. There are several future works should be addressed:

(1) Using hollow-core fibers with ultra-broad transmission window which may cover multiple Raman transition lines of gases, multi-gas detection system may be developed.

(2) To investigate the effect of the Raman-induced dispersion on a high finesse optical cavity. By tuning the Raman-induced dispersion, the resonant condition of the optical cavity would be changed correspondently.

(3) To further improve the Raman scattering efficiency, it is valid to develop or use waveguide with much smaller mode field diameter, such as nano-bore fiber and slot waveguide. Improvement of the Raman scattering efficiency may benefit sensitive gas sensors.

(4) Other applications may be implemented based on the stimulated Raman dispersion spectroscopy, e.g., high contrast imaging by direct measurement of the Raman dispersion of the sample medium, which offers better signal-to-noise-ratio due to better immunity.